Merging NLO QCD Corrections with Parton Shower Simulations

Zur Erlangung des akademischen Grades eines
DOKTORS DER NATURWISSENSCHAFTEN
von der Fakultät für Physik des
Karlsruher Instituts für Technologie (KIT) genehmigte

DISSERTATION

von

Master of Science Luca D'Errico
aus Neapel (Italien)

Mündliche Prüfung: 8. Juli 2011

Referent: *Prof. Dr. D. Zeppenfeld*
KIT, Institut für Theoretische Physik

Korreferent: *Prof. Dr. P. Richardson*
University of Durham, IPPP Institute

Institut für Theoretische Physik

Contents

Contents

"There's a great deal of excitement at CERN today and a tangible feeling that we're on the threshold of new discovery"

- Sergio Bertolucci, 22 April 2011 -

Abstract

Currently Monte Carlo event generators are playing a very important role for the simulation of signal and background processes at the Large Hadron Collider at CERN, in Geneva. For some observables it will be very important to consistently improve the accuracy of the predictions to higher orders in the perturbative expansion. In this direction, several approaches are possible. In the present thesis we consider the standard Herwig++ parton shower as well as a new, coherent dipole-type shower along with an automated way of matching. The work is focussed on the positive weight next-to-leading-order matching formalism (POWHEG), which combines parton shower simulation and next-to-leading-order calculation in a consistent way which only produces positive weight events. The POWHEG scheme is used in both approaches of parton showers algorithm and for three different processes.

The POWHEG method is applied to Deep Inelastic Scattering (DIS) and the related Higgs boson production via vector-boson fusion process in the Herwig++ Monte Carlo event generator. The simulation contains a full implementation of the truncated shower required to correctly model soft emissions in an angular-ordered parton shower. Furthermore, we present a method, based on the POWHEG matching scheme, to simulate photon production processes at next-to-leading-order. This technique is applied to the simulation of diphoton production in hadron-hadron collisions. The simulation includes both the photon fragmentation contribution and a full implementation of the truncated shower. The new, coherent dipole-type parton shower is tested in its final-initial and initial-final radiation by simulating radiation within the POWHEG formalism for the DIS process. We describe the NLO phase-space that is used for the calculation of the NLO momenta and phase-space integration of differential cross section. The present work is concluded with a comparison of the simulations of the two showers for the DIS process.

iv

Introduction

The Large Hadron Collider (LHC) at the European Organization for Nuclear Research (CERN) has recently started colliding protons at 7 TeV in the centre of mass frame and will continue to operate at half power until 2014, when proton beams are expected to circulate in the main ring at 14 TeV in the centre of mass frame, a new world record for the highest-energy man-made particle collisions.

The LHC is expected to illuminate a new landscape of physics in the coming years. We will learn whether electroweak symmetry breaking is realised as postulated by the Higgs mechanism, the last missing piece in the puzzle of the Standard Model. We will also address the question of whether Supersymmetry describes our universe or is only a mathematical tool. We may even obtain a deeper understanding of the space-time structure of Nature, by testing the idea of extra dimensions.

The price to pay for this precious knowledge is the tremendous complexity of the experiment at the LHC. On the one hand we have the technical issues of dealing with such a huge machine that is expected to measure micrometric distances. On the other hand we need a full understanding of the outcome of high-energy proton-proton collisions. The task is colossal and can only be addressed by a close collaboration between theory and experiment.

Theorists are expected to contribute by providing accurate predictions. To this end it is crucial that the strong interaction, which confines quarks in protons and governs processes involving quarks and gluons, which comprise the background, are well understood.

Quantum Chromodynamics (QCD) is the component of the Standard Model describing the interaction of coloured particles. It has been extensively tested at several collider experiments, such as the Large Electron Positron (LEP) collider, the Hadron-Electron Ring Accelerator (HERA) and Tevatron, and is widely accepted as the correct quantum field theory of strong interaction.

At high scales, the QCD predictions can be calculated by means of perturbative expansion in terms of quarks and gluons, commonly referred to as partons. However, since QCD becomes strongly coupled at small transferred momentum, partons that are produced in a scattering process fragment to observed hadrons. This physics is described by non-perturbative models, which are phenomenological models and

depend on parameters that are tuned to experimental data.

Monte Carlo event generators provide a description of collisions at particle accelarator experiments and a simulation of the physics involved. They supply a means, via a parton shower, of evolving from the high scale, where partons behave as free particles and a perturbative expansion can be applied, to a lower scale, where non-perturbative models are needed.

The perturbative physics consists of three parts: the hard subprocess, the shower and the decay. The hard subprocess is in general calculated at leading order. Each external leg then undergoes soft and collinear branching, the parton shower, which evolves from high to low scale. Finally each unstable particle decays according to the decay rate.

Next-to-leading order (NLO) perturbative QCD calculations provide the best description for inclusive observables. However, parton showers are needed when we want to calculate observables that are more exclusive and sensitive to higher multiplicity configurations. Therefore, the best description will be obtained by combining NLO QCD corrections with parton showers.

This is complicated because the NLO matrix element and parton showers both radiate in some regions of the phase-space. A prescription, known in the literature as an NLO *matching scheme*, is needed to remove the double counting and give NLO results for infrared safe observables in the strong coupling.

In the present work the POWHEG matching scheme of Refs. [1, 2] has been implemented for Higgs production via vector boson fusion, diphoton production and deep inelastic scattering (DIS) subprocesses in the Herwig++ parton shower of Ref. [3] and in the dipole-type parton shower of Ref. [4] for DIS. More precisely, the outline of this thesis is as follows.

We will start in Chapter 1 by introducing the basics of QCD theory and QCD single- and multiple-particle emissions, which are of interest for the understanding of the parton shower. We will describe parton showers and the POWHEG matching algorithm, giving particular attention to the Herwig++ and the dipole shower of Ref. [4].

Higgs production via vector boson fusion (VBF) is a very promising channel for Higgs searches at the LHC. In fact, since this process has a special kinematical structure that allows for good separation from the background, VBF is expected to play a fundamental rôle in the measurement of the Higgs coupling to gauge bosons and fermions in different decay channels, *i.e.* $H \to \tau^+\tau^-$ and $H \to W^+W^-$. The implementation of the POWHEG method for VBF in the Herwig++ parton shower will be discussed in Chapter 2.

One of the main backgrounds for the discovery channel of the Higgs boson decaying into a pair of photons will be discussed in Chapter 3, where we describe the implementation of the POWHEG formalism for diphoton production in hadron-hadron collisions for the Herwig++ parton shower.

The DIS process has made an important contribution to the understanding of the internal structure of hadrons and is very well-known in the literature. Its implementation in the Herwig++ parton shower, according to the POWHEG matching scheme, goes along the same lines as for Higgs production via vector boson fusion, as will be discussed in Chapter 4.

On the other hand, the implementation of the DIS in the dipoles shower follows a different approach, as will be described in Chapter 5: I designed and implemented the NLO phase-space and the program provides an automated method of matching. This process is an important test for the initial-final and final-initial radiation of the dipole shower, as will be extensively discussed.

In Chapter 6 we provide a summary of the approaches and compare distributions for the two showers, in the DIS case. The thesis ends with Chapter 7, which is dedicated to a summary and conclusions of the whole work, and a well documented bibliography.

Chapter 1

Parton Showers and QCD corrections

The Large Hadron Collider (LHC) has just begun working at CERN. Its primary goals are the detection of the Higgs boson, which would confirm the validity of the Standard Model and our understanding of the origin of mass, and particles predicted by theories of physics beyond the Standard Model, such as supersymmetry. The understanding of Quantum Chromodynamics (QCD), which underlies proton-proton scattering, has a crucial role in the analysis of discovery signals and backgrounds.

QCD is universally accepted as the correct quantum field theory of strong interactions and its predictions have been tested at different collider experiments, such as the Large Electron Positron (LEP) Collider and the Tevatron. Next-to-leading order (NLO) QCD corrections provide the best description for sufficiently inclusive observables. However, this is not enough when we want to calculate observables that are more sensitive to high multiplicity configurations: a parton shower algorithm, which is based on Monte Carlo simulation, would provide a better description in this case. Therefore the best picture will be obtained when we combine NLO corrections and a parton shower.

In this Chapter we review the way these two components can be pieced together. An overwiev of QCD is presented following Refs. [5,6]. We start by highlighting the main features of QCD and perturbative expansion within this theory (Sect. 1.1). More attention will be focussed on singularities and the parton branching formalism (Sect. 1.2). Collinear emissions will be studied in the simple case of two particles, before generalising to multi-parton branching and showing that the DGLAP equation resums the leading logarithmic divergences (Sect. 1.3). Soft emissions will be treated in Sect. 1.4. We will present an overview of Monte Carlo event generators in Sect. 1.5, emphasising the features of interest for the understanding of the rest of the thesis. We will reserve Sect. 1.6 for a discussion of parton shower simulation, focussing on the Herwig++ shower of Ref. [3] and the dipole shower of Ref. [4], which have been used in the present work. In Sect. 1.7 we will discuss the way the worlds of QCD corrections and parton showers can be combined, focussing on the POWHEG matching scheme, which is the algorithm used in the present work. In Sect. 1.8 we will conclude the Chapter by recapping the main topics discussed.

Flavour	Charge	Mass
u	$+\frac{2}{3}e$	~ 4 MeV
d	$-\frac{1}{3}e$	~ 7 MeV
c	$+\frac{2}{3}e$	~ 1.5 GeV
s	$-\frac{1}{3}e$	~ 135 MeV
t	$+\frac{2}{3}e$	~ 175 GeV
b	$-\frac{2}{3}e$	~ 5 GeV

Table 1.1: Flavours, electric charges and masses of quarks. Here e defines the charge of the electron, which is $1.602 \cdot 10^{-19}$C.

1.1 Quantum Chromodynamics

QCD is the component of the Standard Model describing the interactions of particles with colour charge, *partons*, and is constructed as a non-abelian gauge theory, $SU(N_c)$ [7]. Colour charge has three values, *i.e.* $N_c = 3$: red, green and blue. The fermions of the theory are called *quarks* and they are in a triplet of $SU(N_c)$. There are six types of quarks, known as flavours, and each of them also has QED charge, which is a fraction of the electron charge, as shown in Tab. 1.1. The antiparticles are called *antiquarks*. They have opposite electric charge and can take one of the three anticolours: antired, antigreen or antiblue. The gauge boson of the theory is called the *gluon* and is in a colour octet of $SU(N_c)$ and has zero mass. Quarks and gluons are not observed as free particles but rather clump together to form a singlet of $SU(N_c)$, *hadrons*; this is due to *confinement*, which is an intrinsic property of the theory, as we will see later in this section.

In the present section we aim to briefly introduce QCD, highlighting the features that will be useful for the understanding of the rest of this work. In Sect. 1.1.1 we will describe the Lagrangian of the theory, Sect. 1.1.2 summarises the notion of perturbative expansion in QCD and in Sect. 1.1.3 we will illustrate the running of the strong coupling.

1.1.1 QCD Lagrangian

QCD is constructed as a $SU(N_c)$ gauge theory with Lagrangian density

$$\mathcal{L}_{\text{QCD}} = \sum_{f=1}^{n_f} \bar{\psi}_i^f [i \, \slashed{D}_{ij} - m_f \delta_{ij}] \psi_j^f - \frac{1}{4} F_{\mu\nu,a} F_a^{\mu\nu} + \mathcal{L}_{\text{gauge}} + \mathcal{L}_{\text{ghost}}$$
$$\equiv \mathcal{L}_0 + \mathcal{L}_{\text{int}} + \mathcal{L}_{\text{gauge}} + \mathcal{L}_{\text{ghost}}, \tag{1.1}$$

where

$$\slashed{D}_{ij} \equiv \gamma^\mu D_{\mu,ij} = \gamma^\mu [\partial_\mu \delta_{ij} + i g_s A_{\mu,a} (T_a)_{ij}], \tag{1.2}$$
$$F_{\mu\nu,a} = \partial_\mu A_{\nu,a} - \partial_\nu A_{\mu,a} - g_s C_{abc} A_{\mu,b} A_{\nu,c}. \tag{1.3}$$

Here and throughout this work, greek letters indicate Lorentz indices and latin letters colour indices; in particular, abc go from 1 to $N_c^2 - 1$, whereas i, j range from 1 to N_c. The first two terms in Eqn. 1.1 are invariant under a local $SU(N_c)$ gauge

transformation. Within the Lagrangian, quarks are described by spinor fields, $\psi^f(x)$, where $f = 1, ..., n_f$ denotes the flavour of the quarks, and the gluon is described by the vector field $A_\mu(z)$. Moreover, C_{abc} are the structure constants of $SU(N_c)$, which define its *Lie algebra* and g_s is the coupling constant. The Lagrangian density of non-interacting quark fields is $\mathcal{L}_0 = \sum_{f=1}^{n_f} \bar{\psi}_i^f[i\,\not{\partial}_{ij} - m_f\delta_{ij}]\psi_j^f$ and $\mathcal{L}_{\text{int}}$ defines the interaction. The term $\mathcal{L}_{\text{gauge}}$ is needed to define the gluon fields propagator[1]. According to a prescription introduced by Faddeev and Popov [8], this is done by introducing the gauge fixing term [5]

$$\mathcal{L}_{\text{gauge}} = -\frac{1}{2\lambda}(\partial^\mu A_{\mu,a})^2. \tag{1.4}$$

Typically the gauge parameter, λ, is chosen to be $\lambda = 1$ and the gauge is called the *Feynman gauge*, where the gluon propagator has the simplest form.

Moreover, in non-abelian gauge theories, an extra ghost term must also be included in order to cancel the propagation of unphysical gluon field polarization [9]. This is done by the ghost contribution

$$\mathcal{L}_{\text{ghost}} = \partial_\mu \phi_a^\dagger \{D_{ab}^\mu \phi_b\}, \tag{1.5}$$

where ϕ_b is a scalar ghost field of Grassman variables. The ghost fields are unphysical so they do not appear as external particles.

1.1.2 Perturbative QCD

The differential cross section for the scattering of particle a, with momentum p_a, and particle b with momentum p_b, into particles of momenta $p_1...p_n$ is given by

$$d\sigma_{ab} = \frac{\bar{\sum}|\mathcal{M}(p_a p_b \rightarrow p_1...p_n)|^2}{F}d\Phi_n, \tag{1.6}$$

where $\bar{\sum}$ denotes the sum over all final-state quantum numbers and the average over initial-state quantum numbers of the process, $\mathcal{M}$ is the Feynman amplitude, F the incoming particle flux, given by $F = 4\sqrt{(p_a \cdot p_b)^2 - p_a^2 p_b^2}$ and the Lorentz invariant phase-space element (LIPS) for n outgoing particles is

$$d\Phi_n(p_a p_b \rightarrow p_1...p_n) = (2\pi)^4 \delta^4 \left(p_a + p_b - \sum_{k=1}^n p_k \right) \prod_{k=1}^n \frac{d^3 p_k}{(2\pi)^3 2E_k}. \tag{1.7}$$

The calculation of the Feynman amplitude, or S-Matrix elements, is performed within perturbation theory, where the interaction terms of the Lagrangian are considered as perturbations to the free Lagrangian. Matrix elements are constructed as a series in the couplings of the interaction terms, more specifically as a series in $\alpha_s = \frac{g_s^2}{4\pi}$. If the couplings are small, the series can be truncated and the result is an approximation at finite order.

---

[1]In order to define the propagator of the gluon fields, the operator associated with terms bilinear in the gluon fields needs to be inverted and to do that it is necessary to introduce gauge-fixing terms in the Lagrangian.

1.1.3 The running coupling constant

In Quantum Field Theories there are divergences coming from loop diagrams in which virtual particles propagate with unconstrained momentum: *virtual divergences*. These singularities are controlled by *renormalization*, which consists of rewriting the physical parameters in terms of *bare* parameters, which appear in the Lagrangian, such that the observable quantities are finite. Nevertheless it introduces a *renormalization scale* (μ) and *scheme* dependence into the physical parameters. The constraint that phyisical quantities do not depend on the unphysical scale can be expressed in terms of a differential equation, known as the *renormalization group equation*.

Considering the strong coupling, the most important parameter of QCD, this equation can be expressed as

$$Q^2 \frac{\partial \alpha_s}{\partial Q^2} = \beta(\alpha_s), \tag{1.8}$$

and for this reason we refer to the coupling as a *running coupling*. In the previous equation $\beta(\alpha_s)$ can be computed as a power series expansion in α_s [10, 11],

$$\beta(\alpha_s(Q^2)) = -b_0 \alpha_s^2(Q^2)(1 + b_1 \alpha_s(Q^2) + ...), \tag{1.9}$$

with $b_0 = \frac{33-2n_f}{12\pi}$ and $b_1 = \frac{153-19n_f}{2\pi(33-2n_f)}$. From the previous equation emerges the fact that for $n_f \leq 16$ the beta function has a negative sign, leading to a vanishing coupling constant in the large energy regime: this is a well known feature of QCD called *asymptotic freedom*. As opposed to QED, where the coupling increases with increasing energy, the beta function of QCD guarantees the validity of the perturbative expansion at high energies. This behaviour is shown by the solution of Eqn. 1.8 at 1-loop level:

$$\alpha_s(Q^2) = \frac{\alpha_s(\mu^2)}{1 + \alpha_s(\mu^2)b_1 \ln \frac{Q^2}{\mu^2}}. \tag{1.10}$$

Conversely, Eqn. 1.10 shows that the coupling diverges for small Q^2: this is another feature of QCD, known as *confinement*, and is responsible for the fact that partons are bound in hadrons and are not detected as free particles[2].

The absolute value of the coupling constant is not predictable and has to be obtained from experiment. Usually $\alpha_s(M_Z^2)$ is chosen as a reference point to ensure that the perturbative analysis is valid. Moreover, as an alternative to Eqn. 1.10, α_s can be expressed at leading-order in terms of the parameter Λ_{QCD} as [5]

$$\alpha_s(Q^2) = \frac{1}{b_1 \ln \frac{Q^2}{\Lambda_{QCD}^2}}. \tag{1.11}$$

Λ_{QCD} is the scale at which the coupling would diverge; qualitatively, it is the scale at which $\alpha_s(Q^2)$ becomes strong and the perturbative regime is not valid. It is not uniquely defined and depends on the renormalization scale, the number of active flavours and the order to which the beta function is computed: at 4-loops, in the $\overline{MS}$ scheme $\Lambda_{QCD}^{\overline{MS}} = 220$ MeV.

---

[2]A full description of the formation of hadrons is outside the domain of perturbation theory and relies on non-perturbative models of QCD that are not fully developed.
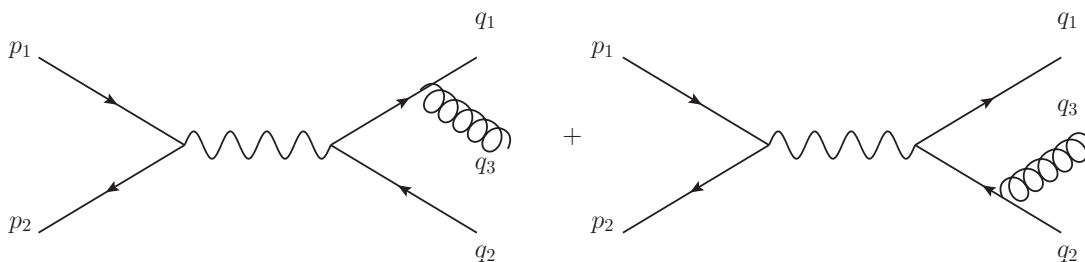
Figure 1.1: Feynman diagrams contributing to the radiative corrections of the process $e^+e^- \to$ hadrons.

1.2 The parton branching formalism

The parton shower is based on the parton branching formalism, which describes soft and collinear emissions in terms of enhanced contributions. The corrections have a universal factorized form and are logarithmically divergent. In Sect. 1.2.1 we will show the origin of these divergences for the process $e^+e^- \to$ hadrons and provide an argument to regulate them. Then in Sect. 1.2.2 we illustrate how singularities are factorized in terms Altarelli-Parisi splitting functions.

1.2.1 $\mathcal{O}(\alpha_s)$ radiative correction

The leading order cross section for the process $e^+e^- \to$ hadrons is given by

$$\sigma_B = N_c Q_q^2 \frac{4\pi\alpha^2}{3Q^2}, \tag{1.12}$$

where $Q_q e$ is the electric charge carried by the quark q, $\alpha = \frac{e^2}{4\pi}$ is the *fine structure constant* and Q is the momentum of the intermediate boson. The $\mathcal{O}(\alpha_s)$ real emission consists of two Feynman diagrams as shown in Fig. 1.1. The analytical contribution is given by

$$\sigma_R = \sigma_B C_F \frac{\alpha_s}{2\pi} \int \mathrm{d}x_1 \mathrm{d}x_2 \frac{x_1^2 + x_2^2}{(1-x_1)(1-x_2)}, \tag{1.13}$$

where $C_F = \frac{N_c^2-1}{2N_c}$,

$$x_i = \frac{2q_i \cdot Q}{Q^2} \tag{1.14}$$

are called *Dalitz variables* and define the momentum fraction, with integration region $x_i \in [0,1]$ and $x_1 + x_2 > 1$, cf. Fig. 1.2.

Eqn. 1.13 shows that the real emission contribution to the cross section diverges in the limits $x_1 \to 1$ and/or $x_2 \to 1$. This picture is the basis of the parton shower formalism and is better seen by expressing the momentum fraction in Eqn. 1.14 in terms of the opening angles θ_{ij} between the partons,

$$1 - x_1 = x_2 x_3 (1 - \cos\theta_{23}),$$
$$1 - x_2 = x_1 x_3 (1 - \cos\theta_{13}). \tag{1.15}$$
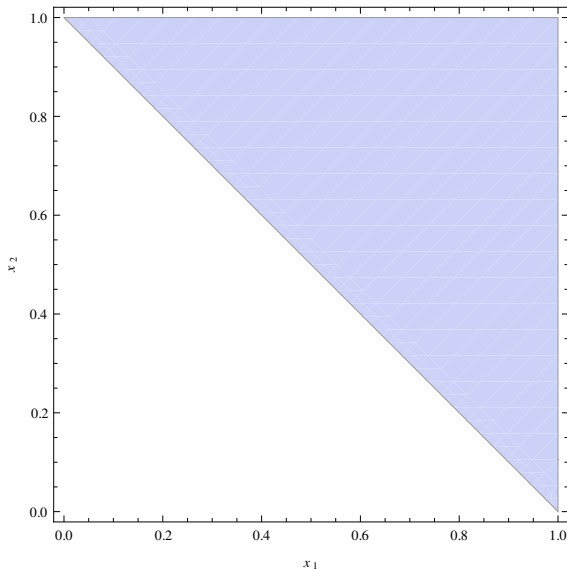
Figure 1.2: The shaded region shows the phase-space available in Dalitz variables, for the process $e^+e^- \to$ hadrons.

Therefore the singular region of the differential cross section corresponds to the limits where the gluon is collinear to the quark ($\theta_{13} \to 0$), or to the anti-quark ($\theta_{23} \to 0$), or it is soft ($x_3 \to 0$).

Eqn. 1.13 can be written as [5]

$$\sigma_R = \sigma_B C_F \frac{\alpha_s}{2\pi} \int \mathrm{d}z \frac{\mathrm{d}p_\perp^2}{p_\perp^2} \left[\frac{1+z^2}{1-z} + \mathcal{O}(p_\perp^2) \right], \tag{1.16}$$

where $p_\perp$ is the transverse momentum of the emitted parton, z is the momentum fraction of the emission and σ_B is the leading-order cross section. The divergences of the previous integral can be regulated by introducing cut-offs, Q_0 and ϵ, and parametrising the divergent regions according to

$$Q_0^2 < p_\perp^2, \qquad \epsilon < z < 1 - \epsilon. \tag{1.17}$$

The integral in Eqn. 1.16 then yields single and double logarithmic terms

$$\propto \frac{\alpha_s}{2\pi} \ln\left(\frac{Q^2}{Q_0^2}\right), \qquad \propto \frac{\alpha_s}{2\pi} \ln\left(\frac{Q^2}{Q_0^2}\right) \ln\left(\frac{1}{\epsilon}\right). \tag{1.18}$$

Here the single logarithm corresponds to the collinear divergences while the double logarithm corresponds to collinear and soft regions of the phase-space. Note that according to the theorem of Kinoshita, Lee and Nauenberg (KLN) [12–14] those singularities are cancelled at all orders in α_s in any observable that is not sensitive to soft and collinear emission of partons; those observables are called *infrared safe*. In particular, for the full inclusive cross section of $e^+e^- \to$ hadrons the divergences coming from the radiative correction are cancelled by identical singularities of opposite sign arising from the $\mathcal{O}(\alpha_s)$ virtual correction.
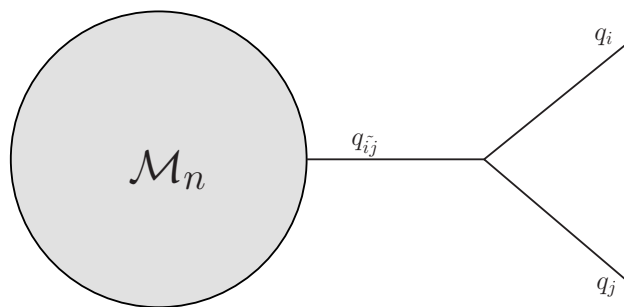
Figure 1.3: Correction to a process with n-particles in the final state and matrix element $\mathcal{M}_n$. The correction is due to the branching of an external parton $q_{\tilde{ij}} \to q_i q_j$.

1.2.2 Splitting functions

The factorization in Eqn. 1.16 can be generalized to the case of a process with n particles in the final state and the parton $\tilde{ij}$ splitting into two particles i and j, as shown in Fig. 1.3. The matrix element will contain the factor from the propagator,

$$\frac{1}{q_{\tilde{ij}}^2 - m_{\tilde{ij}}^2}, \tag{1.19}$$

which is singular in the limit that the emitter is on-shell ($q_{\tilde{ij}}^2 \to m_{\tilde{ij}}^2$). In the massless limit the previous factor becomes

$$\frac{1}{E_i E_j (1 - \cos\theta_{ij})}, \tag{1.20}$$

which shows that the divergences appear in the limit that either an external parton is soft ($E_{i,j} \to 0$) or the external partons are collinear ($\theta_{i,j} \to 0$).

The main result of QCD is that, in the enhanced soft and collinear limit, those singularities are factorized into a universal set of Altarelli-Parisi *splitting functions* [15], $P_{\tilde{ij} \to ij}(z)$, according to

$$d\sigma_{n+1} = d\sigma_n \frac{\alpha_s}{2\pi} \frac{dp_\perp^2}{p_\perp^2} dz P_{\tilde{ij} \to ij}(z). \tag{1.21}$$

These splitting functions are **universal** in the sense that they do not depend on the underlying process but only on the parton species involved in the branching. In the following we will briefly discuss the case of emission of a gluon and for any further detail see Ref. [5]. The main step consists of writing the matrix element, in the on-shell limit, in terms of the Sudakov decomposition of the emitted particle momenta. For the branching $p_q \equiv p \to q_q q_g$ we obtain

$$q_q^\mu = zp^\mu + \frac{p_\perp^2}{2zp \cdot n} n^\mu + k_\perp^\mu, \tag{1.22}$$

$$q_g^\mu = (1-z)p^\mu + \frac{p_\perp^2}{2(1-z)p \cdot n} n^\mu - k_\perp^\mu, \tag{1.23}$$

where p is the momentum of the emitter, the reference vector n is a light-like vector with three-momentum opposite to that of p, $p_\perp$ is the transverse momentum of the emission and $k_\perp$ is chosen so that $k_\perp^2 = -p_\perp^2$. Note that the previous results hold in the on-shell limit, where $p^2 \simeq 0$. The modulus squared of the matrix element summed over colours and spins factorizes

$$|\bar{\mathcal{M}}_{n+1}|^2 = 8\pi\alpha_s \frac{1}{(q_q \cdot q_g)} \frac{1+z^2}{1-z} |\bar{\mathcal{M}}_n|^2 + \mathcal{O}(p_\perp). \tag{1.24}$$

This result has to be considered together with the corresponding radiative phase-space measure written in terms of z and $p_\perp$. At $\mathcal{O}(p_\perp)$ we have [5]

$$\mathrm{d}\Phi_{n+1} = \mathrm{d}\Phi_n \frac{\mathrm{d}z \mathrm{d}p_\perp^2}{16\pi^2 z(1-z)}. \tag{1.25}$$

In this way we obtain

$$\mathrm{d}\sigma_{n+1} = \mathrm{d}\sigma_n \frac{\mathrm{d}p_\perp^2}{p_\perp^2} \mathrm{d}z \frac{\alpha_s}{2\pi} P_{q\to qg}, \tag{1.26}$$

where

$$P_{q\to qg} = C_F \left[\frac{1+z^2}{1-z} \right] \tag{1.27}$$

is the Altarelli-Parisi splitting function for the $q \to qg$ branching. The collinear splitting functions for different flavour branching can be derived in a similar way giving

$$P_{g\to gg} = C_A \left[\frac{z}{1-z} + \frac{1-z}{z} + z(1-z) \right], \tag{1.28}$$

$$P_{g\to q\bar{q}} = T_F \left[1 - 2z(1-z) \right], \tag{1.29}$$

where $C_A = N_c$ and $T_F = 1/2$. Eqns. 1.27-1.28 are known in the literature as *unregularized* splitting function because they diverge in the soft gluon limit $z \to 1$[3]. The divergent behaviour can be regularized by using a prescription that is known as *plus prescription*. We will not discussed the regularized version of the splitting functions here and refer the reader to Ref. [5,6] for further details.

Here we have considered the branching from final-state partons, whose branching line is characterised by the virtuality $q^2 > 0$ of the intermediate parton. For this reason it is known as *time-like branching*. The same factorization would be gained for the branching of initial-state emission; in the latter case, the intermediate parton would have a virtuality $q^2 < 0$ and we would refer to it as *space-like branching*.

1.3   The DGLAP equation

In order to illustrate the origin of logarithmic divergences in QCD, we generalize the approach followed in the previous section to the case of multiple collinear emission,

---

[3]The splitting function $P_{g\to gg}$ has also singularity at $z = 0$, but this divergence can be mapped to $z = 1$ given the $z \to 1 - z$ symmetry of the function [5].
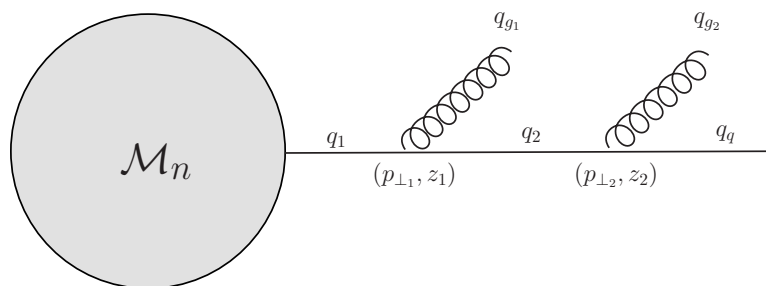
Figure 1.4: Real emission correction to a general process with n particles in the final state. The correction is due to the emission of gluons.

i.e. when more than one branching happens along the branching line. We will start from a two-particle branching (Sect. 1.3.1) before illustrating the case of multi-particle emission in Sect. 1.3.2. In the latter, we will show that the DGLAP equation provides a leading-logarithm (LL) resummation of these divergences.

1.3.1 Two-particle emissions

We start from the simple case, of two collinear gluons emission, as shown in Fig. 1.4. The approach leading to the factorization shown in Eqn. 1.26 relied on the fact that the emitter was on-shell. Going backwards along the branching line in Fig. 1.4 we see, from Eqns. 1.22 and 1.23, that at $(p_{\perp_2}, z_2)$ the emitter has virtuality given by

$$q_2^2 = (q_q + q_{g_2})^2 = \frac{p_{\perp_2}^2}{z_2(1 - z_2)}. \tag{1.30}$$

When we consider the branching at $(p_{\perp_1}, z_1)$, this finite virtuality can be neglected in the limit $q_1^2 \gg q_2^2$. The latter condition is known in the literature as *strong ordering*. From Eqn. 1.30 we find that, for non-soft emission, the strong ordering condition can be expressed as

$$p_{\perp_1}^2 \gg p_{\perp_2}^2. \tag{1.31}$$

Following the approach of the previous section, in the non-soft, collinear limit of Eqn. 1.26, we find that the emission illustrated in Fig. 1.4 is proportional to

$$\left(\frac{\alpha_s}{2\pi}\right)^2 \int_{Q_0^2}^{Q^2} \frac{dp_{\perp_1}^2}{p_{\perp_1}^2} \int_{Q_0^2}^{p_{\perp_1}} \frac{dp_{\perp_2}^2}{p_{\perp_2}^2} = \frac{1}{2} \left(\frac{\alpha_s}{2\pi}\right)^2 \ln^2\left(\frac{Q^2}{Q_0^2}\right). \tag{1.32}$$

Note that the presence of double logarithms holds because of the strong ordering condition; in fact if we invert the relation in Eqn. 1.31, $p_{\perp_1}^2 \ll p_{\perp_2}^2$, we get only a single logarithm while the strong coupling is still at a power of two: this configuration is therefore subleading. From Eqn. 1.32 it follows that the description of exclusive jet observable contains the logarithmic terms of Eqn. 1.18. If the resolution parameters are small those logarithms will dominate the observable. Moreover, each power of α_s will introduce a large logarithm, invalidating the truncation of the perturbative series. For this reason we need an algorithm to rewrite the integral in such a way that the perturbative approach is still valid: *resummation*. The DGLAP equation

9

provides a *leading-order resummation*, as we will see in the next section. Before concluding this section it is important to note that the strong ordering condition (Eqn. 1.31) implies not only an ordering in the transverse momenta, but also in the opening angle of the emission or any other variable parametrising the collinear limit of the branching. The variable with which the strong ordering variable is applied is called the *ordering variable* and it is of main interest for parton shower. Different choices of ordering variable do not change the treatment of the leading logarithms (LL) but only the subleading terms.

1.3.2 Multi-particle emissions

In Sect. 1.2 we saw that the branching formalism is based on a picture of partons evolving in an ordering variable, t, and undergoing an emission while evolving from $t \to \delta t$ with probablility $\mathcal{P}_{\tilde{ij} \to ij}(t)\delta t$; from Eqn. 1.21, this is given by

$$\mathcal{P}_{\tilde{ij} \to ij}(t)\delta t = \frac{\delta t}{t} \int_0^1 dz \frac{\alpha_s}{2\pi} P_{\tilde{ij} \to ij}(z). \tag{1.33}$$

Here and in the following the strong coupling is $\alpha_s \equiv \alpha_s(t)$. The DGLAP equation [15, 16] is defined as

$$t \frac{\partial f_i(x,t)}{\partial t} = \int_0^1 dz \frac{\alpha_s}{2\pi} P(z) \left[\frac{1}{z} f_i \left(\frac{x}{z}, t \right) - f_i(x,t) \right] \tag{1.34}$$

and describes how $f_i(x,t)$ develops in t. The functions $f_i(x,t)$ are called *parton density* (*fragmentation*) functions and describe the probability of finding a parton species i with momentum fraction x of the incoming (outgoing) hadron at a scale given by the ordering variable t. Using the plus prescription mentioned in Sect. 1.2.2, Eqn. 1.34 can be written in terms of regularized splitting functions and the integration region becomes $x \le z \le 1$. However, in the Monte Carlo approach it is preferable to use unregularized splitting functions and remove the divergences in the following way.

We consider the *Sudakov form factor*,

$$\Delta(t) = \exp \left[-\int_{t_0}^t \frac{dt'}{t'} \int_\epsilon^{1-\epsilon} dz \frac{\alpha_s}{2\pi} P(z) \right], \tag{1.35}$$

which is defined as being the probability for evolving from $t \to t_0$. Here we have introduced an explicit cut-off ϵ to remove the singularities. The definition of this cut-off is to some extent a matter of choice about what we classify as an *unresolvable* emission, which involves the radiation of an undetectable soft parton. In terms of the Sudakov form factor, Eqn. 1.34 becomes

$$t \frac{\partial}{\partial t} \left(\frac{f_i(x,t)}{\Delta(t)} \right) = \frac{1}{\Delta(t)} \int_\epsilon^{1-\epsilon} \frac{dz}{z} \frac{\alpha_s}{2\pi} P(z) f_i \left(\frac{x}{z}, t \right) \tag{1.36}$$

and for multiple parton species emission, $\tilde{ij} \to ij$, it becomes

$$t \frac{\partial}{\partial t} \left(\frac{f_i(x,t)}{\Delta_i(t)} \right) = \frac{1}{\Delta_i(t)} \sum_{i,j} \int_\epsilon^{1-\epsilon} \frac{dz}{z} \frac{\alpha_s}{2\pi} P_{\tilde{ij} \to ij}(z) f_{\tilde{ij}} \left(\frac{x}{z}, t \right), \tag{1.37}$$

which shows no logarithmic enhancement. Therefore the strongly-ordered DGLAP equation resums the leading logarithmic contributions.

1.4 Soft emission

So far we have discussed only collinear singularities. Now we consider soft singularities. Returning to the branching in Fig.1.3, we consider the case of a soft emitted gluon, $i.e$ $E_g \simeq 0$, with momentum

$$q_g^\mu = E_g(1; \mathbf{n}), \tag{1.38}$$

where $\mathbf{n}$ is a unit vector defining the direction of the gluon. In the limit $E_g \to 0$ the matrix element factorises into a product of a spin independent *eikonal factor*, a colour factor and the coupling constant

$$\mathcal{M}_{n+1} = g_s t_{ab}^c \frac{q_q \cdot \epsilon(q_g)^{*c}}{q_q \cdot q_g} \mathcal{M}_n^{ab}. \tag{1.39}$$

Note that the form of this factorisation is universal in the sense that it describes the emission of a soft gluon from any of the external on-shell partons, with only the colour factor depending on the emitting parton species (ab). The cross section will then be given by summing Eqn. 1.39 over all external partons and squaring: the result is given by [5]

$$d\sigma_{n+1} = d\sigma_n \frac{dE_g}{E_g} \frac{d\Omega}{2\pi} \frac{\alpha_s}{2\pi} \sum_{i,j} C_{ij} W_{ij}, \tag{1.40}$$

where the sum over i and j refers to all possible pairs of external partons. Here C_{ij} contains the colour factors while W_{ij} is the *radiation function*. Note that in the collinear limit, Eqn. 1.40 approximates the general soft-collinear form of Eqn. 1.21 and treats soft and collinear singularities on an equal footing: this is the basic idea of angular ordered parton showers.

In the massless limit, the radiation function is given by

$$W_{ij} = E_g^2 \frac{p_i \cdot p_j}{p_i \cdot q_g p_j \cdot q_g}. \tag{1.41}$$

The radiation function can be written in terms of the opening angle between the partons i, j, and g as

$$W_{ij} = \frac{1 - \cos\theta_{ij}}{(1 - \cos\theta_{ig})(1 - \cos\theta_{jg})}. \tag{1.42}$$

The previous equation shows that Eqn. 1.40 contains soft singularities, because of the $\frac{1}{E_g} term$, together with collinear singularities (see Eqn. 1.42), as we expect. Eqn. 1.42 can be written in terms of

$$W_{ij}^{(i,j)} = \frac{1}{2} \left(W_{ij} + \frac{1}{1 - \cos\theta_{(i,j)g}} - \frac{1}{1 - \cos\theta_{(j,i)g}} \right) \tag{1.43}$$

11

as

$$W_{ij} = W_{ij}^{(i)} + W_{ij}^{(j)}, \tag{1.44}$$

where the superscript (i, j) is meant to be either the particle i or j. In Eqn. 1.44 the collinear singularities $\theta_{ig} \to 0$ are separated from $\theta_{jg} \to 0$ and the interference between them has been removed.

It is convenient to perform the integral over the azimuthal angle of the gluon, relative to the parton to which the gluon is collinear and this gives [5]

$$\int_0^{2\pi} \frac{\mathrm{d}\phi_{(i,j)g}}{2\pi} W_{ij}^{(i,j)} = \frac{1}{1 - \cos_{(i,j)g}} \Theta(\theta_{ij} - \theta_{(i,j)g}), \tag{1.45}$$

which shows that the interference is completely destructive outside of a cone centred along the line (i, j) and extending as far as the line (j, i): the radiation function then exhibits a property of *angular ordering* [17–24]. For massive partons, the same angular ordering applies but with an inaccessible area collinear to the massive quarks, the *dead cone* [25].

1.5   Monte Carlo event generators

The main general purpose Monte Carlo events generators used to be Pythia [26] and HERWIG [27]. They were based on FORTRAN language and despite the fact that they were very successful in describing several physical processes, maintaining them became impractical as they grew. For this reason they were rewritten in an object-oriented structure in the C++ language as Pythia 8 [28] and Herwig++ [3]. In the meantime another event generator was also developed: SHERPA [29]. These event generators present a common structure that provides the simulation but have notable differences in the details of the simulation itself. In this section we describe the general features of Monte Carlo event generators. Later we will give more details on Herwig++, which is the event generator used for the present work.

1.5.1   The structure

Monte Carlo event generators provide an event-by-event description of collisions at particle accelerator experiments, supplying as complete as possible a simulation of the physics involved. The event-by-event flexibility guarantees predictions for any number of observable quantities and the application of the experimental cuts to these predictions.

Event generators simulate physics in two different domains: *perturbative* and *non-perturbative*. Those regions are separated by a *hadronization scale*, which is typically of the order of 1 GeV. At higher scales the asymptotic freedom guarantees that the strong coupling is small and perturbation theory can be applied to describe the interactions of free partons: the *hard subprocess*. However, at lower scales confinement dictates that only colour singlets exist: hadronic states are observed and not free partons. This physics will be described by non-perturbative models: these are phenomenological models based on physical assumptions, which depend on free parameters that need to be *tuned* to experimental data.

Monte Carlo event generators provide a means, via a parton shower, of evolving from the hard scale, where partons are produced at a fixed order in perturbation theory, to the soft scale, where non-perturbative models are applied. The perturbative physics consists of three main parts: the hard subprocess, perturbative decays and the parton shower. The hard subprocess is generally calculated at leading-order with a tree-level matrix element. Each external leg undergoes multiple soft and collinear branching, the parton shower, which evolves from the hard scale down to the hadronization scale. This corresponds to a DGLAP resummation of the LL terms. Moreover, the unstable particles decay according to the decay rate calculated in perturbation theory. The hadronization models, describing the way stable hadrons are created by final state partons, are then applied. The interaction of the remnants of the beam particles, after the partons of the hard scattering have been extracted, also needs to be simulated: this is done with a non-perturbative model describing the *underlying events*. In particular, the underlying events are the products of two components: the hadron production in multiple parton interactions (MPI) and the beam-beam remnants (BBR), which is the result of the hadronization of the beam partonic constituents that did not participate in the hard scattering.

1.6   The parton shower

The parton shower is a formalism devoted to the simulation of scattering events of particle physics in colliders. Continuing along the same lines as Sect. 1.3, where we illustrated final state branching, we will start by describing a final state parton shower in Sect. 1.6.1. In Sect. 1.6.2 we will investigate the need for a backward evolution for initial state radiation and then take a brief look at angular-ordered parton showers in Sect. 1.6.3. We will conclude the present section by highlighting the main features of the parton shower used in the present work: Herwig++ in Sect. 1.6.4 and in Sect. 1.6.5 the dipole shower of Ref. [4].

1.6.1   Final state parton shower

The parton shower is based on the fact that the branching formalism of the DGLAP equation (Eqn. 1.37) can be interpreted in a probabilistic way as *Markov process* (see Refs. [30–33]), describing independent branchings. This interpretation is seen by integrating[4] Eqn. 1.37 with respect to the ordering variable and writing it as

$$f_i(x,t) = \Delta_i(t)f_i(x,t_0) + \int_{t_0}^{t} \frac{\mathrm{d}t'}{t'} \frac{\Delta_i(t)}{\Delta_i(t')} \sum_{\tilde{i}j} \int_{\epsilon}^{1-\epsilon} \frac{\mathrm{d}z}{z} \frac{\alpha_s}{2\pi} P_{\tilde{i}j \to ij} f_{\tilde{i}j}\left(\frac{x}{z}, t'\right). \quad (1.46)$$

The previous equation can be solved by iterative substitution and has a very interesting probability interpretation. The first term on the right hand side defines the probability that no resolvable emission happens in evolving from t down to the hadronization scale t_0. The second term corresponds to the probability of having a branching $\tilde{i}j \to ij$ at a scale t' and momentum fraction z: this is given by the

---

[4]We proceed along the same lines as Sect. 1.3, where we derived the DGLAP equation (Eqn. 1.37) for final state branching; therefore, we refer to a final state parton shower here.

probability of having no resolvable emission from t to t', $\frac{\Delta_{\tilde{i}j}(t)}{\Delta_{\tilde{i}j}(t')}$, multiplied by the probability of undergoing a branch at scale t' and momentum fraction z. The recursive approach requires that the function $f_i(\frac{x}{z}, t')$ in the second term undergoes the same evolution by branching at (t'', z'), with $t' < t'' < t_0$ and $z' \neq z$.

Conventionally the parton shower evolution is expressed by a generating functional, which describes all configurations and corresponding probabilities of the states accessible to the shower [5]. This parton shower resums the effect of enhanced collinear emission to all orders in α_s in the LL approximation. In practice, it is generated following the *parton shower algorithm*. This consists of calculating the scale of the emission by generating random numbers $\mathcal{R}, \mathcal{R}' \in [0, 1]$, solving

$$\mathcal{R} = \frac{\Delta_i(t)}{\Delta_i(t')} \tag{1.47}$$

for t and calculating the momentum fraction of the branching, z, by solving[5]

$$\int_\epsilon^z \mathrm{d}z' \frac{\alpha_s}{2\pi} P(z') = \mathcal{R}' \int_\epsilon^{1-\epsilon} \mathrm{d}z' \frac{\alpha_s}{2\pi} P(z'). \tag{1.48}$$

1.6.2   Initial state parton shower

The branching algorithm described above generates what is known as *forward evolution* or *final state parton shower*. At each branching a parton with *timelike* momentum is emitted and the emitting particle moves towards a lower virtuality.

In the initial state parton shower the incoming parton, extracted from the incoming hadron, has negative (*spacelike*) virtuality which increases, to less negative values, when the particle moves towards the hard scattering. The initial state shower describes parton emissions in the LL approximation via the DGLAP equation. The DGLAP equation for initial state branchings is identical to the one for final state branching. For this reason, we could plan to resolve it by following the same approach used in Sect. 1.3: a parton is selected from the incoming hadron and showered from the hadronic scale to the hard scale. This approach has two drawbacks: it is ambiguous in the shower scheme and inefficient in the event generation. In fact, on the one hand it is not easy to decide which parton corresponds to the incoming parton of the hard scattering and the scale at which the shower should be stopped to generate the hard scattering. On the other hand we want the incoming partons of the hard scattering to interact at the correct value of the hard scale in order to form a particular boson; forward evolution would require that a high proportion of events must be rejected.

Consequently, a *backward evolution* scheme is applied. It works by generating the hard process first and then showering the initial state parton backwards from the hard scale to the hadronization scale, where the partons are assigned to the incoming hadrons. In this case the probability of evolving a particle of flavour i backwards from (t_2, x) to (t_1, x) with no resolvable emission is given by the modified Sudakov form factor

$$\Pi_i(t_1, t_2; x) = \Delta(t_1, t_2) \frac{f_i(x, t_1)}{f_i(x, t_2)}, \tag{1.49}$$

---

[5]The choice of the cut-off ϵ in practice defines what is considered to be a resolvable emission.

where $\Delta(t_1, t_2) = \frac{\Delta(t_2)}{\Delta(t_1)}$. The branchings are then generated according to the probability given by the product of the probability of having no resolvable emission (Eqn. 1.49) and the probability of emitting a parton at (t, z), given by

$$\frac{\alpha_s}{2\pi} P_{\tilde{ij} \to ij}(z) \frac{f_{\tilde{ij}}(\frac{x}{z}, t)}{z f_i(x, t)}. \tag{1.50}$$

In practice this is generated using a Monte Carlo algorithm analogous to the one discussed for the timelike case.

1.6.3 The angular-ordered parton shower

So far we have discussed the parton shower formalism including only the collinear emission. Soft gluon emission can be included by extending the approach described in Sect. 1.4 to the case in which a soft gluon is emitted by any number of external partons in a parton shower configuration and by iterating that to any number of soft gluon emissions [25]. It has been shown that coherent soft gluon effects can be taken into account at LL approximation by choosing the ordering variable of the parton shower to be the opening angle of emission [34]. A simple modification can be made to the parton shower formalism, taking the ordering variable to be the opening angle of emissions: this is know as an *angular-ordered* parton shower. From our discussion of the strong ordering of parton shower emission, such a change in ordering variable does not change the description of non-soft emissions in the LL approximation.

1.6.4 Herwig++ parton shower

Herwig++ is an angular-ordered parton shower. The ordering variable is chosen to be

$$\tilde{q}^2 = \frac{q_{\tilde{ij}}^2 - m_{\tilde{ij}}^2}{z(1-z)}, \tag{1.51}$$

where z is the light-cone momentum fraction in the Sudakov decomposition, $q_{\tilde{ij}}^2$ is the virtuality and $m_{\tilde{ij}}$ the mass of the emitting particle. In the collinear limit, the evolution variable behaves as

$$\tilde{q} = E_{\tilde{ij}} \theta_{ij} + \mathcal{O}(\theta_{ij}^2); \tag{1.52}$$

therefore it takes into account coherent soft gluon emission via angular ordering.

Phase-space

Now we consider the allowed phase-space in Dalitz variables. For illustrative purposes, here we only discuss the phase-space coverage for a final state parton shower; this choice is made with the aim of comparing the results with those discussed in Sect. 1.2.1.
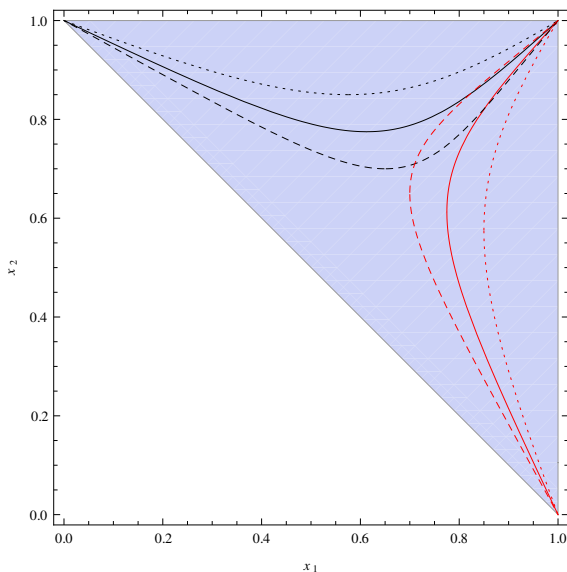
Figure 1.5: Contours of constant $\tilde{k} = 0.6$ (dotted), $\tilde{k} = 0.9$ (solid) and $\tilde{k} = 1.2$ (dashed) in Dalitz variables. Emissions of parton 1 are depicted in black while those for parton 2 are in red. The shaded region is the allowed phase-space region for the process $e^+e^- \to$ hadrons (cf. Fig. 1.2).

Consider the QCD shower for the hard subprocess shown in Fig. 1.1. The Dalitz variables are defined as (cf. Ref [35])

$$x_1 = 1 - b + c - z(1-z)\tilde{k}, \tag{1.53}$$

$$x_2 = (2 - x_1)r + (z - r)\sqrt{x_1^2 - 4c}, \tag{1.54}$$

where

$$b = \frac{m_2^2}{Q^2}, \quad c = \frac{m_1^2}{Q^2}, \tag{1.55}$$

$$r = \frac{1}{2}\left[1 + \frac{b}{1 + c - x_1}\right]. \tag{1.56}$$

The dimensionless evolution variable is $\tilde{k} = \frac{\tilde{q}^2}{Q^2}$ and the initial condition for it provides the limit to the phase-space region that is accessible from each progenitor.

For simplicity we consider the massless case, $i.e.$ $m_1 \simeq m_2 \simeq 0$, and we plot a contour for three different values of $\tilde{k}$, Fig. 1.5.

The dotted curves show radiation for $\tilde{k} = 0.6$, the solid lines have $\tilde{k} = 0.9$ while the dashed ones have $\tilde{k} = 1.2$. The phase-space coverage strongly depends on the evolution variable and the area of the dead zone decreases as $\tilde{k}$ increases. The shaded region describes the physically allowed phase-space region, as already discussed in Sect. 1.2.1. Curves have been plotted in different colours to distinguish the emission of parton 1 (black) from parton 2 (red).

In the case of an asymmetric initial condition the contour curves (red dashed) are shown in Fig. 1.6. In this case we choose $\tilde{k} = 0.6$ for one of the progenitors and its inverse for the other progenitor. The default initial condition is $\tilde{k} = 1$ (solid black
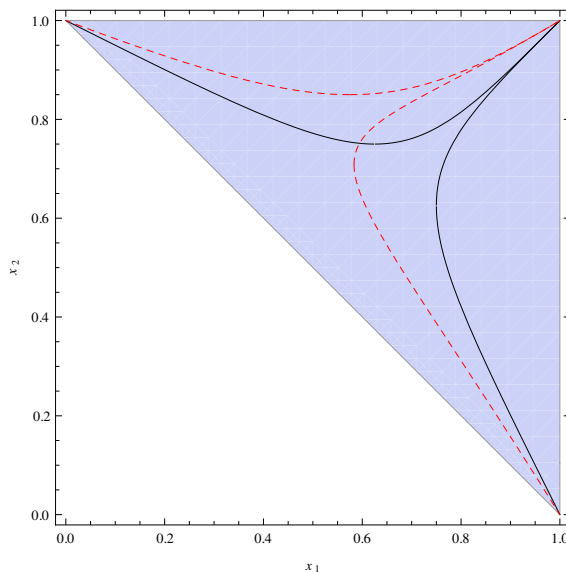
Figure 1.6: Contours of constant $\tilde{k}$ for the parton 1 and $1/\tilde{k}$ for parton 2. We choose $\tilde{k} = 0.6$, dashed red line, and $\tilde{k} = 1$, solid black line. The solid black curves correspond to the default initial condition. The shaded region is as described in Fig. 1.5

line). It provides the best, symmetric, coverage of the physically allowed phase-space region.

1.6.5 Dipole shower

In Sect. 1.2 we described the $1 \rightarrow 2$ branching in terms of the usual *collinear approximation*. Within this formalism the outgoing momenta are given by Eqns. 1.22 and 1.23, and the cross section factorises in terms of splitting functions depending on the momentum fraction of the emission, which is in general defined as

$$z = \frac{n \cdot q_q}{n \cdot p}, \tag{1.57}$$

where n is a gauge vector in the light-cone gauge introduced in Sect. 1.2.

Dipole-type showers are based on the generalization of this picture, by introducing **exact energy-momentum conservation** within the splitting[6] $p_i, p_j \rightarrow q_i, q, q_j$, which is obtained by requiring

$$n = p_j, \quad q_j = \left(1 - \frac{p_\perp^2}{2p_i \cdot p_j z(1-z)}\right) p_j. \tag{1.58}$$

With this choice, we force the spectator to absorb the longitudinal recoil of the splitting; this is known as *recoil strategy*.

Within this framework the $n + 1$ final-state matrix element squared, summed

---

[6]Here and in the following (q_i, q, q_j) stands for (emitter, emission, spectator).

over all collinear configurations, is

$$_{n+1}\langle\mathcal{M}(q_1,...,q_{n+1})|\mathcal{M}(q_1,...,q_{n+1})\rangle_{n+1} \to$$

$$\sum_{i=1}^{n}\sum_{j,k\neq i}\frac{4\pi\alpha_s}{q_i\cdot q_k}P_{ik}(z)|_{n=p_j}\,{}_n\langle\mathcal{M}(q_1,...,p_i,...,q_n)|\mathbf{C}_{ij}|\mathcal{M}(q_1,...,p_i,...,q_n)\rangle_n \quad (1.59)$$

where

$$\mathbf{C}_{ij} = -\frac{\mathbf{T}_i\cdot\mathbf{T}_j}{\mathbf{T}_i^2} \quad (1.60)$$

is the colour correlation operator introduced in [36]. This operator can be included because each amplitude $|\mathcal{M}\rangle$ is a colour singlet, *i.e.*

$$\sum_{i=1}^{n}T_i^2 + \sum_{i=1}^{n}\sum_{j\neq i}T_i\cdot T_j = 0. \quad (1.61)$$

Ignoring the $g \to q\bar{q}$ splitting, Eqn. 1.59 gives

$$\frac{1}{q_i\cdot q}\frac{z}{1-z}\bigg|_{n=p_j} = \frac{q_i\cdot p_j}{q_i\cdot q\,q\cdot p_j} \qquad \frac{1}{q_i\cdot q}\frac{1-z}{z}\bigg|_{n=p_j} = \frac{q\cdot p_j}{q\cdot q_i\,q_i\cdot p_j}, \quad (1.62)$$

so that the single splitting function $P_{ik}(z)|_{n=p_j}$ defines the **complete, correct soft behaviour** for the dipole i,j (cf. Eqn. 1.41).

However, the fact that the DGLAP splitting functions give the correct soft behaviour is not enough to reproduce the correct Sudakov form factor. In fact the integrand function of Eqn. 1.35, the *soft anomalous dimension*, is changed by the recoil strategy: the next-to-leading logarithm (NLL) coefficient is directly modified by the recoil effect while the LL one turns out to be twice the correct result [34]. The overestimate of the LL coefficient is due to the fact that the phase-space introduces an overlap of the regions available for emission off either parton of the dipole.

To remove this problem we can "continue" the DGLAP splitting function over the phase-space in a way that reproduces the correct soft behaviour whenever we add the modified splitting functions for both legs of the dipole. In other words, following the prescription given in Ref. [36], the eikonal part is replaced by

$$\frac{p_i\cdot p_j}{p_i\cdot q\,p_j\cdot q} \to \frac{p_i\cdot p_j}{p_i\cdot q(p_i+p_j)\cdot q} \quad (1.63)$$

while the collinear part is left unchanged. In this way, the regions describing soft emission off either leg of the dipole separate and the correct anomalous dimension is recovered with recoil effect entering only beyond leading logarithm (BLL). Moreover, the exact factorisation of the phase-space in terms of the splitting variables is provided with no kinematic approximation. However, for initial-state radiation, using the Catani-Seymour prescription, this method has shortcomings; in particular, for intial-initial dipoles, a final state singlet receives non-vanishing transverse momentum from the very first shower emission only and the spectator is left unchanged. This is not sufficient for the description of the whole final-state spectrum.

The dipole shower used in the present work is part of a program called **Match-box** and the algorithm is implemented as an add-on module of the **Herwig++** event

generator; it implements the Catani-Seymour prescription and provides a formalism that overcomes the highlighted shortcomings [4]. The kinematics for initial state emitter and/or spectator are described by considering the physical splitting process and keeping exact momentum conservation. The spectator is forced to take the longitudinal recoil of the splitting only. Backwards evolution is used and the transverse momentum of the emitting particle is migrated to the final state by re-aligning the incoming partons to the beam axes at the end of the evolution. Moreover, within a dipole-type shower it is difficult to maintain the strong angular ordering that is related to the $1 \to 2$ nature of the description; ordering in transverse momentum of the emitted particle is much more natural in this case. As we will see in the next section, this feature removes complications when implementing the NLO correction of the hard process into the parton shower.

Phase-space

We now consider the phase-space coverage for emission of a final-final dipole, in the Dalitz variables, for the massless limit of the dipole shower of Ref. [4]. For a splitting $(p_i, p_j) \to (q_1, q_2, q_j)$, the Dalitz variables are defined in terms of

$$q_1 = z p_i + \frac{p_\perp^2}{z s_{ij}} p_j + k_\perp, \tag{1.64}$$

$$q_2 = (1-z) p_i + \frac{p_\perp^2}{(1-z) s_{ij}} p_j - k_\perp, \tag{1.65}$$

respectively, where $k_\perp^2 = -p_\perp^2$, $s_{ij} = 2 p_i \cdot p_j$, $k_\perp \cdot p_{i,j} = 0$ and $z = \frac{p_j \cdot q_1}{p_i \cdot p_j}$. This gives

$$x_1 = z + \frac{p_\perp^2}{z s_{ij}}, \tag{1.66}$$

$$x_2 = 1 - \frac{p_\perp^2}{z(1-z) s_{ij}}. \tag{1.67}$$

The boundaries are given by [37]

$$\mu^2 < p_\perp^2 < \frac{s_{ij}}{4} \qquad\qquad z_\pm = \frac{1}{2}\left[1 \pm \sqrt{1 - \frac{4 p_\perp^2}{s_{ij}}}\right]. \tag{1.68}$$

In Fig. 1.7 we show the allowed phase-space region for a dipole of mass $s_{ij}^{1/2} = 100$ GeV and $\mu = 5$ GeV. The shaded region shows the emissions off parton 1. The straight grey lines define emission at fixed values of z; $z = 0$ along $x_1 = 1 - x_2$ and $z = 1$ along $x_1 = 1$. The curved lines define emission at fixed values of $p_\perp$; $p_\perp = 0$ at the border of the shaded region and increases when the area enclosed by the curved grey line decreases. The solid black line is the region accessible for emissions off parton 2. The two regions overlap, as discussed previously, and almost the whole physical phase-space is available in this case, apart from regions near the singularities, which are exaggerated in our case for illustrative purposes; *i.e* the infrared cut off has been chosen to be high.

Dipole showers provide a very good description of the phase-space, due to the exact momentum conservation that they are based on.
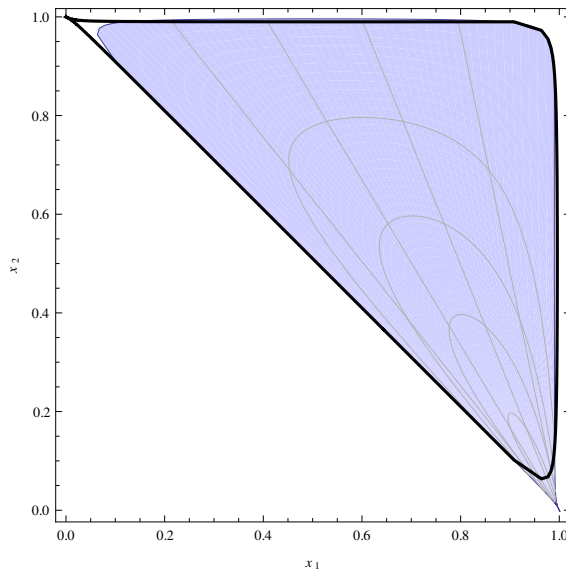
Figure 1.7: Allowed phase-space regions in terms of Dalitz variables. The blue region is accessible to the emission of parton 1. The contourplot shows curved grey lines, which define emission at fixed $p_\perp$, and straight grey lines at fixed z. The black solid line defines the area accessible to parton 2.

1.7 Matching parton shower and NLO corrections

The parton shower is an essential tool for simulating high-multiplicity final-states. Traditionally leading-order matrix elements have been used in these simulations together with the parton shower approximation. However, in recent years different approaches have been developed in order to improve the accuracy of the description by including the next-to-leading order matrix element.

In this section we describe the NLO matching technique that combines parton shower and NLO calculations. We start by giving an overview of the subtraction method in Sect. 1.7.1, and matching schemes (Sect. 1.7.2), before highlighting the POWHEG method and the way in which it has been implemented in the shower (Sect. 1.7.3).

1.7.1 Catani-Seymour subtraction method

The NLO cross section can be written as

$$\mathrm{d}\sigma_{NLO} = B(\Phi_n)\mathrm{d}\Phi_n + V_0(\Phi_n)\mathrm{d}\Phi_n + R_0(\Phi_{n+1})\mathrm{d}\Phi_{\mathrm{n+1}}, \tag{1.69}$$

where $B(\Phi_n)$ is the born, $V_0(\Phi_n)$ the virtual and $R_0(\Phi_{n+1})$ the radiative contributions. V_0 and R_0 are both divergent, as denoted by the subscript "0"; in particular, the ultra-violet divergences appear only in the virtual contribution, while the infrared appear in both. The ultra-violet singularities are removed by renormalisation, as discussed in Sect. 1.1.3.

The infrared divergences arise when an external final-state parton becomes soft or collinear to another final-state parton. These singularities can be parametrised using

dimensional regularization: the divergent contributions are evaluated in $d = 4 - 2\epsilon$ dimensions, where they are integrable. In this way, the singularities appear in terms of poles in ϵ. The KLN theorem [12–14] dictates that these divergences must cancel when summing up both contributions: this gives a fully inclusive cross section that is finite for infrared-safe observables. Note that the radiative piece could contain infrared singularities coming from a configuration in which an initial parton is collinear to a final one: these divergences are not cancelled by the virtual piece but rather factorised into the definition of physical parton density functions (PDFs).

However, for less inclusive cross section the KLN theorem can not be applied and the infra-red safe observable

$$O = \int \mathrm{d}\Phi_n O_n(\Phi_n)\left[B(\Phi_n) + V_0(\Phi_n)\right] + \int \mathrm{d}\Phi_{n+1} O_{n+1}(\Phi_{n+1}) R_0(\Phi_{n+1}) \qquad (1.70)$$

can be calculated using Monte Carlo method as long as we have a prescription that removes the singularities. The *subtraction procedure* is an algorithm that provides a set of counterterms, $C^\alpha(\Phi_{n+1})$, so that the contributions

$$R(\Phi_{n+1}) = R_0(\Phi_{n+1}) - \sum_\alpha C^\alpha(\Phi_{n+1}), \qquad (1.71)$$

$$V(\Phi_n) = V_0(\Phi_n) + \sum_\alpha \int \mathrm{d}\Phi_r C^\alpha(\Phi_{n+1}) \qquad (1.72)$$

are finite. To this end the counterterms need to be defined such that they show the same divergent part as the radiative correction in each divergent region α. Moreover, if the C^α can be integrated in the radiative phase-space, $\mathrm{d}\Phi_r$, yelding poles in $\frac{1}{\epsilon}$ which cancel those in V_0, the NLO differential cross section

$$\mathrm{d}\sigma_{NLO} = \left[B(\Phi_n) + V(\Phi_n)\right]\mathrm{d}\Phi_n + R(\Phi_{n+1})\mathrm{d}\Phi_r\mathrm{d}\Phi_n \qquad (1.73)$$

is finite.

In the present work we use the **general** NLO subtraction scheme, introduced by Catani and Seymour, which provides a **universal** set of counterterms and their corresponding integrals in d-dimensions [36].

1.7.2 NLO matching schemes

Next-to-leading order calculations provide the best description for sufficiently inclusive observables. However, parton showers are needed when we want to calculate observables that are more exclusive and sensitive to higher multiplicity configurations; parton shower simulation evolves from low multiplicity, high energy configuration, described by fixed-order matrix elements, to high multiplicity, low energy configuration, to which universal hadronization models are applied. Therefore the best description will be obtained when we combine NLO corrections and parton showers.

This is complicated because the higher-order matrix element and the parton shower both radiate in some regions of the phase-space, which leads to *double counting*. A prescription, known as a *NLO matching scheme*, is needed to remove this

problem of double counting. The aims of the NLO matching algorithm are to provide the parton shower resummation of soft and collinear emission while giving NLO results for all infrared safe observables in α_s.

In recent years a number of different approaches have been developed to improve the simulation of high transverse momentum, p_T, radiation. In the PYTHIA event generator [26], corrections have been calculated for several different processes [38–41]. Similar corrections have been made to a number of processes in the HERWIG event generator [27, 42–48] and with the new parton shower algorithm in Herwig++ [49–54]. However, these methods are limited to relatively simple processes, only correct the hardest emission in the event and retain the leading-order normalisation of the cross section.

In recent years, there have been numerous efforts to combine higher multiplicity and higher order matrix elements with the parton shower in order to either provide a better description of many hard emissions while retaining the leading-order normalisation [55–63], or the hardest emission together with the correct next-to-leading order normalisation of the cross section by including the full NLO matrix elements.

A number of approaches has been developed to provide a description of the hardest emission together with a next-to-leading order cross section. In the approach of Frixione, Webber and Nason (MC@NLO) [64,65], the parton shower approximation is subtracted from the exact next-to-leading order calculation. This was the first successful systematic scheme for matching next-to-leading order calculations and parton showers and has been applied to many different processes in HERWIG [66–68] and Herwig++ [69–71]. However, this method has two drawbacks: it generates weights that are not positive definite[7] and is implemented in a way that is fundamentally dependent on the details of the parton shower algorithm.

These problems have been addressed with a new matching algorithm, which achieves the same aims as MC@NLO but produces only positive weight events; it was introduced by Nason and called POWHEG (POsitive Weight Hardest Emission Generator) [1, 2].

1.7.3   POWHEG matching

The POWHEG method is based on the fact that if the hardest emission (the emission with the greatest transverse momentum) is generated according to the exact NLO cross section, then all infrared-safe observables will be given according to their NLO distributions; in fact, the subsequent branchings are softer and they only affect observables at next-to-next-to-leading-order.

If the parton shower simulation is ordered in transverse momentum (see dipole showers in Sect. 1.6.5) we can simulate the process by first generating the hardest emission and then evolving the process by using the parton shower from the $(N+1)$-parton final state, forbidding any emissions with transverse momentum above that of the hardest one. However, for shower algorithms that are ordered in other variables,

---

[7]It should be noted that while the presence of negative weight events is not appealling, it does not constitute a problem. These events would be included in any histograms and contribute negative weight to a bin. However, the result should still be positive when we describe infrared-safe observables with sufficiently high statistics.

for example the angular ordering in Herwig++, the hardest transverse momentum emission is not generated as the first emission in the parton shower. Therefore the shower must be reorganized into a *truncated* shower that describes soft emissions at higher evolution scales than the highest p_T emission, together with *vetoed* showers that describe emissions at lower evolution scales that are constrained to be softer than the hardest emission [1, 2].

Within the POWHEG formalism the hardest emission is singled out so that it can be generated separately and then it is generated according to exact NLO formulae.

In the standard Monte Carlo approach, each event is generated according to the leading-order weight $B(\Phi_n)$ and then all external legs initiate a shower. The hardest emission can happen along any of the parton shower lines and it is distributed according to [1, 2]

$$d\sigma^{\text{PS}} = B(\Phi_n)d\Phi_n \left[\Delta_R(\tilde{q}_I, \tilde{q}_0; 0) + \Delta_R(\tilde{q}_I, \tilde{q}_0; p_T)F(\tilde{q}, z)d\tilde{q}dz\right], \tag{1.74}$$

where $\tilde{q}_I$ is the initial scale and $\tilde{q}_0$ is the hadronization scale. Δ_R is called *remnant* Sudakov and is defined as the products of remnant Sudakov form factors for all external legs

$$\Delta_R(\tilde{q}_I, \tilde{q}_0; p_T) = \prod_l \Delta_{R_l}(\tilde{q}_I, \tilde{q}_0; p_T)$$

$$= \exp\left[-\int_{\tilde{q}_0}^{\tilde{q}_I} \sum_{\tilde{ij}} \sum_{\tilde{ij}\to ij} d\mathcal{P}_{\tilde{ij}\to ij}(\tilde{q}, z)\theta(p_T(\tilde{q}, z) - p_{T_h})\right], \tag{1.75}$$

with

$$d\mathcal{P}_{\tilde{ij}\to ij} = \frac{\alpha_s(\tilde{q}, z)}{2\pi} \frac{d\tilde{q}^2}{\tilde{q}^2} dz P_{\tilde{ij}\to ij}(z, \tilde{q}) \tag{1.76}$$

The remnant Sudakov is introduced to overcome the following problem, Ref. [1, 2]. In brief, to single out the hardest emission a θ-function is needed to guarantee that no emission with p_T greater than the hardest emission is generated in truncated and vetoed showers. This θ-function is included in the splitting functions of both new showers but not in Sudakov form factors. However, standard Monte Carlo techniques require that Sudakov form factor and parton shower do have the same splitting functions. In order to make truncated and vetoed showers suitable for a Monte Carlo algorithm, the standard Sudakov form factor is split into pieces: one contains the same θ-function appearing in the splitting functions and is used for the showers, the other contains the opposite θ-function and is called the remnant. The infinitesimal splitting probability summed over all the parton-shower legs is

$$F(\tilde{q}, z)d\tilde{q}dz = \sum_{\tilde{ij}} \sum_{\tilde{ij}\to ij} d\mathcal{P}_{\tilde{ij}\to ij}(\tilde{q}_h, z_h), \tag{1.77}$$

where $(\tilde{q}_h, z_h)$ describes the hardest radiation and the summation over $\tilde{ij}$ denotes summation over the external legs which initiate the parton shower.

The α_s expansion of Eqn. 1.74 is given by

$$d\sigma^{\text{PS}} = B(\Phi_n)d\Phi_n \left[1 + F(\tilde{q}, z)d\tilde{q}dz - \int_{\tilde{q}_0}^{\tilde{q}_I} F(\tilde{q}, z)d\tilde{q}dz + \mathcal{O}(\alpha_s^2)\right]. \tag{1.78}$$

We now manipulate the exact NLO cross section in Eqn. 1.73 to match the form of Eqn. 1.78 and we get

$$
\mathrm{d}\sigma_{NLO} = \left[V(\Phi_n) + \int \mathrm{d}\Phi_r R(\Phi_{n+1}) \right] \mathrm{d}\Phi_n
$$
$$
+ B(\Phi_n)\mathrm{d}\Phi_n \left[1 + \frac{R_0(\Phi_{n+1})\mathrm{d}\Phi_r}{B(\Phi_n)} - \frac{\int R_0(\Phi_{n+1})\mathrm{d}\Phi_r}{B(\Phi_n)} \right]. \qquad (1.79)
$$

The second term in Eqn. 1.79 has the same form as Eqn. 1.78 if we replace

$$
F(\tilde{q}, z) \rightarrow \frac{R_0(\Phi_{n+1})}{B(\Phi_n)}, \qquad\qquad \mathrm{d}\tilde{q}\mathrm{d}z \rightarrow \mathrm{d}\Phi_r. \qquad (1.80)
$$

Accordingly, the Sudakov form factor is defined as

$$
\Delta_R(p_T) = \exp\left[-\int \mathrm{d}\Phi_r \frac{R_0(\Phi_{n+1})}{B(\Phi_n)} \theta(p_T(\Phi_{n+1}) - p_{T_h}) \right] \qquad (1.81)
$$

and the NLO cross section

$$
\mathrm{d}\sigma_{NLO} = \left[V(\Phi_n) + \int \mathrm{d}\Phi_r R(\Phi_{n+1}) \right] \mathrm{d}\Phi_n
$$
$$
+ B(\Phi_n)\mathrm{d}\Phi_n \left[\Delta_R(p_{T_{\min}}) + \Delta_R(p_T)\frac{R_0(\Phi_{n+1})\mathrm{d}\Phi_r}{B(\Phi_n)} \right], \qquad (1.82)
$$

where the cut-off $p_{T_{\min}}$ is introduced to avoid the singular regions of the radiative corrections: this defines what is considered a resolvable emission. Eqn. 1.81 is known in literature as the *modified* Sudakov form factor.

Eqn. 1.82 has the same expression as the exact cross section at NLO, Eqn. 1.69, but also generate the same distribution of the hardest emission, Eqn. 1.74. Therefore, together with the truncated and vetoed showers it satisfies the requirement of a NLO matching prescription. The first term in the square brackets is higher order in α_s and can be implemented by generating an n-body configuration and applying the standard shower. The second term in square brackets defines the distributions of events containing the hardest emission and it is implemented, together with the shower reorganization, within the POWHEG method. Although this is a workable implementation, *i.e.* MC@NLO scheme, it suffers from negative weights since the first term in not positive definite.

The POWHEG method overcomes this problem by introducing

$$
\bar{B}(\Phi_n) = B(\Phi_n) + V(\Phi_n) + \int \left[R(\Phi_n, \Phi_r) - \sum_\alpha C^\alpha(\Phi_n, \Phi_r) \right] \mathrm{d}\Phi_r, \qquad (1.83)
$$

and rewriting the NLO differential cross section, with only differences at NNLO, as

$$
\mathrm{d}\sigma = \bar{B}(\Phi_n)\mathrm{d}\Phi_n \left[\Delta_R(p_{T_{\min}}) + \frac{R(\Phi_n, \Phi_r)}{B(\Phi_n)}\Delta_R(k_T(\Phi_n, \Phi_r))\mathrm{d}\Phi_r \right]. \qquad (1.84)
$$

The POWHEG formalism requires that the n-body configuration is generated according to $\bar{B}(\Phi_B)$. The hardest emission in the event is then generated by using the Sudakov form factor given in Eqn. 1.81. As $\bar{B}(\Phi_B)$ is simply the next-to-leading-order differential cross section integrated over the radiative variables, it is naturally positive, and therefore leads to the absence of events with negative weights.

POWHEG in the Herwig++ parton shower

The POWHEG algorithm is implemented in the Herwig++ parton shower according to the following procedure:

- generate an event according to Eqn. 1.84;

- directly hadronize the small fraction of non-radiative events;

- map the radiative variables parametrising the emission onto the evolution scale, momentum fraction and azimuthal angle, $(\tilde{q}_h, z_h, \phi_h)$, from which the parton shower will reconstruct identical momenta;

- consider the initial N-body configuration generated from $\bar{B}(\Phi_B)$ and evolve the parton emitting the extra radiation from the default starting scale down to $\tilde{q}_h$ using the truncated shower;

- insert a branching with parameters $(\tilde{q}_h, z_h, \phi_h)$ into the shower when the evolution scale reaches $\tilde{q}_h$;

- generate p_T vetoed showers from all external legs.

POWHEG in the dipole shower

The POWHEG scheme is implemented in the dipole shower used in the present work, as summarised in the following:

- generate born-type events, with a weight that is the LO differential cross section, $B(\Phi_n)$;

- generate the hardest emission by using the exact real emission matrix element;

- define the dipole kinematics by inverting the "tilde-mapping" defined in Ref. [36];

- define splitting kernels $P_{n+1+i \to n+2+i}$, with $i = 0, ..., N$ (where N is the multiplicity), to generate a transition from the state $|n + 1 + i\rangle$ to $|n + 2 + i\rangle$;

- feed the dipole shower.

For a given configuration C, the splitting kernel is defined as

$$P_C = \frac{D_C}{\sum_I D_I(\Phi_B, \Phi_R)} \frac{R(\Phi_B, \Phi_R)}{B(\Phi_B) + B_{\text{screen}}(\Phi_B)}. \tag{1.85}$$

In this way all divergences but the divergence associated with D_C are divided out from the real emission matrix element and unpleasant behaviour of the born matrix element, such as peaks due to unstable particles, are flattened out. The term $B_{\text{screen}}(\Phi_B)$ has been introduced on purpose in Eqn. 1.85 and has to be chosen such that it avoids divergences when $B(\Phi_B) \to 0$ and forces the PDF to smoothly tend to zero whenever they oscillate around the origin. It can be shown that parametrizing $B_{\text{screen}}(\Phi_B)$ in term of $p_\perp$ results in the fact that the screen-term must vanish when $p_\perp \to 0$ in order not to spoil the resummation of large logarithms [37].

Note that the present approach is a general description of the POWHEG method and the NLO cross section within this general approach is equivalent to Eqn. 1.84 [37]. The generality of the approach, together with the ability to rigorously calculate fixed-order expansion of the parton showers guarantee that matching at NNLO is possible even if there has been no attempt reported in the literature thus far.

1.8   Summary

QCD is widely accepted as the correct theory of strong interactions. The understanding of QCD is crucial for the success of collider experiments, but it is not enough to describe observables that are sensitive to final-state high multiplicity. The best description is given when NLO QCD corrections and parton showers work together.

The success of the parton shower resides in the flexibility of Monte Carlo event generators, which provide an event-by-event description of the cascade. The parton shower is based on parton branching formalism, which describes soft and collinear emissions in terms of a universal factorised form. These emissions correspond to enhanced emissions that result in LL corrections. Parton showers provide resummation of these LL contribution to all orders in α_s.

Collinear emission is described by a parton shower formulated in terms of an evolution in virtuality, while coherent, soft gluon emission is correctly included by ordering emissions in the opening angle of the branching. Angular ordered parton showers are used in Herwig++. On the other hand, dipole showers are based on a dipole picture of the splitting, which guarantees exact momentum conservation, and an ordering in the transverse momentum of the emission.

These features provide a better description of the allowed phase-space: mainly the whole phase-space is covered without dead regions. The order in transverse momentum guarantees an easier implementation of the matching scheme, such as POWHEG: now the hardest $p_\perp$ emission is the first one and there is no need to reorganize the shower to correct it.

Chapter 2

Implementing the POWHEG method for Higgs production via vector boson fusion in the **Herwig++** parton shower

The Large Hadron Collider (LHC) at CERN is designed to illuminate the nature of electroweak symmetry breaking in the Standard Model [72–75], and in particular discover the Higgs boson. Once the Higgs boson has been observed and its mass determined, it will be crucial to measure the way it couples to gauge bosons and fermions [76, 77]. The most promising processes in which these couplings of the Higgs boson can be measured are gluon-gluon and vector-boson fusion, as shown in Fig.[1] 2.1a. The former consists of a gluon-gluon partonic collision that produces a Higgs boson via a virtual top quark loop [78]. It has the largest cross section for Higgs boson masses of less than $\sim 1\,\mathrm{TeV}$ and will be important for the measurement of the Higgs coupling to the top quark.

Higgs boson production via vector-boson fusion (VBF), despite not having the largest cross section at the LHC, is very useful because of its kinematical structure, characterized by two forward jets[2] and a central Higgs. It is a process in which two incoming fermions each radiate a $W^{\pm}$ or Z^0 boson, which then combine to produce the Higgs boson. VBF is expected to play a fundamental rôle in the measurement of the Higgs boson couplings to gauge bosons and fermions, because it allows for independent observation in different channels: $H \to \tau\tau$ [79,80], $H \to WW$ [81,82], $H \to \gamma\gamma$ [83] and $H \to$ invisible [84,85].

The angular distribution of the two tagging jet carries unambiguous information of the CP properties of the Higgs coupling to the $W^{\pm}$ or Z^0 independently from the decay channel and the mass of the Higgs considered [86]. In the Standard Model (SM) the WWH and ZZH couplings originate from the kinetic energy term of the symmetry breaking field, which provides a coupling that is proportional to the metric tensor $g^{\mu\nu}$; this tensor structure is not gauge invariant by itself and the Higgs boson

---

[1]The plot was made by the Tev4LHC Higgs working group.

[2]As we will see later in this Chapter, at NLO we will use an algorithm to select two jets among the three forward jets.
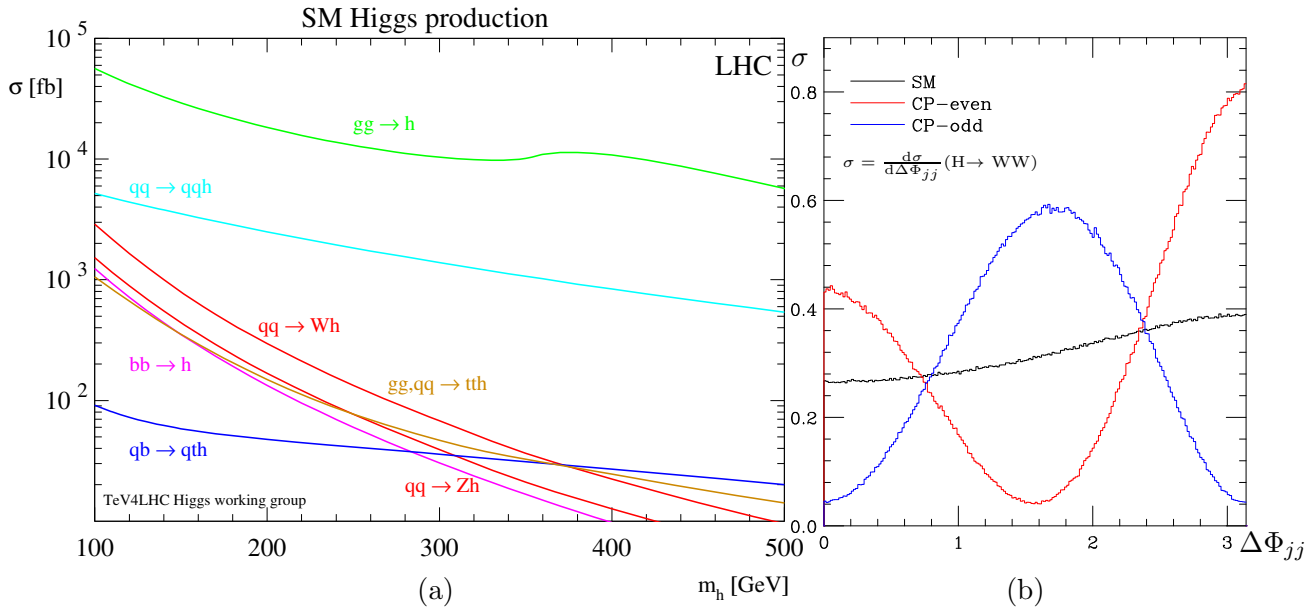
Figure 2.1: Higgs production via vector boson fusion does not have the largest cross section at LHC, as shown in (a), but is very useful in determining the CP nature of the Higgs boson, as shown in (b).

is identified only after the spontaneous symmetry breaking. It thus follows that the azimuthal angle distribution of the two tagging jet is proportional to the invariant mass squared of the two tagging jet; as depicted in Fig.[3] 2.1b, the cross section is essentially flat (SM curve) apart from a slight bias for small angles due to the applied cuts (see Ref. [86]). Higgs couplings to the gauge bosons which arise from loop effects have a completely different tensor structure [86]. As a consequence, the azimuthal angle distribution shows a very different behaviour within an effective field theory with dimension 6 operators, as shown in Fig. 2.1b. The CP odd contribution of the Lagrangian provides a cross section proportional to the Levi-Civita tensor in the coupling, which gives a nonzero result when four independent momenta contribute to the process, while it vanishes in the other cases (CP odd curve), *i.e.* for planar scattering this happens when the two tagging jets are back-to-back or collinear. The CP even contribution provides a cross section that is proportional to the squared scalar product of the two tagging jets transverse momentum (CP even curve). From Fig. 2.1b we conclude that Higgs production via vector boson fusion is expected to play an important rôle in determining the CP nature and the tensor structure of the Higgs coupling.

In order to calculate the SM Higgs boson coupling constants with sufficient accuracy, next-to-leading (NLO) QCD cross corrections for the VBF process must be included. These corrections have been known for some time [87] and are relatively small, with K-factors around 1.05 to 1.1. At next-to-leading order, the theoretical prediction of the Standard Model production cross sections have an error of less than 10%. This accuracy is sufficient to compare predictions with upcoming LHC

---

[3]The normalized distribution was plotted by the Herwig++ collaboration in the case of Higgs mass $m_H = 160$ GeV and Higgs decay $H \rightarrow WW$.

measurements, which will be performed with a statistical accuracy on the product of the production cross section and decay branching ratio reaching 5 to 10% [76,77]. The theoretical uncertainties for the VBF process therefore do not significantly compromise the precision of the coupling constant measurements. This makes the VBF process more attractive than Higgs production via gluon fusion, which has a K-factor larger than 2 and for which the uncertainties remain between $10-20\%$ even after the inclusion of next-to-next-to-leading order corrections [88–96]. Nevertheless, stringent cuts are necessary to distinguish the VBF Higgs boson signal from the backgrounds. In particular, a veto on additional activity in the events, the central-jet veto, is often imposed to reduce the backgrounds.

In this Chapter we discuss the way I implemented the POWHEG method for the Higgs production via VBF in the Herwig++ parton shower [97]. As we will see in the next sections, VBF and DIS have common features so that they can be implemented in the Herwig++ parton shower using a similar approach. However, we prefer to focus on the VBF implementation here and dedicate Chapter 4 to the DIS implementation. The calculation of the VBF leading-order kinematics with NLO accuracy in the POWHEG approach will be discussed in Sect. 2.1. A brief description of the generation of the hardest emission within Herwig++ will be outlined in Sect. 2.2 and in Sect. 2.3 we give details of the implementation of truncated and vetoed showers in the program. Our results will be described in Sect. 2.4. We present our conclusions in Sect. 2.5.

2.1 Calculation of $\bar{B}(\Phi_B)$

The leading-order diagram for the VBF process is shown in Fig. 2.2a, together with appropriate crossings of the quark lines. In principle other contributions to the VBF process should be considered: diagrams with the exchange of identical outgoing quarks and the quark annihilation processes $\bar{q}q \to Z^* \to ZH$ and $\bar{q}q \to W^{\pm*} \to W^{\pm}H$ with hadronic decays of the vector bosons. However, colour suppression and the large momentum transfer in the weak-boson propagators make the contribution from these additional processes negligible in the phase-space regions where VBF can be observed experimentally, *i.e.* with widely separated quark jets of very large invariant mass [98].

At $\mathcal{O}(\alpha_s(\mu_R))$, the contributions coming from amplitudes in which the gluon is attached to both upper and lower quark lines in the VBF process vanish because the weak boson has no colour charge. The only Feynman graphs contributing are therefore the ones shown in Figs. 2.2b-2.2f, where for simplicity we show only radiation from the upper quark line.

The corrections to the DIS and VBF processes are therefore the same provided that we take into account the corrections to both quarks lines in the VBF process. In this section, we show the analytical contributions to the next-to-leading order differential cross section for VBF. Collecting the real emission cross section, described in Sect. 2.1.1, together with the virtual and collinear contributions, briefly discussed in Sect. 2.1.3, $\bar{B}(\Phi_B)$ can be calculated. Particular attention will be paid to the NLO phase-space, Sect. 2.1.2, so that later in this thesis it will be possible to compare the present implementation and the one that I made for the DIS into the
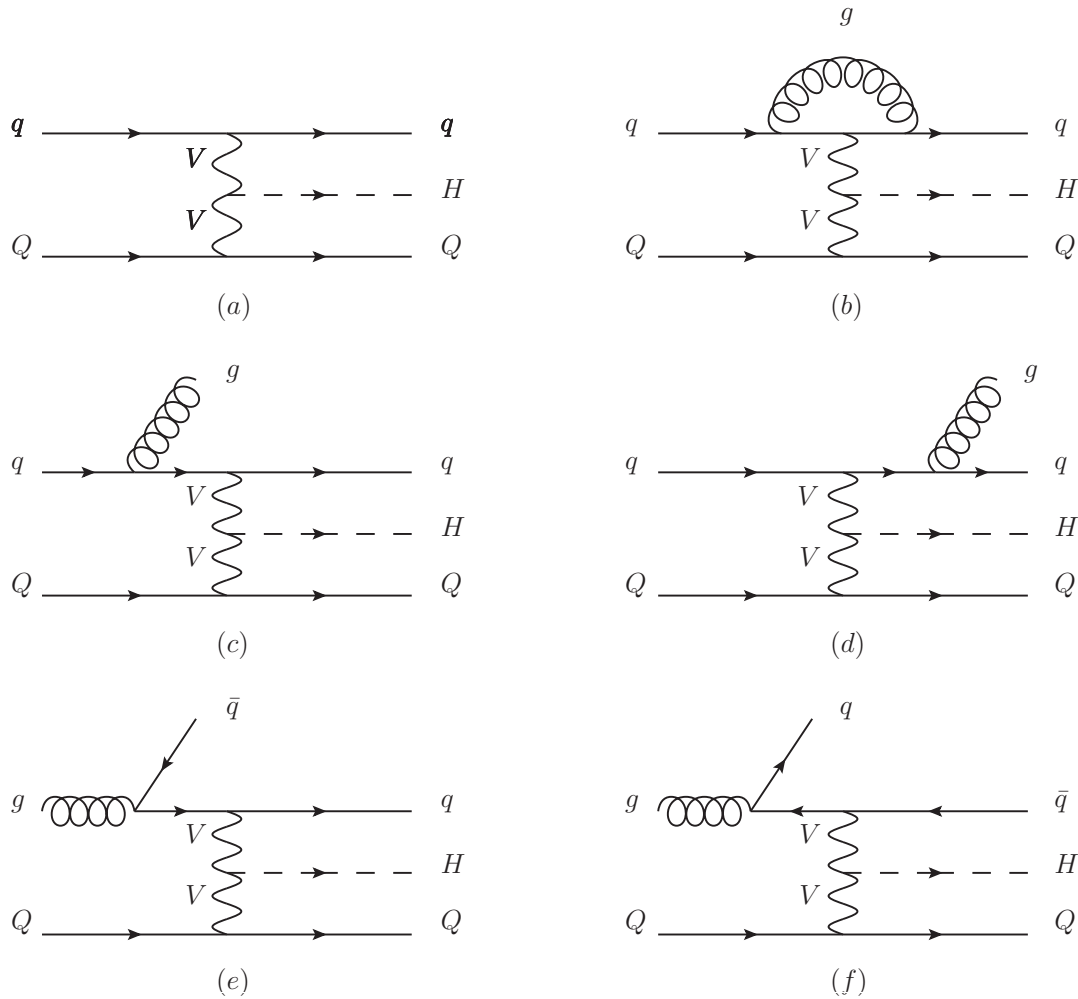
Figure 2.2: Feynman diagrams contributing to Higgs boson production via weak-boson fusion at $\mathcal{O}(\alpha_s(\mu_R))$: leading order (a), virtual (b) and real emission (c-f) corrections. For simplicity, we show only radiative corrections to the upper line in the gluon emission (c-d) and gluon initiated processes (e-f). In this case $V = W^{\pm}$ or Z^0.

dipole shower. We then discuss how $\bar{B}(\Phi_B)$ is sampled within Herwig++ in Sect. 2.1.4.

2.1.1 Real emission contribution

The corrections to e^+e^- annihilation to hadrons can be written in a form in which the QCD and electroweak parts exactly factorize [99]. This method was later generalized to any process in which the lowest-order diagrams contain a single quark line attached to a single electroweak gauge boson [48]. We adopt this approach for the calculation of the real corrections to VBF[4], based on the calculation of the correction to DIS in Refs. [44, 48].

---

[4]In Chapter 4 the same approach will be used for the calculation of the corrections to DIS.
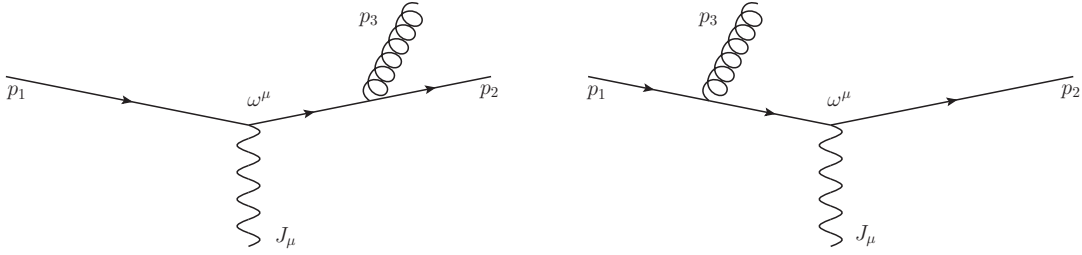
Figure 2.3: QCD Compton scattering, in which a quark interacts with an arbitrary current J_μ via boson-quark coupling ω^μ.

Consider the QCD Compton process, shown in Fig. 2.3, where a quark q with momentum p_1 and a fraction x_B of the incoming hadron momentum, interacts with a current J_μ and boson-parton coupling ω^μ, and scatters into an outgoing quark q' with momentum p_2 and a gluon with momentum p_3

$$\text{QCDC} : q(p_1) + X \rightarrow q'(p_2) + g(p_3) + X'. \tag{2.1}$$

It is simplest to work in the *Breit frame*, in which the incoming parton for the leading-order process has four-momentum $q_1 = \frac{Q}{2}(1; 0, 0, 1)$, the exchanged boson has four-momentum $q = (0; 0, 0, -Q)$ and the scattered quark has four-momentum $q_2 = \frac{Q}{2}(1; 0, 0, -1)$. In this frame the four-momenta of the real emission process are

$$p_1 = \frac{Q}{2}(-x_1; 0, 0, -x_1); \tag{2.2a}$$

$$p_2 = \frac{Q}{2}(\sqrt{x_2^2 + x_\perp^2}; \quad x_\perp \cos\phi, \quad x_\perp \sin\phi, -x_2); \tag{2.2b}$$

$$p_3 = \frac{Q}{2}(\sqrt{x_3^2 + x_\perp^2}; -x_\perp \cos\phi, -x_\perp \sin\phi, -x_3); \tag{2.2c}$$

where the transferred momentum $q = (0; 0, 0, -Q) = p_2 + p_3 - p_1$,

$$x_i = \frac{2p_i \cdot q}{q \cdot q}. \tag{2.3}$$

Momentum conservation requires that $x_3 = 2 + x_1 - x_2$ and

$$x_\perp^2 = \frac{(x_3^2 - x_1^2 - x_2^2)^2}{4x_1^2} - x_2^2. \tag{2.4}$$

In terms of these variables the cross section for the real emission process is

$$d\sigma_{\text{NLO}} = \frac{1}{4(2\pi)^2} \frac{d\phi}{2\pi} \frac{dx_1 dx_2}{-x_1^3} \frac{-x_1 x_B f(-x_1 x_B, Q^2)}{x_B f(x_B, Q^2)} \frac{Q^2 |\mathcal{M}_{\text{QCDC}}|^2}{|\mathcal{M}_{\text{LO}}(q_1, q_2)|^2} d\sigma_2, \tag{2.5}$$

where x_B is the momentum fraction of the quark in the leading-order process, $|\mathcal{M}_{\text{QCDC}}|^2$ and $|\mathcal{M}_{\text{LO}}(q_1, q_2)|^2$ are the spin and colour averaged matrix elements squared for the real emission and leading-order processes respectively.

Using the gauge introduced by the CALKUL collaboration [100], the matrix element for the real emission process is [44, 48]

$$|\mathcal{M}_{\mathrm{QCDC}}|^2 = -\frac{8\pi\alpha_S C_F}{(1+x_1)(1-x_2)Q^2}\left(x_1^2 + (x_2^2 + x_\perp^2)R_2\right)|\mathcal{M}_{\mathrm{LO}}(q_1, q_2)|^2, \qquad (2.6)$$

where

$$R_2 \equiv \frac{x_2^2}{x_2^2 + x_\perp^2}\frac{|\mathcal{M}_{\mathrm{LO}}(\bar{r}_1, r_2)|^2}{|\mathcal{M}_{\mathrm{LO}}(q_1, q_2)|^2}, \qquad (2.7)$$

with $r_2 = \frac{p_2}{x_2}$ and $\bar{r}_1 = r_2 - q$.

The integration of the phase-space is simpler if we use the variables:

$$x_1 = -\frac{1}{x_p}; \qquad (2.8a)$$

$$x_2 = 1 - \frac{1 - z_p}{x_p}; \qquad (2.8b)$$

so that the phase-space limits become $x_B < x_p < 1$ and $0 < z_p < 1$. In terms of these variables

$$x_\perp^2 = \frac{4(1 - x_p)(1 - z_p)z_p}{x_p}. \qquad (2.9)$$

The cross section for the real emission process becomes

$$d\sigma_{\mathrm{NLO}} = \frac{\alpha_S C_F}{2\pi}\frac{d\phi}{2\pi}\frac{\frac{x_B}{x_p}f(\frac{x_B}{x_p}, Q^2)}{x_B f(x_B, Q^2)}\frac{dx_p dz_p}{(1 - x_p)(1 - z_p)}\left(1 + x_p^2(x_2^2 + x_\perp^2)R_2\right)d\sigma_2. \qquad (2.10)$$

This allows us to treat the QCD Compton process as a correction to the leading-order quark scattering process.

The boson-gluon fusion process,

$$\mathrm{BGF}: g(p_1) + X \to q'(p_2) + \bar{q}(p_3) + X', \qquad (2.11)$$

can be treated in a similar way. In this case the spin and colour averaged matrix element squared is

$$|\mathcal{M}_{\mathrm{BGF}}|^2 = \frac{8\pi\alpha_S T_R}{(1-x_2)(1-x_3)Q^2}\left((x_2^2 + x_\perp^2)R_2 + (x_3^2 + x_\perp^2)R_3\right), \qquad (2.12)$$

where

$$R_3 = \frac{x_3^2}{x_3^2 + x_\perp^2}\frac{|\mathcal{M}_{\mathrm{LO}}(r_3, r_3 + q)|^2}{|\mathcal{M}_{\mathrm{LO}}(q_1, q_2)|^2}, \qquad (2.13)$$

with $r_3 = -p_3/x_3$.

Using the same change of variables as before the differential cross section is

$$d\sigma_{\mathrm{LO}} = \frac{T_R\alpha_S}{2\pi}\frac{d\phi}{2\pi}\frac{dx_p dz_p}{z_p(1 - z_p)}\frac{\frac{x_B}{x_p}f\left(\frac{x_B}{x_p}, Q^2\right)}{x_B f(x_B, Q^2)}\left(x_P^2(x_2^2 + x_\perp^2)R_2 + x_P^2(x_3^2 + x_\perp^2)R_3\right). \qquad (2.14)$$

Thus far, our result gives the calculation of the BGF cross section, without any distinction between quark and antiquark scattering. If we want to view Eqn. 2.14 as a correction to a given lowest-order process, partons and antipartons should be treated equivalently. As the $z_p = 1$ singularity is associated with configurations that become collinear to the lowest-order quark scattering process, while the $z_p = 0$ singularity is associated with the antiquark scattering process, we can separate

$$\frac{1}{z_p(1-z_p)} = \frac{1}{z_p} + \frac{1}{1-z_p} \tag{2.15}$$

and rewrite the cross section as

$$d\sigma_{\mathrm{NLO}} = \frac{T_R \alpha_S}{2\pi} \frac{d\phi}{2\pi} \frac{dx_p dz_p}{(1-z_p)} \frac{\frac{x_B}{x_p} f\left(\frac{x_B}{x_p}\right)}{x_B f(x_B)} \left(x_P^2(x_2^2 + x_\perp^2)R_2 + x_P^2(x_3^2 + x_\perp^2)R_3 \right), \tag{2.16}$$

with the corresponding $\frac{1}{z_p}$ term giving a correction to the antiquark scattering process [44, 48].

Using these results we can rewrite the real emission corrections as

$$d\sigma_R \equiv R(\Phi_B, \Phi_R)d\Phi_B d\Phi_R, \tag{2.17}$$

where

$$R(\Phi_B, \Phi_R) = \sum_{I \in \{\mathrm{QCDC, BGF}\}} R_I = B(\Phi_B) \sum_{I \in \{\mathrm{QCDC, BGF}\}} \frac{\mathcal{C}_I \alpha_s(\mu_R)}{2\pi} \mathcal{A}_I, \tag{2.18}$$

with

$$\mathcal{C}_{\mathrm{QCDC}} = C_F, \tag{2.19a}$$

$$\mathcal{C}_{\mathrm{BGF}} = T_R, \tag{2.19b}$$

$$\mathcal{A}_{\mathrm{QCDC}} = \frac{\frac{x_B}{x_p} f_q\left(\frac{x_B}{x_p}, Q^2\right)}{x_B f_q(x_B, Q^2)} \frac{1}{(1-x_p)(1-z_p)} \left(1 + x_p^2(x_p^2 + x_\perp^2))R_2 \right), \tag{2.19c}$$

$$\mathcal{A}_{\mathrm{BGF}} = \frac{\frac{x_B}{x_p} f_g\left(\frac{x_B}{x_p}, Q^2\right)}{x_B f_q(x_B, Q^2)} \frac{1}{(1-z_p)} \left(x_P^2(x_2^2 + x_\perp^2)R_2 + x_P^2(x_3^2 + x_\perp^2)R_3 \right). \tag{2.19d}$$

The radiative phase-space element is

$$d\Phi_R = \frac{1}{2\pi} dx_p dz_p d\phi. \tag{2.20}$$

The singularities in $R(\Phi_B, \Phi_R)$ are cancelled by subtracting

$$D_I = \frac{\mathcal{C}_I \alpha_s(\mu_R)}{2\pi} \mathcal{D}_I, \tag{2.21}$$

where $\mathcal{D}_I$ are the Catani-Seymour dipoles [36]:

$$\mathcal{D}_{\mathrm{QCDC}} = \frac{\frac{x_B}{x_p} f_g\left(\frac{x_B}{x_p}, Q^2\right)}{x_B f_q(x_B, Q^2)} \frac{x_p^2 + z_p^2}{(1-x_p)(1-z_p)}; \tag{2.22a}$$

$$\mathcal{D}_{\mathrm{BGF}} = \frac{\frac{x_B}{x_p} f_g\left(\frac{x_B}{x_p}, Q^2\right)}{x_B f_q(x_B, Q^2)} \frac{x_p^2 + (1-x_p)^2}{1-z_p}. \tag{2.22b}$$

The contribution of the real emission processes to $\bar{B}$ is therefore

$$B(\Phi_B)d\Phi_B \sum_{I \in \{\mathrm{QCDC, BGF}\}} \frac{\mathcal{C}_I \alpha_s(\mu_R)}{2\pi} \left(\mathcal{A}_I - \mathcal{D}_I \right) d\Phi_R. \tag{2.23}$$

33

2.1.2 NLO phase-space

The NLO phase-space measure is

$$d\Phi_{NLO}^{(5)} = d\Phi_R d\Phi_l, \tag{2.24}$$

where $d\Phi_R$ describes the hadronic contribution and is given by Eqn. 3.7, $d\Phi_l$ describes the leptonic contribution, which is the one generated at LO, and provides the remaining two degrees of freedom. The method by which we generate the momenta at NLO is as follows:

- generate momenta at LO in the centre of mass frame;

- boost LO momenta into the Breit frame;

- calculate Q^2;

- generate the radiative variables[5]: $\{x_p, z_p, \phi\}$ or equivalently $\{x_1, x_2, \phi\}$;

- calculate the NLO momenta defined in Eqns. 2.2a-2.2c by using Q^2 and the radiative variables;

- boost NLO momenta into the centre of mass frame.

From the previous algorithm we see that the NLO phase-space depends on the LO momenta and that the transferred momentum, Q^2, is not a degree of freedom of the NLO phase-space measure.

2.1.3 Virtual contribution and collinear remainders

The finite piece of the virtual correction is given by [98]

$$d\sigma_V = \frac{C_F \alpha_s(\mu_R)}{2\pi} V(x_B) B(\Phi_B), \tag{2.25}$$

where the finite contribution of $\mathbf{I}(\epsilon)$ [36] and the virtual correction are

$$V(x_B) = -\frac{\pi^2}{3} - \frac{9}{2} + \frac{3}{2} \ln \frac{Q^2}{\mu_F^2(1 - x_B)} + 2 \ln(1 - x_B) \ln \frac{Q^2}{\mu_F^2} + \ln^2(1 - x_B). \tag{2.26}$$

The collinear remainders are

$$d\sigma_{\text{coll}} = \frac{C_F \alpha_s(\mu_R)}{2\pi} \frac{f^m(x_B, \mu_F)}{f(x_B, \mu_F)} B(\Phi_B), \tag{2.27}$$

---

[5]The radiative phase-space is defined in Eqn. 3.7. As we will discuss in Sect. 2.1.4, for convenience we transform $\{x_p, z_p, \phi\}$ to $\{\tilde{x}_p, z_p, \tilde{\phi}\}$, defined on the interval $[0, 1]$.

where the modified PDF is[6]

$$f_q^m(x_B, \mu_F) = \int_{x_B}^1 \frac{\mathrm{d}x_p}{x_p} \left\{ f_g\left(\frac{x_B}{x_p}, \mu_F\right) A(x_p) \right.$$
$$+ \left[f_q\left(\frac{x_B}{x_p}, \mu_F\right) - x_p f_q(x_B, \mu_F) \right] B(x_p)$$
$$\left. + f_q\left(\frac{x_B}{x_p}, \mu_F\right) C(x_p) \right\}, \tag{2.28}$$

where f_q and f_g are the quark and gluon PDFs respectively, and

$$A(x_p) = \frac{T_F}{C_F} \left[x_p^2 + (1-x_p)^2 \right] \ln\frac{Q^2(1-x_p)}{\mu_F^2 x_p} + 2\frac{T_F}{C_F} x_p(1-x_p), \tag{2.29}$$

$$B(x_p) = \left[\frac{2}{1-x_p}\ln\frac{Q^2(1-x_p)}{\mu_F^2} - \frac{3}{2}\frac{1}{1-x_p} \right], \tag{2.30}$$

$$C(x_p) = \left[1 - x_p - \frac{2}{1-x_p}\ln x_p - (1+x_p)\ln\frac{Q^2(1-x_p)}{\mu_F^2 x_p} \right]. \tag{2.31}$$

The combined contribution of the finite virtual term and collinear remnants is

$$\mathrm{d}\sigma_{V+\mathrm{coll}} = \frac{C_F \alpha_s(\mu_R)}{2\pi}\mathcal{V}(\Phi_B)B(\Phi_B), \tag{2.32}$$

with

$$\mathcal{V}(\Phi_B) \equiv V(x_B) + \tilde{V}(x_B, \mu_F)., \tag{2.33}$$

where $\tilde{V}(x_B, \mu_F) = \frac{f^m(x_B, \mu_F)}{f(x_B, \mu_F)}$.

2.1.4 Sampling $\bar{B}$ within Herwig++

Using the results in the previous sections

$$\bar{B}(\Phi_B) = B(\Phi_B)\left[1 + \frac{C_F\alpha_s(\mu_R)}{2\pi}\mathcal{V}(\Phi_B) \right.$$
$$\left. + \sum_{I\in\{\mathrm{QCDC,BGF}\}} \frac{\mathcal{C}_I\alpha_s(\mu_R)}{2\pi} \int \left[\mathcal{A}_I(\Phi_B, \Phi_R) - \mathcal{D}_I(\Phi_B, \Phi_R) \right]\mathrm{d}\Phi_R \right]. \tag{2.34}$$

For convenience, the radiative variables $\{x_p, z_p, \phi\}$ are transformed into a new set $\left\{\tilde{x}_p, z_p, \tilde{\phi}\right\}$, defined on the interval $[0, 1]$, such that the radiative phase-space is a unit cube. The variable x_p is redefined as

$$x_p = 1 - \rho^{\frac{1}{1-n}}, \tag{2.35}$$

where n is fixed, and ρ is the new variable with phase-space limits

$$0 < \rho < (1-x_B)^{1-n}. \tag{2.36}$$

---

[6]We write the modified PDF for the quark q, but a similar expression is valid for an incoming antiquark $\bar{q}$.

This change of variable has been made in order to guarantee numerical stability when calculating the integral of $1/(1 - x_p)$. A further transformation is needed to achieve $\tilde{x}_p$:

$$\rho = (1 - x_B)^{1-n}\tilde{x}_p. \tag{2.37}$$

Finally, the variable ϕ is easily redefined as $\tilde{\phi} = \frac{\phi}{2\pi}$.

The sampling of $\bar{B}(\Phi_B)$ proceeds in the following way:

1. generate a leading-order configuration using the standard Herwig++ leading-order matrix element generator, providing the Born variables Φ_B with an associated weight $B(\Phi_B)$;

2. radiative variables Φ_R are then generated by sampling $\bar{B}(\Phi_B)$, parametrised in terms of the unit cube $(\tilde{x}_p, z_p, \tilde{\phi})$, using the Auto-Compensating Divide-and-Conquer (ACDC) phase-space generator [101];

3. the leading-order configuration is accepted with a probability proportional to the integrand of Eqn. 2.34 evaluated at $\{\Phi_B, \Phi_R\}$.

In order to treat radiation from both quark lines in the VBF and DIS processes we randomly select one line that emits the radiation and generate events in $\Phi\left\{\tilde{x}_p, z_p, \tilde{\phi}\right\}$. The symmetry of the process then ensures that the correct statistical result is obtained by multiplying the correction term in Eqn. 2.34 by two.

2.2 The generation of the hardest emission

The hardest emission is generated using the modified Sudakov form factor, given by the product of $\Delta_R(p_T)$ for each channel contributing; this is done by replacing the ratio $R(\Phi_B, \Phi_R)/B(\Phi_B)$ in Eqn. 1.81 with

$$W_I(\Phi_B, \Phi_R) = \frac{R_I(\Phi_B, \Phi_R)}{B(\Phi_B)}. \tag{2.38}$$

Moreover, we prefer to generate the hardest emission in terms of radiative variables $\Phi'_R(x_\perp, z_p, \tilde{\phi})$ so that the θ-function in Eqn. 1.81 simply gives $x_\perp$ as the upper limit of the integral and the modified Sudakov form factor, for the channel I, becomes

$$\Delta_{R_I}(x_\perp) = \exp\left(-\int_{x_\perp}^{x_\perp^{\max}} \frac{\mathrm{d}x'_\perp}{x'^3_\perp} \mathrm{d}\tilde{\phi}\mathrm{d}z_p \frac{C_I\alpha_S}{2\pi} 8z_p(1 - z_p)(1 - x_p)^2 \mathcal{A}_I\right), \tag{2.39}$$

where $\frac{Q}{2}x_\perp^{\max}$ is the maximum value for the transverse momentum.

The radiative variables are generated using the *veto algorithm*, described in [26]. We use the upper bounding function

$$g_I = \frac{a_I}{x^3_\perp}, \tag{2.40}$$

for the integrand, which is chosen such that g_I can be easily integrated in $\{x_\perp, x_\perp^{\max}\}$. The generation procedure then proceeds as follows:

1. $x_\perp$ is set to $x_\perp^{\max}$;

2. a new $(\tilde{x}_p, z_p, \tilde{\phi})$ is randomly generated according to

$$\Delta_{R_I}^{\text{over}}(x_\perp) = \exp\left(-\int_{x_\perp}^{x_\perp^{\max}} \frac{\mathrm{d}x'_\perp}{x'^3_\perp}\mathrm{d}\tilde{\phi}\mathrm{d}z_p a_I\right), \qquad (2.41)$$

giving[7]

$$x_\perp^2 = \frac{1}{\frac{1}{(x_\perp^{max})^2} - \frac{2}{a_I}\ln\mathcal{R}_1}, \qquad (2.42)$$

$$z_p = \mathcal{R}_2, \qquad (2.43)$$

$$\tilde{\phi} = \mathcal{R}_3. \qquad (2.44)$$

3. if $\tilde{x}_p < 0$ or $\tilde{x}_p > 1$, the configuration generated is outside the phase-space boundaries, then return to step 1;

4. if

$$\frac{1}{g_I}\frac{C_I\alpha_S}{2\pi}8z_p(1-z_p)(1-x_p)^2\mathcal{A}_I > \mathcal{R}, \qquad (2.45)$$

the configuration is accepted, otherwise return to step 1.

2.3 Truncated and vetoed parton showers

The Herwig++ shower algorithm [3,35] starts at an initial scale, given by the kinematics and the colour structure of the hard scattering process, and evolves down in the evolution variable related to the angular separation of parton branching products, $\tilde{q}$. The evolution is generated by the emission of partons in $1 \rightarrow 2$ branching processes and each branching is described by a scale, $\tilde{q}$, a light-cone momentum fraction, z, and an azimuthal angle, ϕ. The latter parameters are used to uniquely define the momenta of all particles radiated in a shower. However, the Herwig++ approach generally requires some reshuffling of these momenta after the generation of the parton showers to ensure global energy-momentum conservation.

$(N+1)$-body final states associated with the generation of the hardest emission are first interpreted as a standard Herwig++ emission, from the N-body configuration, specified by the branching variables $(\tilde{q}_h, z_h, \phi_h)$. The POWHEG emission is performed as a single Herwig++ shower as follows:

1. the truncated shower evolves from the default starting scale to $\tilde{q}_h$, such that any further emission conserves the flavour of the emitting parton and has transverse momentum lower than that of the hardest emission;

2. the hardest emission is forced with shower variables $(\tilde{q}_h, z_h, \phi_h)$;

3. the vetoed shower evolves down to the hadronization scale, vetoing any emission with transverse momentum higher than that of the hardest emission.

---

[7]Here $\mathcal{R}_i$ defines a random number in $[0, 1]$.

The key feature of this approach is the ability to interpret the hard emission in terms of the shower variables. In order to do this we first need to consider the treatment of processes with an initial-state final-state colour connection, such as DIS or VBF, in the Herwig++ parton shower. In these processes the momenta of the incoming and outgoing colour connected partons after the parton shower are first reconstructed from the shower variables as described in Ref. [3]. These off-shell momenta are such that energy and momentum is not conserved, so boosts are applied to the incoming and outgoing momenta such that the momentum of the virtual boson is preserved by the showering process. In DIS and VBF type processes the reconstructed momenta are boosted to the Breit-frame of the system before the radiation. We take p_b to be the momentum of the original incoming parton and p_c to be the momentum of the original outgoing parton and $p_a = p_c - p_b$, therefore in the Breit-frame

$$p_a = Q(1; 0, 0, -1). \tag{2.46}$$

We can then construct a set of basis vectors,

$$n_1 = Q(1; 0, 0, 1), \qquad\qquad n_2 = Q(1; 0, 0. -1). \tag{2.47}$$

The momenta of the off-shell incoming parton can be decomposed as

$$q_{\text{in}} = \alpha_{\text{in}} n_1 + \beta_{\text{in}} n_2 + q_\perp, \tag{2.48}$$

where $\alpha_{\text{in}} = \frac{n_2 \cdot q_{\text{in}}}{n_1 \cdot n_2}$, $\beta_{\text{in}} = \frac{n_1 \cdot q_{\text{in}}}{n_1 \cdot n_2}$ and $q_\perp = q_{\text{in}} - \alpha_{\text{in}} n_1 - \beta_{\text{in}} n_2$. In order to reconstruct the final-state momentum we first apply a rotation so that the momentum of the outgoing jet is

$$q_{\text{out}} = \alpha_{\text{out}} n_1 + \beta_{\text{out}} n_2 + q_\perp, \tag{2.49}$$

where β_{out} is taken to be one and the requirement that the virtual mass is preserved gives $\alpha_{\text{out}} = \frac{q_{\text{out}}^2 + p_\perp^2}{2 n_1 \cdot n_2}$, where $q_\perp^2 = -p_\perp^2$. The momenta of the jets are rescaled such that

$$q'_{\text{in,out}} = \alpha_{\text{in,out}} k_{\text{in,out}} n_1 + \frac{\beta_{\text{in,out}}}{k_{\text{in,out}}} n_2 + q_\perp, \tag{2.50}$$

which ensures that the virtual mass of the partons is preserved. The requirement that the momentum of the system is conserved, *i.e.*

$$p_a = q'_{\text{out}} - q'_{\text{in}} = Q(0, 0, -1; 0), \tag{2.51}$$

gives

$$\alpha_{\text{in}} k_{\text{in}} - \alpha_{\text{out}} k_{\text{out}} = \frac{1}{2}, \tag{2.52a}$$

$$\frac{\beta_{\text{in}}}{k_{\text{in}}} - \frac{\beta_{\text{out}}}{k_{\text{out}}} = -\frac{1}{2}. \tag{2.52b}$$

Once the rescalings have been determined the jets are transformed using a boost such that

$$q_{\text{in,out}} \overset{\text{boost}}{\longrightarrow} q'_{\text{in,out}}. \tag{2.53}$$

In order to interpret the hard emission in terms of the shower variables we first calculate the momentum of the off-shell incoming, $q_b'^{\text{new}}$, or outgoing, $q_c'^{\text{new}}$, parton

depending on whether we are dealing with initial- or final-state radiation. We then compute the boost into the Breit-frame of this system and construct the basis vectors $n_{1,2}$ as before, which allows us to determine the transverse momentum, $q_\perp$, of the off-shell incoming parton. In this frame the momenta of the partons before the shower would be:

$$p_b = \frac{Q}{2}(1+c; 0, 0, 1+c); \qquad p_c = \frac{Q}{2}(1+c; 0, 0, -(1-c)). \qquad (2.54)$$

The momenta of the off-shell partons before the boost required to conserve energy and momentum are

$$q_b^{\text{new}} = \alpha_{\text{in}}^{\text{new}} n_1 + \beta_{\text{in}}^{\text{new}} n_2 + q_\perp \qquad q_c^{\text{new}} = \alpha_{\text{out}}^{\text{new}} n_1 + \beta_{\text{out}}^{\text{new}} n_2, \qquad (2.55a)$$

where

$$\alpha_{\text{in}}^{\text{new}} = \frac{p_b \cdot n_2}{n_1 \cdot n_2}, \qquad\qquad \beta_{\text{in}}^{\text{new}} = \frac{q_b'^2 - q_\perp^2}{2 n_1 \cdot n_2 \alpha_{\text{in}}^{\text{new}}}, \qquad (2.56a)$$

$$\alpha_{\text{out}}^{\text{new}} = \frac{q_c'^2}{2 n_1 \cdot n_2 \beta_{\text{out}}^{\text{new}}}, \qquad\qquad \beta_{\text{out}}^{\text{new}} = \frac{p_c \cdot n_1}{n_1 \cdot n_2}. \qquad (2.56b)$$

The inverse of the boost, which would be applied in the shower to ensure energy-momentum conservation, can then be determined and applied to all the incoming and outgoing partons. These momenta can be decomposed in terms of the Sudakov basis used in Herwig++, allowing the shower variables $(\tilde{q}_h, z_h, \phi_h)$ to be determined.

2.4 Results

The typical feature of the VBF process at hadron colliders is the presence of two forward tagging jets. At leading-order, they correspond to the two scattered quarks in the hard process and their observation, together with the properties of the Higgs boson decay product, is vital for the suppression of backgrounds [79–85]. Tagging jet distributions must be known precisely in order to gain a good estimate of the Higgs couplings: comparison of the Higgs production rate with tagging jets cross section, within cuts, determine Higgs boson couplings [76, 77] and the uncertainty of measured couplings are determined by the theoretical error of the cross section. At next-to-leading order, tagging jet distributions is enough to estimate size and uncertainties of the higher order QCD corrections, because the Higgs boson does not induce spin correlations in the phase-space of its decay products.

A detailed analysis of jet distributions has been realized in the present work and the results are shown in this section. A preliminary step has been the validation of the $\bar{B}$ function, by comparing the NLO differential cross section as function of the rapidity and the transverse momentum for the stable Higgs boson given by Herwig++ and VBFNLO, as shown in Fig. 2.4 and Fig. 2.5 respectively. The rapidity distribution is symmetric about zero, as expected in a proton-proton collision. In both cases we find excellent agreement between the two distributions and this demonstrates that the generation of radiative variables and the calculation of $\bar{B}$ is correct.
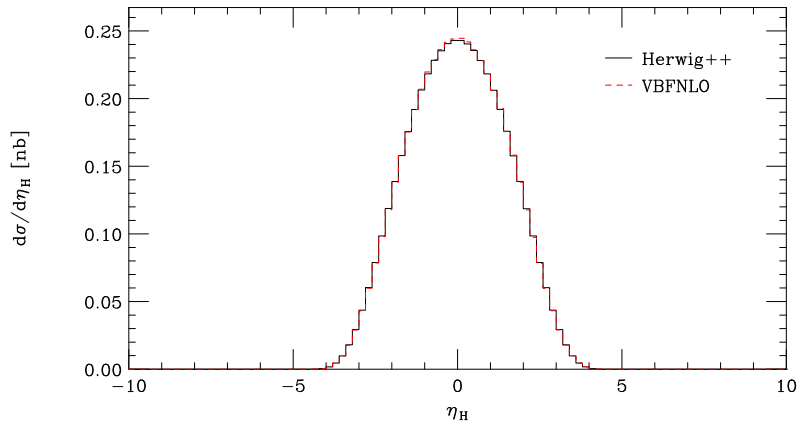
Figure 2.4: Rapidity of the Higgs boson at NLO. The result from Herwig++ (solid black line) is compared to that from VBFNLO (dashed red line).
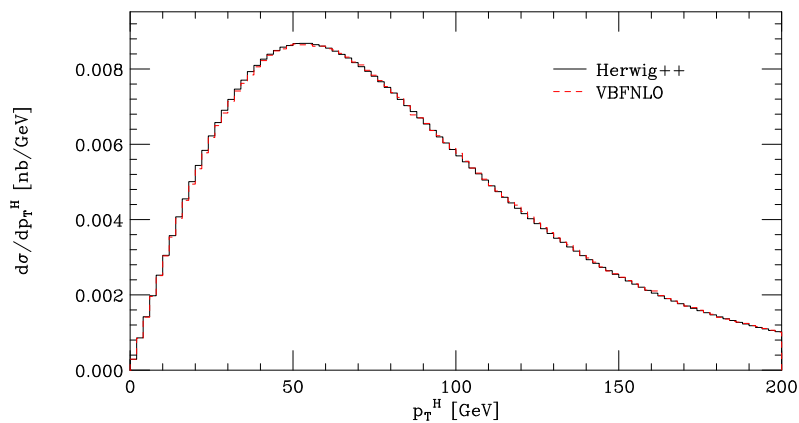
Figure 2.5: Transvere momentum of the Higgs boson at NLO. The results from Herwig++ (solid black line) are compared to those from VBFNLO (dashed red line).

However, at next-to-leading order we can either encounter two jets, with one of them composed of two partons (recombination effects), or 2 jets + 1 parton which does not qualify as jet, or three jets corresponding to well-separated partons. For LHC data, an algorithm to select two tagging jets is needed. There are two possibilities [98]:

1. p_T-*method*: the two tagging jets are the two highest p_T jets in the event;

2. *E-method*: the two tagging jets are the two highest energy jets in the event;

We follow the p_T-method and jets are defined according to the k_T algorithm by using the FASTJET package [102]. As mentioned before, cuts are needed to reduce the effect of backgrounds and we provide two sets of results by choosing two different sets of cuts.

At first, it has been of interest to compare results with the ones from Nason's implementation that has recently appeared in the literature [103]. To this end, we follow the cuts in Ref. [103]. Transverse momentum, p_T^j, and rapidity, y_j, of tagging jets are chosen so that:

$$p_T^j \geq 30 \text{ GeV}, \qquad |y_j| \leq 5. \tag{2.57}$$

Moreover, we require the tagging jets to lie in opposite hemispheres and have a large invariant mass, *i.e.*,

$$y_{j_1} \cdot y_{j_2} < 0, \qquad m_{jj} > 600 \text{ GeV}. \tag{2.58}$$

We set the Higgs boson stable and choose a mass $m_H = 120$ GeV. The factorization and renormalization scales are chosen to be equal to the mass of the Higgs boson. The other relevant electroweak parameters are

$$M_W = 79.964 \text{GeV}, \quad \text{M}_Z = 91.188 \text{GeV}, \tag{2.59}$$

$$\alpha_{\text{em}}(M_Z)^{-1} = 128.930, \quad \sin^2\theta_W = 0.23102, \tag{2.60}$$

and the weak coupling is computed as $g = \sqrt{4\alpha_{\text{em}}/\sin\theta_W}$. The parton distribution functions are chosen to be the CTEQ6M set [104].

The resuts of the POWHEG implementation in the Herwig++ parton shower are shown in Fig. 2.6 and corresponding results from Ref. [103] in Fig. 2.7. In Fig. 2.6a we show the result for the rapidity separation, $|y_{j_1} - y_{j_2}|$, of the two tagging jets. In addition to the shower at LO (red dashed line), we have included the Herwig++ result with POWHEG correction (solid black line) and matrix element correction based on the approach of Ref. [44] (dotted blue line). The distributions are centred around 5.5. POWHEG corrections provide a distribution that is 5% higher with respect to the matrix element correction based on the approach of Ref. [44] and 9% smaller than the one expected from Ref. [103] (see Fig. 2.7a) at the peak of the curve. In Fig. 2.7a POWHEG BOX [105] is interfaced with HERWIG and PYTHIA parton showers, solid black and dashed red line respectevly. The NLO cross section is given by the dotted blue curve and it is almost indistinguishable fom the showers simulation. Here the black dotted line marks the value $|y_{j1} - y_{j2}| = 4.2$: this is the position of the cut on rapidity difference that will be applied in the following.
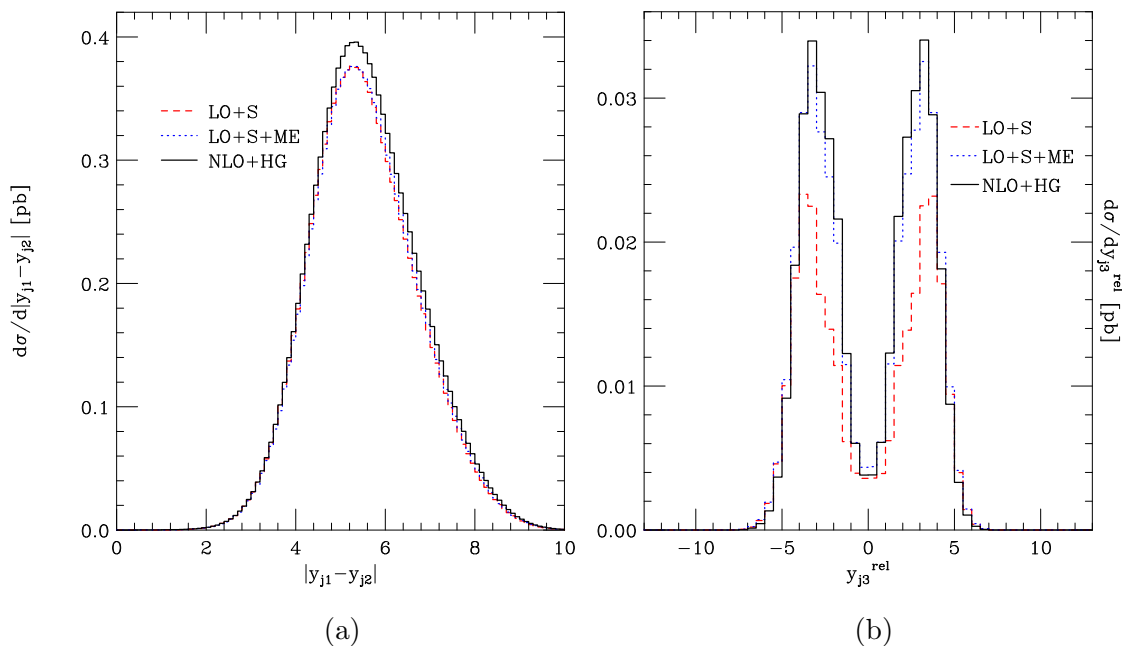
Figure 2.6: The rapidity separation of the two tagging jets (a) and relative rapidity of the third jet (b). The results from Herwig++ within the POWHEG formalism (solid black line) are compared with the shower at LO (red dashed line) and LO shower with matrix element correction based on the approach of Ref. [44] (dotted blue line).
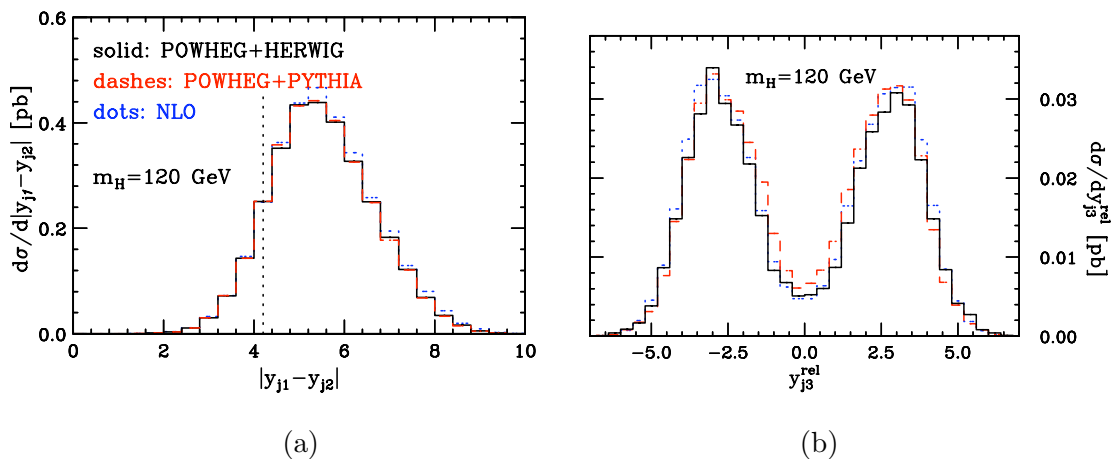
Figure 2.7: The rapidity separation of the two tagging jets (a) and relative rapidity of the third jet (b). Here we show results from Ref. [103]. POWHEG BOX is interface with HERWIG (solid black line) and PYTHIA (red dashed line) parton shower. The NLO cross section is given by the blue dotted curve. The black dotted line marks the cut on rapidity difference that will be used in the following.

In addition, we fix a rapidity separation cut, $|y_{j_1} - y_{j_2}| > 4.2$, and study distributions of the third (hardest) jet. Of relevant interest is the relative rapidity of the third jet with respect to the average of the rapidities of the two tagging jets,

$$y_{j_3}^{\text{rel}} = y_{j_3} - (y_{j_1} + y_{j_2})/2, \tag{2.61}$$

that we plot in Fig. 2.6b. We compare distributions from the Herwig++ parton shower without matrix element correction (red dashed line) and with corrections provided by the POWHEG formalism (solid black line) and the approach of Ref. [44]. We estimate an increasement of 29.4% at the peak of the distribution due to the POWHEG formalism. Fig.2.6b describes the result expected from Ref. [103] (see Fig. 2.7b) reasonably well: the $|y_{j_3}^{\text{rel}}|$-distribution is centred at 3.5 and has peak of 0.034 pb, as expected. In Fig. 2.7b the POWHEG BOX implementation of HERWIG (solid black line) and PYTHIA (red dashed line) is shown. Here again we notice that the NLO cross section distribution (blue dotted line) shows only a little difference from the curves describing the showers. However, a slight asymmetry is visible at the peaks of the distributions and this does not help in determining the exact high of the peaks. The curve in Fig. 2.6b is very symmetric with respect to the origin, as expected in a proton-proton collision.

The second set of result follows the cuts introduced in Ref. [98]. We choose

$$p_T^j \geq 20 \text{ GeV}, \qquad |y_j| \leq 4.5. \tag{2.62}$$

Moreover, we generate the Higgs boson decay in $\tau^+\tau^-$ isotropically and require that the produced leptons have transverse momentum, $p_{T_{\tau(+,-)}}$, and pseudorapidity, $\eta_{\tau(+,-)}$, so that

$$p_{T_{\tau(+,-)}} \geq 20 \text{ GeV}, \qquad |\eta_{\tau(+,-)}| \leq 2.5. \tag{2.63}$$

In addition, we require that jet-lepton separation in the rapidity-azimuthal angle plane satisfies

$$\Delta R_{j\tau(+,-)} \geq 0.6, \tag{2.64}$$

and that the taus fall between the two tagging jets in rapidity

$$y_{j,\min} < \eta_{\tau(+,-)} < y_{j,\min}. \tag{2.65}$$

Backgrounds to VBF are significantly suppressed if the rapidity of the two tagging jets are well separated; therefore, we require

$$|y_{j_1} - y_{j_2}| > 4. \tag{2.66}$$

The factorization and the renormalization scale are chosen to be equal to the mass of the Higgs boson, $m_H = 120$ GeV. The other relevant electroweak parameters are

$$M_W = 80.3980\text{GeV}, \quad M_Z = 91.1876\text{GeV}, \tag{2.67}$$

$$\alpha_{em} = 0.007556, \quad \sin^2\theta_W = 0.222646, \tag{2.68}$$

and the weak coupling is computed as $g = \sqrt{4\alpha_{em}/\sin\theta_W}$. The parton distribution functions are chosen to be the CTEQ6M set [104].
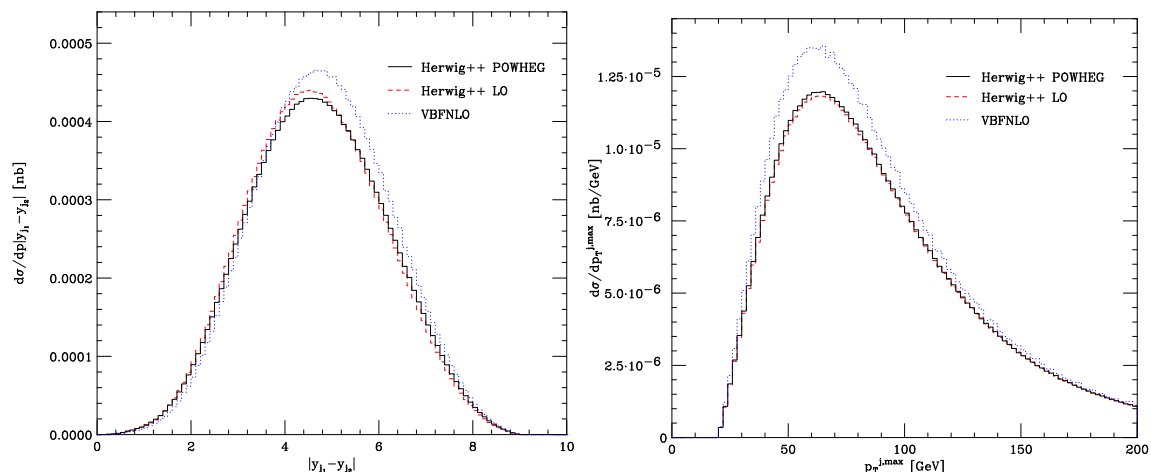
Figure 2.8: Difference of rapidity (left panel) and higher p_T (right panel) distribution of the two tagging jets. In the left panel we have excluded the cut in Eqn. 2.66.

The analysis provides a comparison of distributions for POWHEG implementation (solid black curve) and LO simulation (dashed red curve) of Herwig++ parton shower together with VBFNLO NLO differential cross section (dotted blue curve).

In Fig. 2.8 we present the differential cross section as a function of rapidity separation and higher p_T of the two tagging jets. In the left panel we have excluded the cut in Eqn. 2.66. The cross sections show a peak around 5 in the left panel and 70 GeV in the right panel. The POWHEG implementation leaves unchanged the higher p_T cross section, while it modifies the difference of rapidity distribution with respect to the LO simulation of the Herwig++ parton shower: the curve is 2.3% lower at the peak and slightly shifted to a higher value of the rapidity difference.

In Fig. 2.9 we plot the cross sections of smaller transverse momentum (left panel) and rapidity (right panel) of the two tagging jets. The transverse momentum distribution shows a peak around 30 GeV and the rapidity around 2. The Herwig++ shower provides a similar description at LO and NLO accuracy.

The transverse momentum and rapidity distributions of the third jet are plotted in Fig. 2.10 in the left and right panel respectively. As expected here we see a harder spectrum for the third jet in the POWHEG approach, which is now simulated using the real emission matrix element rather than the shower approximation. The POWHEG curve is 3% lower at the peak for the transverse momentum and 6.4% higher at the peak for the rapidity distribution with respect to the LO simulation of Herwig++.

In this second set of plots we see that the Herwig++ results lie below the fixed NLO results for distributions involving the two leading jets as a result of the subsequent parton shower, unlike the results of Ref. [103] where there is little difference between the POWHEG and fixed order results. This difference exists at both leading order and in the POWHEG approach in Herwig++ and is a result of the different shower algorithm and kinematic reconstruction in Herwig++. A similar behaviour was pointed out in the previous set of plots, where we found that the rapidity dif-
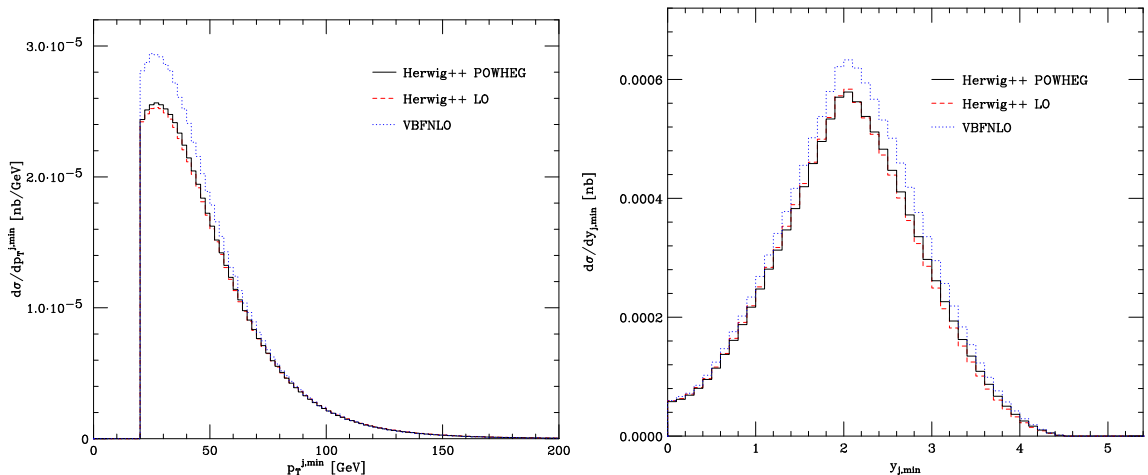
Figure 2.9: Distributions of smaller transverse momentum, $p_T^{j,\min}$, (left panel) and smaller rapidity, $y_{j,\min}$, (right panel) of the two tagging jets.

ference distribution is smaller with respect to the curve of Ref. [103] at the peak. Given the excellent description of the related DIS data compared with the previous HERWIG shower algorithm (see Chapter 4), this is an important difference in the two approaches and worthy of further study.

2.5 Conclusions

In this Chapter the POWHEG NLO matching scheme has been implemented in the Herwig++ Monte Carlo event generator for Higgs production via vector-boson fusion. The $\bar{B}$ function has been calculated following the general approach provided in [48]. The simulation contains a full treatment of the truncated shower, which is needed for the production of wide angle, soft radiation in angular-ordered parton showers.

The implementation of $\bar{B}$ has been checked by comparing results between Herwig++ and VBFNLO. The excellent agreement between the distributions shows that the generator of radiative variables and the calculation of $\bar{B}$ is correct.

We have shown different jet distributions after imposing typical cuts, which are required to remove the effects of backgrounds. With the first set of results we have compared the implementation of POWHEG formalism with the matrix element correction obtained with the approach of Ref. [44] on one side, and on the other with the LO Herwig++ parton shower. The distributions describe reasonably well the results expected from a work that has recently appeared in the literature [103] even though the difference of rapidity shows a normalization that is different than the one expected. The relative rapidity of the third jet shows an excellent symmetry about zero, as expected in a proton-proton collision.

In the second set of results we find that the POWHEG implementation does improve the rapidity difference distribution for the two tagging jets and of p_T and rapidity for the third hardest jet, while it mainly leaves the other distributions
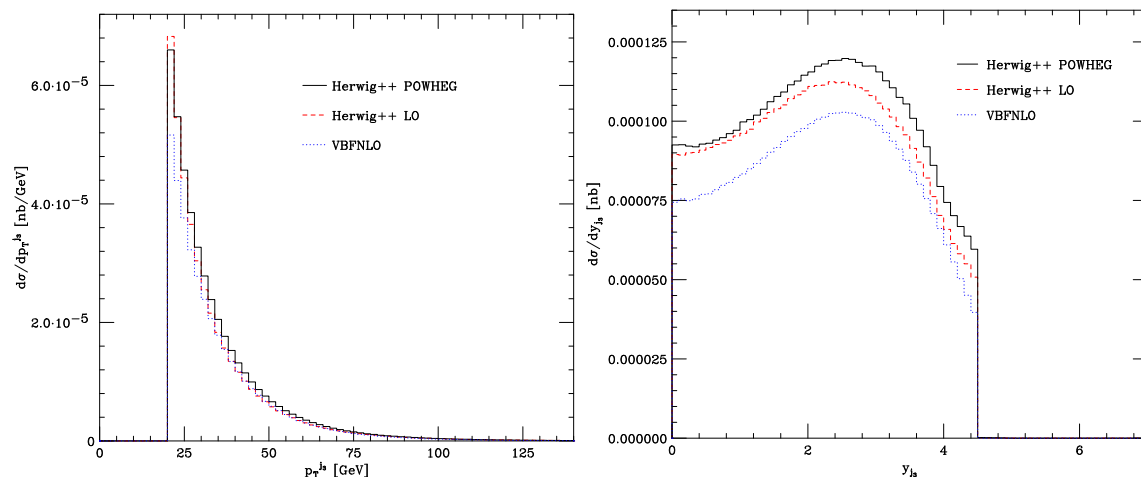
Figure 2.10: Transverse momentum distribution of the third jet ($p_T^{j_3}$) is plotted in the left panel and the rapidity distribution of the same jet (y_{j_3}) in the right one.

of the two tagging jets unchanged with respect to the LO simulations within the Herwig++ parton shower. The difference between the Herwig++ results and the VBFNLO curves is not expected and is worthy for further study.

The lack of data prevents us from comparing the jet distributions with experimental results. However, the present work, together with the Higgs production via gluon fusion and the Higgs-strahlung simulations, which were already implemented in Herwig++2.3 [106], will provide an essential tool for analysing the upcoming results at the LHC.

Chapter 3

Implementing the POWHEG method for diphoton production in hadron collisions in the **Herwig++** parton shower

For Higgs masses below 140 GeV, the decay of the Higgs into two photons is one of the most promising discovery channel for Higgs detection at the LHC [107–111]. The $\gamma\gamma$-decay mode can be well identified experimentally but the signal is small compared to the background. In Fig. 3.1a the Higgs signal, shown for different masses, is scaled by a factor 10 to be visible above the large background. Several processes contribute to these backgrounds, as shown in the same figure. The *irreducible* backgrounds are given by two real prompt photons, produced from $q\bar{q} \to \gamma\gamma$ ($\gamma\gamma$ born) and $gg \to \gamma\gamma$ ($\gamma\gamma$ box). The *reducible* backgrounds are given by events where at least one final state jet is interpreted as a photon. The γ+jet sample originates from two possible sources: either two prompt photons with one γ radiated during the fragmentation of the jet (γ+jets (2 prompt γ)) or one prompt photon and the other candidate corresponding to a mis-identified jet or isolated π^0 (γ+jet (1 prompt γ + 1 fake)). Furthermore, we can mis-identify both jets in the final states of processes such as Drell-Yan and hadron-hadron$\to$ jets.

In the present Chapter we will consider one of the main candidates to these backgrounds: the prompt photon production in hadron-hadron collisions. Diphoton ($\gamma\gamma$) production at large invariant mass ($M_{\gamma\gamma}$) is not only a large background for the discovery channel of the Higgs boson decaying into a pair of photons for the CERN LHC experiments [112, 113] and the Fermilab Tevatron [114], but it also constitutes an important background for new physics, such as heavy resonances [115], extra spatial dimensions [116] and cascade decays of heavy new particles [117]. Measurement involving $\gamma\gamma$-production have already been carried out at fixed-target [118–120] and collinear experiments [121–125].

The theoretical understanding of diphoton production and precise measurements of the differential cross section of the process are therefore not only important for the discovery of new phenomena but also as a check of the validity of the predictions of perturbative quantum chromodynamics (pQCD) and soft-gluon resummation meth-
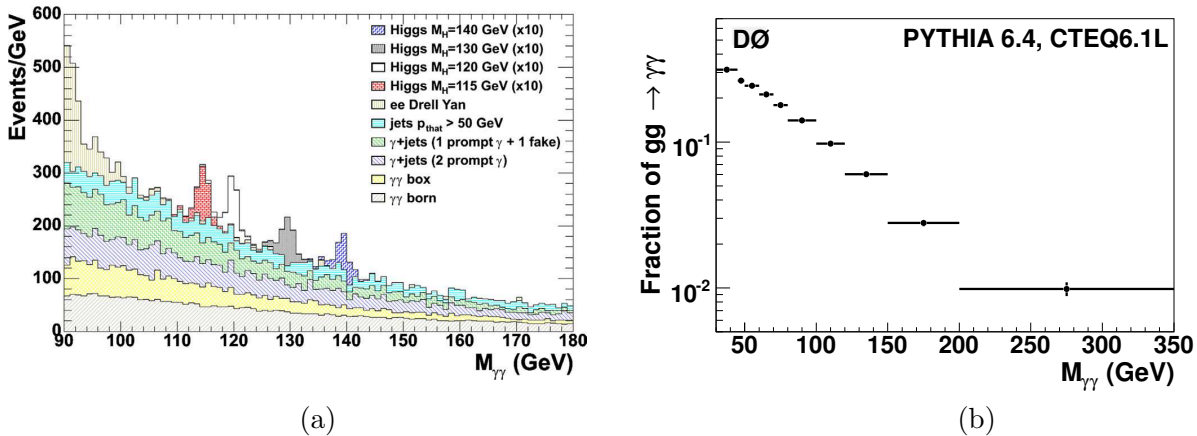
Figure 3.1: Backgrounds to the Higgs boson decay channel into $\gamma\gamma$ (a). The figure is presented in Ref. [113]. The 2-prompt photons production is an important candidate for such backgrounds and is given by $q\bar{q} \to \gamma\gamma$, $gg \to \gamma\gamma$ and γ + jet production with one of the photons radiated during the fragmentation of the jet. The $gg \to \gamma\gamma$ process can be important and even comparable to the leading-order contribution at low diphoton mass ($M_{\gamma\gamma}$) (b). The figure on the right panel is presented in Ref. [125]. The distribution is plotted with PYTHIA and gives the fraction of events produced via $\gamma\gamma$-box relative to the total $\gamma\gamma$-production as a function of $M_{\gamma\gamma}$.

ods [125].

The dominant production method for direct photon pairs is leading order $q\bar{q}$ scattering, although the formally next-to-next-to-leading order, $\mathcal{O}(\alpha_s^2)$, gluon-gluon fusion process via a quark-loop diagram [126] can be important, and even comparable to the leading-order contribution at low diphoton mass ($M_{\gamma\gamma}$) [125] due to the large gluon parton distribution function. This is shown in Fig. 3.1b. The distribution is plotted with the PYTHIA event generator and is presented in Ref. [125]. It gives the fraction of events produced via $gg \to \gamma\gamma$ relative to the total diphoton production as a function of $M_{\gamma\gamma}$.

The $\mathcal{O}(\alpha_s)$ corrections to the $q\bar{q} \to \gamma\gamma$ process are given by the $q\bar{q} \to \gamma\gamma g$, $gq \to \gamma\gamma q$ and $g\bar{q} \to \gamma\gamma\bar{q}$ subprocesses and corresponding virtual corrections. Moreover, the contribution where the final parton is collinear to a photon is calculated in terms of the quark and gluon fragmentation function into photons [126, 127]. We will give more details about fragmentation functions in Sect. 3.2. Given the behaviour of the latter functions, $\sim \frac{\alpha}{\alpha_s}$, these terms contribute to the same order as $q\bar{q} \to \gamma\gamma$. The QCD corrections to the process are well known in the literature [128–133]. They are large compared to most new physics [124], and thus the understanding of the QCD production mechanism is crucial for the research of new physics in this channel.

However, the inclusive production rate of high p_T π^0, η, ω or of pairs like $\pi^0\pi^0$, $\pi^0\gamma$, and similarly for η and ω, is an order of magnitude bigger than for direct photons. For this reason the experimental selection of direct photons requires the use of isolation cut. Different criteria for the isolation of photons have been developed in recent years: the cone approach [128, 134], the democratic approach [135] and the smooth isolation procedure [136]. Monte Carlo programs, such as JETPHOX [137]

and DIPHOX [138], provide simulation for direct photon production together with the implementation of isolation cuts.

The present Chapter is devoted to the implementation of the POWHEG method for the $\gamma\gamma$-production in hadron collisions in the Herwig++ parton shower [139]. It is organized as follows. In Sect. 3.1 we introduce the POWHEG formulae useful for the description of our approach and our treatment of the photon fragmentation contribution. The calculation of the leading-order kinematics with NLO accuracy in the POWHEG approach is discussed in Sect. 3.2. In Sect. 3.3 we describe the procedure used to generate the hardest emission. We show our results in Sect. 3.4 and finally present our conclusions in Sect. 3.5.

3.1 Modification of POWHEG

In order to use the POWHEG method for processes involving photons where the real emission matrix elements contain both QCD singularities from the emission of soft and collinear gluons and QED singularities from the radiation of soft and collinear photons we need to make some modifications to the POWHEG approach. We start by writing the real emission piece as

$$R(\Phi_B, \Phi_R) = R_{\text{QED}}(\Phi_B, \Phi_R) + R_{\text{QCD}}(\Phi_B, \Phi_R), \tag{3.1}$$

where

$$R_{\text{QED}}(\Phi_B, \Phi_R) = \frac{\sum_i D^i_{\text{QED}}}{\sum_j D^j_{\text{QED}} + \sum_j D^j_{\text{QCD}}} R(\Phi_B, \Phi_R), \tag{3.2a}$$

contains the collinear photon emission singularities and

$$R_{\text{QCD}}(\Phi_B, \Phi_R) = \frac{\sum_i D^i_{\text{QCD}}}{\sum_j D^j_{\text{QED}} + \sum_j D^j_{\text{QCD}}} R(\Phi_B, \Phi_R). \tag{3.2b}$$

contains the singularities associated with QCD radiation.[1] Here the counter terms have been split into those D^i_{QCD} which regulate the singularities from QCD radiation and those D^i_{QED} which regulate the singularities due to photon radiation.

We can regard the real QCD emission terms as part of the QCD corrections to the leading-order process, whereas the QED contributions are part of the photon fragmentation contribution coming from a leading-order process with one less photon and an extra parton. We therefore modify the next-to-leading order cross section for processes with photon production giving

$$d\sigma = \left\{ B(\Phi_B) + V(\Phi_B) + \int \left[R_{\text{QCD}}(\Phi_B, \Phi_R) - \sum_i D^i_{\text{QCD}}(\Phi_B, \Phi_R) \right] d\Phi_R \right\} d\Phi_B$$
$$+ R_{\text{QED}}(\Phi_B, \Phi_R) d\Phi_R d\Phi_B. \tag{3.3}$$

---

[1]In practice the counter terms can be negative in some regions and we choose to use their magnitude in this separation in order to ensure that the real contributions are positive.

We can now write the cross section for photon production processes in the POWHEG approach in the same way as in Eqn. 1.84

$$
\begin{aligned}
\mathrm{d}\sigma = \quad & \bar{B}(\Phi_B)\mathrm{d}\Phi_B \left[\Delta_{\mathrm{QCD}}(0) + \frac{R_{\mathrm{QCD}}(\Phi_B, \Phi_R)}{B(\Phi_B)} \Delta_{\mathrm{QCD}}(k_T(\Phi_B, \Phi_R))\mathrm{d}\Phi_R \right] \quad (3.4) \\
& + B'(\Phi'_B)\mathrm{d}\Phi'_B \left[\Delta_{\mathrm{QED}}(0) + \frac{R_{\mathrm{QED}}(\Phi'_B, \Phi'_R)}{B'(\Phi'_B)} \Delta_{\mathrm{QED}}(k_T(\Phi'_B, \Phi'_R))\mathrm{d}\Phi'_R \right],
\end{aligned}
$$

where $\bar{B}(\Phi_B)$ is now defined as

$$
\bar{B}(\Phi_B) = \left\{ B(\Phi_B) + V(\Phi_B) + \int \left[R_{\mathrm{QCD}}(\Phi_B, \Phi_R) - \sum_i D^i_{\mathrm{QCD}}(\Phi_B, \Phi_R) \right] \mathrm{d}\Phi_R \right\} \mathrm{d}\Phi_B
$$
(3.5)

and $B'(\Phi'_B)$ is the leading-order contribution for the process with an extra parton and one less photon with Φ'_B and Φ'_R being the corresponding Born and real emission phase-space variables.

The Sudakov form factor for QCD radiation is

$$
\Delta_{\mathrm{QCD}}(p_T) = \exp \left[- \int \mathrm{d}\Phi_R \frac{R_{\mathrm{QCD}}(\Phi_B, \Phi_R)}{B(\Phi_B)} \theta(k_T(\Phi_B, \Phi_R) - p_T) \right], \quad (3.6a)
$$

and the Sudakov form factor for QED radiation is

$$
\Delta_{\mathrm{QED}}(p_T) = \exp \left[- \int \mathrm{d}\Phi'_R \frac{R_{\mathrm{QED}}(\Phi'_B, \Phi'_R)}{B'(\Phi'_B)} \theta(k_T(\Phi'_B, \Phi'_R) - p_T) \right]. \quad (3.6b)
$$

The POWHEG algorithm is implemented for photon production processes using the following procedure.

- First select either a direct photon production or a fragmentation event using $\bar{B}(\Phi_B)$ and $B'(\Phi'_B)$ and the competition method to correctly generate the relative contributions of the two different processes.

- For a direct photon production process:

  - generate the hardest emission using the Sudakov form in Eqn. 3.6a;
  - directly hadronize non-radiative events;
  - map the radiative variables parametrising the emission onto the evolution scale, momentum fraction and azimuthal angle, $(\tilde{q}_h, z_h, \phi_h)$, from which the parton shower would reconstruct identical momenta;
  - generate the N-body configuration from $\bar{B}(\Phi_B)$ and evolve the radiating parton from the starting scale down to $\tilde{q}_h$ using the truncated shower;
  - insert a branching with parameters $(\tilde{q}_h, z_h, \phi_h)$ into the shower when the evolution scale reaches $\tilde{q}_h$;
  - generate p_T vetoed showers from all the external legs.

- For a fragmentation contribution:
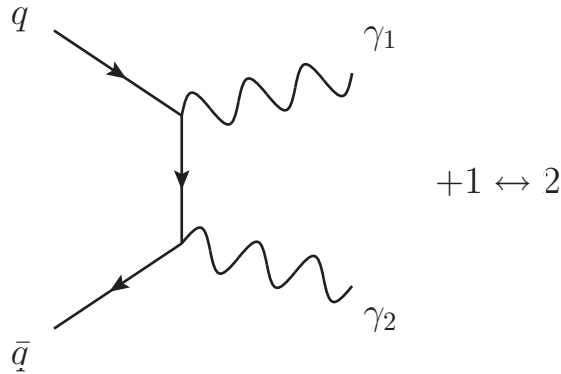
Figure 3.2: Diphoton production at leading-order.

- generate the hardest QED emission using the Sudakov form factor in Eqn. 3.6b;

- directly shower and hadronize non-radiative events, forbidding any perturbative QED radiation in the parton shower;

- for events with QED radiation map the radiative variables parametrising the emission into the evolution scale, momentum fraction and azimuthal angle, $(\tilde{q}_h, z_h, \phi_h)$, from which the parton shower would reconstruct identical momenta;

- generate the N-body configuration from $B'(\Phi'_B)$ and evolve the radiating parton from the starting scale down to $\tilde{q}_h$ using the truncated shower, but allowing QCD radiation with p_T greater than that of the hardest QED emission;

- insert a branching with parameters $(\tilde{q}_h, z_h, \phi_h)$ into the shower when the evolution scale reaches $\tilde{q}_h$;

- generate the shower from all external legs forbidding QED radiation, but not QCD radiation, above the p_T of the hardest emission.

This procedure now includes both the QCD corrections to the leading-order direct photon production process and both the perturbative QED corrections to the photon fragmentation contribution and the non-perturbative contribution is simulated by the parton shower.

In the next two sections we will describe how we implemented this approach in Herwig++ for photon pair production.

3.2 Calculation of $\bar{B}(\Phi_B)$

In this section we describe the $\mathcal{O}(\alpha_s)$ corrections to diphoton production. At leading-order, $\gamma\gamma$-production is described by the Feynman diagram illustrated in Fig. 3.2. Next-to-leading order contributions yield $\mathcal{O}(\alpha_s)$ corrections coming from $q\bar{q} \to \gamma\gamma g$, $gq \to \gamma\gamma q$ and $g\bar{q} \to \gamma\gamma\bar{q}$, together with the corresponding virtual corrections, as shown in Fig. 3.3. These subprocesses contain QED singularities, corresponding to
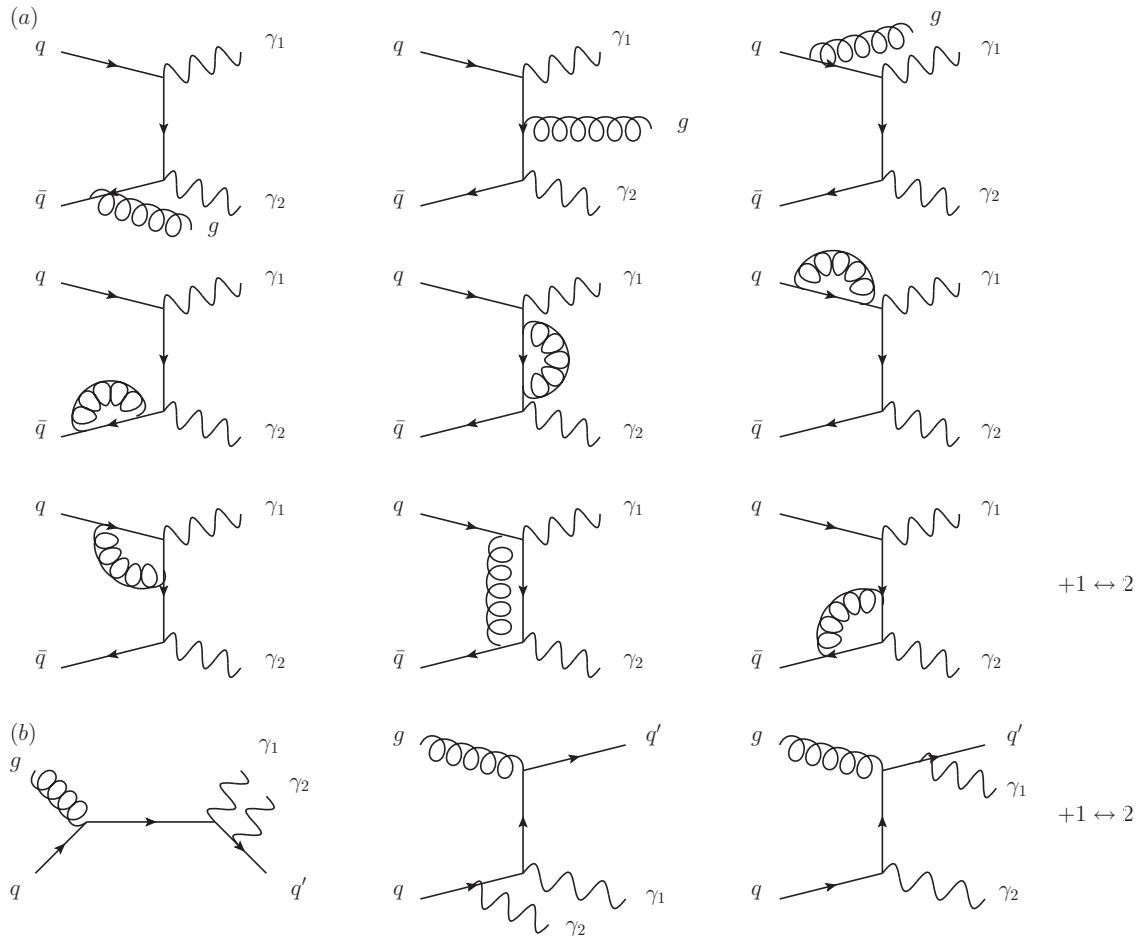
Figure 3.3: Diphoton production at next-to-leading order. In (a) the real and virtual Feynman diagrams contributing to the $q\bar{q} \to \gamma\gamma$ subprocess are shown while in (b) the real diagrams for the gq initiated process are given.

configurations where the final-state parton becomes collinear to a photon, which do not cancel when summing up the real and the virtual pieces of the cross section. They are formally absorbed into a quark ($G_{\gamma q}(z, \mu^2)$) or gluon ($G_{\gamma g}(z, \mu^2)$) fragmentation function into photons, which define the probability of finding a photon carrying longitudinal momentum fraction z in a quark or gluon jet at scale μ for a given factorization scheme. This QED singular component is called the *Bremsstrahlung* or single fragmentation contribution, see Fig. 3.4. In our approach it is treated separately and simulated by showering the $gq \to \gamma q$ or $g\bar{q} \to \gamma\bar{q}$ within the Monte Carlo algorithm as described in the previous section. At next-to-leading order the same configuration appears in any subprocess in which a quark (gluon) undergoes a cascade of successive collinear splittings ending up with a quark-photon (gluon-photon) splitting. These singularities are factorized to all orders in α_s, according to the factorization theorem. When the fragmentation scale μ is chosen higher than any other hadronic scale, *i.e.* $\mu \sim 1$ GeV, these functions behave roughly as $\frac{\alpha}{\alpha_s(\mu^2)}$ and therefore contribute at leading-order.

For a full study at NLO accuracy, the $\mathcal{O}(\alpha_s)$ corrections to the Bremsstrahlung
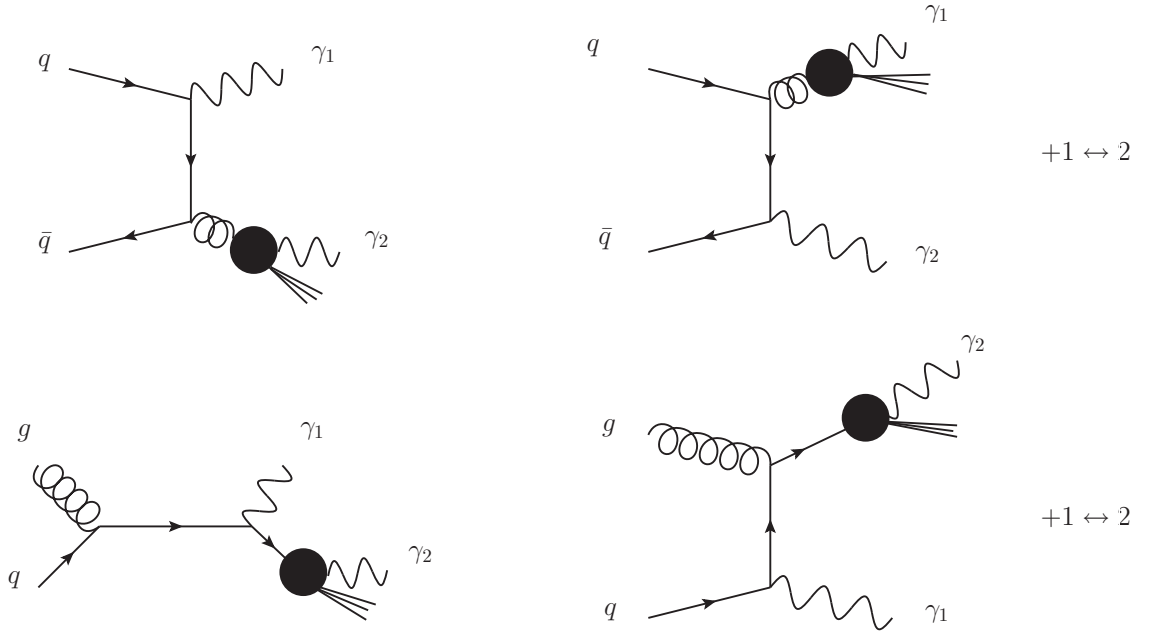
Figure 3.4: Bremsstrahlung contribution for diphoton production.

contribution need to be calculated. Moreover, these corrections in their turn yield the leading order contribution of the double fragmentation type process; in the latter case, both photons result from the collinear fragmentation of a parton. However, these corrections are out of the scope of the present work and are not considered here.

3.2.1 Real emission contribution

In order to calculate the real emission contribution to $\bar{B}(\Phi_B)$ we need to specify both the radiative phase-space, Φ_R, and the subtraction counter terms. We choose to use the dipole subtraction algorithm of Catani and Seymour [36] to specify the counter terms and the associated definition of the real emission phase-space as follows.

In the centre of mass frame the incoming hadronic momenta are $P_\oplus$ and $P_\ominus$ respectively for the hadrons traveling in the positive and negative z-directions. Similarly the momenta of the incoming partons in the Born process are $\bar{p}_\oplus = \bar{x}_\oplus P_\oplus$ and $\bar{p}_\ominus = \bar{x}_\ominus P_\ominus$, respectively. The momenta of the photons in the Born process are $\bar{k}_{1,2}$ respectively. The corresponding momenta in the real emission process are $p_\oplus$ and $p_\ominus$ for the incoming partons and $k_{1,2,3}$ for the outgoing particles, which are chosen such that $k_{1,2}$ are the momenta of the photons and k_3 that of the radiated final-state parton.

In the CS approach the real phase-space depends on which parton is the emitter of the radiation and which the associated spectator defining the dipole [36]. When the parton with momentum $\bar{p}_\oplus$ is the emitter and that with momenta $p_\ominus$ the

spectator the full phase-space is [36]

$$d\Phi_3 = d\Phi_B d\Phi_R = d\Phi_B \frac{(k_1 + k_2)^2}{16\pi^2} \frac{d\phi_\oplus}{2\pi} dv_\oplus \frac{dx}{x} \theta(v_\oplus) \theta\left(1 - \frac{v_\oplus}{1-x}\right) \theta(x(1-x)) \theta(x - \bar{x}_\oplus),$$
(3.7)

where the radiative phase-space variables are

$$x = 1 - \frac{(p_\oplus + p_\ominus) \cdot k_3}{p_\oplus \cdot p_\ominus}, \qquad v_\oplus = \frac{p_\oplus \cdot k_3}{p_\oplus \cdot p_\ominus}, \qquad \phi_\oplus,$$
(3.8)

$\phi_\oplus$ is the azimuthal angle of the emitted particle around the $\hat{\oplus}$-direction and

$$x \in [x_\oplus, 1], \qquad v_\oplus \in [0, 1-x].$$
(3.9)

In terms of these variables

$$p_\oplus = \bar{p}_\oplus / x, \qquad p_\ominus = \bar{p}_\ominus,$$
(3.10a)

$$x_\oplus = \bar{x}_\oplus / x, \qquad x_\ominus = \bar{x}_\ominus.$$
(3.10b)

It is useful to specify the momenta of the radiated parton in terms of its transverse momentum, p_T, and rapidity, y, such that

$$k_3 = p_T (\cosh y; \cos \phi_\oplus, \sin \phi_\oplus, \sinh y).$$
(3.11)

Using the definition of x and $v_\oplus$

$$k_3 = v_\oplus p_\ominus + (1 - x - v_\oplus)p_\oplus + q_\perp,$$
(3.12)

where $q_\perp$ is the component of the 4-momenta transverse to the beam direction. The on-shell condition, $k_3^2 = 0$, gives

$$-q_\perp^2 = p_T^2 = 2p_\oplus \cdot p_\ominus(1 - x - v_\oplus)v_\oplus.$$
(3.13)

From Eqn.3.12 and the definition of rapidity

$$y = \frac{1}{2}\ln\left[\frac{k_3^E + k_3^z}{k_3^E - k_3^z}\right] = \frac{1}{2}\ln\left[\frac{(1 - x - v_\oplus)x_\oplus}{v_\oplus x x_\ominus}\right],$$
(3.14)

the CS variables are

$$\begin{cases} v_\oplus = \frac{1}{x_\ominus \sqrt{\hat{s}}} \frac{p_T}{e^y}, \\[2ex] x = \frac{1 - \frac{p_T}{x_\ominus \sqrt{\hat{s}} e^y}}{1 + \frac{p_T e^y}{x_\oplus \sqrt{\hat{s}}}}. \end{cases}$$
(3.15)

This is sufficient to calculate the momentum of the radiated parton. However rather than implementing the real emission variables in the Sudakov form factor in this way and then imposing the $\theta(k_T(\Phi_B, \Phi_R) - p_T)$ function, it is easier to transform the real emission into the transverse momentum, rapidity and azimuthal angle of the emitted parton.

The Jacobian for this transformation is

$$\left| \frac{\partial(x,v)}{\partial p_T \partial y} \right| = \frac{\frac{2p_T}{sx_\oplus x_\ominus} \left(1 - \frac{p_T e^{-y}}{\sqrt{s}x_\ominus} \right)}{\left(1 + \frac{p_T e^y}{\sqrt{s}x_\oplus} \right)^2} = \frac{2p_T x^2}{sx_\oplus x_\ominus (1 - v_\oplus)}. \tag{3.16}$$

The momenta of the photons in the real emission process can then be calculated from the Born momenta

$$k_r^\mu = \Lambda^\mu{}_\nu \bar{k}_r^\nu \qquad\qquad r = 1, 2, \tag{3.17}$$

where the Lorentz transformation is

$$\Lambda^\mu{}_\nu = g^\mu{}_\nu - \frac{2(K + \bar{K})^\mu (K + \bar{K})_\nu}{(K + \bar{K})^2} + \frac{2K^\mu \bar{K}_\nu}{K^2}, \tag{3.18}$$

with

$$K = p_\oplus + p_\ominus - k_3 = k_1 + k_2 \tag{3.19a}$$
$$\bar{K} = \bar{p}_\oplus + \bar{p}_\ominus. \tag{3.19b}$$

The condition $K^2 = \bar{K}^2$ is compatible with the definition of x given in Eqn. 3.8. The kinematic variables for the $\hat{\ominus}$ collinear direction are calculated in a similar way and they provide a radiative phase-space as in Eqn. 3.7. Moreover, given the $x_\oplus \leftrightarrow x_\ominus$ asymmetry of the rapidity in Eqn. 3.14, it is $[y]_\ominus = -[y]_\oplus$. In the rest of the paper we refer to the collinear direction as $\hat{O} = \{\hat{\ominus}, \hat{\oplus}\}$, when both components need to be included.

In addition to the real emission variables we need the dipole subtraction terms of Ref. [36]. In the following $B(\Phi_B)$ is computed in terms of the reduced momenta defined in terms of the momenta for the real emission process in Ref. [36]. The QCD singularities from $q\bar{q} \rightarrow \gamma\gamma g$ are absorbed by the dipoles

$$D^{qg,\bar{q}} \equiv D^{qg}_{\text{QCD}} = \frac{C_F \alpha_s(\mu_R)}{2\pi} \frac{1}{\bar{p}_\oplus k_3} \left\{ \frac{2}{1-x} - (1+x) \right\} B(\Phi_B), \tag{3.20a}$$

$$D^{\bar{q}g,q} \equiv D^{\bar{q}g}_{\text{QCD}} = \frac{C_F \alpha_s(\mu_R)}{2\pi} \frac{1}{\bar{p}_\ominus k_3} \left\{ \frac{2}{1-x} - (1+x) \right\} B(\Phi_B), \tag{3.20b}$$

where the dipoles $D^{ij,k}$ denote the emitter i, emitted parton j and spectator k.

The $gq \rightarrow \gamma\gamma q$ subprocess involves the QCD dipoles

$$D^{gq,q} \equiv D^{gq}_{\text{QCD}} = \frac{T_F \alpha_s(\mu_R)}{2\pi} \frac{1}{4\bar{p}_\oplus k_3} \left\{ 1 - 2x(1-x) \right\} B(\Phi_B). \tag{3.21}$$

In order to separate the QCD and QED emission we also need the QED dipoles

$$D^q_{q\gamma} \equiv D^{q\gamma F}_{\text{QED}} = e_q^2 \frac{1}{2k_2 k_3 \xi} \left\{ \frac{2}{2 - \xi - z} - (1+z) \right\} B'(\Phi'_B), \tag{3.22a}$$

$$D^{q\gamma}_q \equiv D^{q\gamma I}_{\text{QED}} = e_q^2 \frac{1}{2p_\ominus k_3 \xi} \left\{ \frac{2}{1 - \xi + z} - (1+z) \right\} B'(\Phi'_B), \tag{3.22b}$$

where

$$\xi = 1 - \frac{k_2 k_3}{(k_2 + k_3)p_\oplus}, \tag{3.23a}$$

$$z = \frac{p_\oplus k_2}{(k_2 + k_3)p_\oplus}, \tag{3.23b}$$

and e_q is the charge of the quark q in units of the electron charge. In this case, the radiative phase-space is $\mathrm{d}\Phi'_R(\xi, z, \phi')$. Similar dipoles are included for the $g\bar{q} \to \gamma\gamma\bar{q}$ subprocess. We do not include perturbative QED radiation from the $q\bar{q} \to \gamma g$ subprocess as it does not give a perturbative correction to $G_{\gamma g}(z, \mu^2)$.

In practice we generate the real emission piece as a contribution from each of the incoming partons as

$$\int \left[R_{\mathrm{QCD}}(\Phi_B, \Phi_R) - \sum_i D^i_{\mathrm{QCD}}(\Phi_B, \Phi_R) \right] \mathrm{d}\Phi^i_R = \tag{3.24}$$

$$\sum_{i=\oplus,\ominus} \int \left[\frac{|D^i_{\mathrm{QCD}}|}{\sum_j |D^j_{\mathrm{QED}}| + \sum_j |D^j_{\mathrm{QCD}}|} R(\Phi_B, \Phi^i_R) - D^i_{\mathrm{QCD}}(\Phi_B, \Phi_R) \right] \mathrm{d}\Phi^i_R,$$

For the later generation of the Sudakov form factor it is useful to express the dipoles as

$$D^I_{\mathrm{QCD}} \equiv \frac{\mathcal{C}_I \alpha_s(\mu_R)}{2\pi} \mathcal{D}^I B(\Phi_B), \tag{3.25}$$

where $I = \{qg; \bar{q}g; gq; g\bar{q}\}$,

$$\mathcal{C}_{qg} = \mathcal{C}_{\bar{q}g} = C_F, \tag{3.26}$$
$$\mathcal{C}_{gq} = \mathcal{C}_{g\bar{q}} = T_F, \tag{3.27}$$

and

$$D^J_{\mathrm{QED}} \equiv e_q^2 \mathcal{D}_J B(\Phi'_B), \tag{3.28}$$

where $J = \{q\gamma F, q\gamma I, \bar{q}\gamma F, \bar{q}\gamma I\}$.

3.2.2 Virtual contribution and collinear remainders

The finite piece of the virtual correction is

$$\mathrm{d}\sigma_V = \frac{C_F \alpha_s(\mu_R)}{2\pi} V(w) B(\Phi_B). \tag{3.29}$$

where the finite contribution of $\mathbf{I}(\epsilon)$ [36] and the virtual correction [131] is

$$V(w) = \left(3 + \ln^2 w + \ln^2(1-w) + 3\ln(1-w)\right) + \frac{F(w)}{\left(\frac{1-w}{w} + \frac{w}{1-w}\right)}, \tag{3.30}$$

where e_q is the electric charge of quark q, and

$$F(w) = 2\mathrm{ln}w + 2\mathrm{ln}(1-w) + \frac{3(1-w)}{w}(\mathrm{ln}w - \mathrm{ln}(1-w))$$
$$+ \left(2 + \frac{w}{1-w}\right)\mathrm{ln}^2 w + \left(2 + \frac{1-w}{w}\right)\mathrm{ln}^2(1-w), \qquad (3.31)$$

with $w = 1 + \frac{\hat{t}}{\hat{s}}$, where $\hat{s}$ and $\hat{t}$ are the usual Mandlestam variables.

The collinear remainders are

$$\mathrm{d}\sigma_{\mathrm{coll}} = \frac{C_F \alpha_s(\mu_R)}{2\pi} \frac{f^m(x_\mathrm{O}, \mu_F)}{f(x_\mathrm{O}, \mu_F)} B(\Phi_B), \qquad (3.32)$$

where the modified PDF is[2]

$$f_q^m(x_\mathrm{O}, \mu_F) = \int_{x_\mathrm{O}}^1 \frac{\mathrm{d}x}{x} \left\{ f_g\left(\frac{x_\mathrm{O}}{x}, \mu_F\right) A(x) \right.$$
$$+ \left[f_q\left(\frac{x_\mathrm{O}}{x}, \mu_F\right) - x f_q(x_\mathrm{O}, \mu_F) \right] B(x)$$
$$\left. + f_q\left(\frac{x_\mathrm{O}}{x}, \mu_F\right) C(x) \right\} + f_q(x_\mathrm{O}, \mu_F) D(x_\mathrm{O}), \qquad (3.33)$$

f_q and f_g are the quark and gluon PDFs respectively, and

$$A(x) = \frac{T_F}{C_F} \left[2x(1-x) + (x^2 + (1-x)^2)\mathrm{ln}\frac{Q^2(1-x)^2}{\mu_F^2 x} \right], \qquad (3.34)$$

$$B(x) = \left[\frac{2}{1-x}\mathrm{ln}\frac{Q^2(1-x)^2}{\mu_F^2} \right], \qquad (3.35)$$

$$C(x) = \left[1 - x - \frac{2}{1-x}\mathrm{ln}x - (1+x)\mathrm{ln}\frac{Q^2(1-x)^2}{\mu_F^2 x} \right], \qquad (3.36)$$

$$D(x_\mathrm{O}) = \left[\frac{3}{2}\mathrm{ln}\left(\frac{Q^2}{\mu_F^2}\right) + 2\mathrm{ln}(1-x_\mathrm{O})\mathrm{ln}\left(\frac{Q^2}{\mu_F^2}\right) + 2\mathrm{ln}^2(1-x_\mathrm{O}) + \frac{\pi^2}{3} - 5 \right]. \qquad (3.37)$$

The combined contribution of the finite virtual term and collinear remnants is

$$\mathrm{d}\sigma_{V+\mathrm{coll}} = \frac{C_F \alpha_s(\mu_R)}{2\pi} \mathcal{V}(\Phi_B) B(\Phi_B), \qquad (3.38)$$

where

$$\mathcal{V}(\Phi_B) \equiv V(w) + \tilde{V}(x_\mathrm{O}, \mu_F), \qquad (3.39)$$

where $\tilde{V}(x_\mathrm{O}, \mu_F) = \frac{f^m(x_\mathrm{O}, \mu_F)}{f(x_\mathrm{O}, \mu_F)}$.

3.2.3 Generation of the hard process

The next-to-leading order simulation of photon pair production in Herwig++ uses the standard Herwig++ machinery to generate photon pair and photon plus jet production in competition. The $\bar{B}$ function is implemented as a reweighting of the leading-order matrix element as follows:

---

[2]We write the modified PDF for the quark q, but a similar expression is valid for an incoming antiquark $\bar{q}$.

1. the radiative variables $\Phi_R\{x, v, \phi\}$ and $\Phi'_R\{\xi, z, \phi'\}$ are transformed into a new set such that the radiative phase-space is a unit volume;

2. using the standard Herwig++ leading-order matrix element generator, we generate a leading-order configuration and provide the Born variables Φ_B with an associated weight $B(\Phi_B)$;

3. the radiative variables Φ_R are generated and $\bar{B}(\Phi_B)$ sampled in terms of the unit cube $(\tilde{x}, \tilde{v}, \tilde{\phi})$, using the Auto-Compensating Divide-and-Conquer (ACDC) phase-space generator [101];

4. the leading-order configuration is accepted with a probability proportional to the integrand of Eqn. 3.5 evaluated at $\{\Phi_B, \Phi_R\}$.

3.3 The generation of the hardest emission

Following the generation of the Born kinematics with next-to-leading order accuracy the hardest QCD or QED emission must be generated according to Eqns. 3.6a or 3.6b respectively, depending on whether a direct or photon fragmentation contribution was selected.

3.3.1 The hardest QED emission

The hardest QED emission is generated by using the modified Sudakov form factor defined in Eqn. 3.6b. We generate it in terms of the variables $\Phi'_R(x_p, z_p, \phi)$, with

$$\mathrm{d}\Phi'_R = \frac{1}{2\pi}\mathrm{d}x_p\mathrm{d}z_p\mathrm{d}\phi, \tag{3.40}$$

defined in [44, 48], where $x_p \in [x_o, 1]$, $z_p \in [0, 1]$ and the azimuthal angle $\phi \in [0, 2\pi]$. The invariant mass of the initial-final dipole $q^2 = (p_i - p_k)^2 = -Q^2$ is preserved by the photon radiation. It is easiest to generate the hardest emission by introducing $x_\perp$ such that the transverse momentum of the emission relative to the direction of the partons in the Breit frame of the dipole is $p_T = \frac{Q}{2}x_\perp$ where

$$x_\perp^2 = \frac{4(1-x_p)(1-z_p)z_p}{x_p}. \tag{3.41}$$

The Sudakov form factor can then be calculated in terms of $\tilde{\Phi}'_R(x_\perp, z_p, \phi)$, such that the θ-function simply gives $x_\perp$ as integration limits and Eqn. 3.6b becomes

$$\Delta^J_{\mathrm{QED}}(x_\perp) = \exp\left(-\int_{x_\perp}^{x_\perp^{\max}} \frac{\mathrm{d}x'_\perp}{x'^3_\perp}\mathrm{d}\phi\mathrm{d}z_p\frac{\alpha}{2\pi}\mathcal{W}\frac{\mathcal{A}^J_{\mathrm{QED}}}{B}\right), \tag{3.42}$$

where

$$\frac{\alpha}{2\pi}\mathcal{A}^J_{\mathrm{QED}}\frac{|D^i_{\mathrm{QCD}}|}{\sum_j |D^j_{\mathrm{QED}}| + \sum_j |D^j_{\mathrm{QCD}}|}R(\Phi_B, \Phi^J_R), \tag{3.43}$$

the Jacobian, $\mathcal{W}$, is

$$\mathcal{W} = 4z_p(1 - z_p)(1 - x_p)^2, \tag{3.44}$$

and $\frac{Q}{2}x_\perp^{\max}$ is the maximum value for the transverse momentum.

It is impossible to generate the hardest emission directly using Eqn. 3.42, and so we instead use an overestimate

$$g(x_\perp) = \frac{a}{x_\perp^3}, \tag{3.45}$$

of the integrand in Eqn. 3.42 so that

$$\Delta_{\text{QED}}^{\text{over}}(x_\perp) = \exp\left(-\int_{x_\perp}^{x_\perp^{\max}} \frac{\mathrm{d}x_\perp'}{x_\perp'^3} \mathrm{d}\phi \mathrm{d}z_p a\right), \tag{3.46}$$

can be easily integrated in $\{x_\perp, x_\perp^{\max}\}$. This allows us to solve $\mathcal{R}_1 = \Delta_{\text{QED}}^{\text{over}}(x_\perp)$, where $\mathcal{R}_1$ is a random number in $[0, 1]$ to get the transverse momentum of a trial hard emission

$$x_\perp^2(\mathcal{R}_1) = \frac{1}{\frac{1}{(x_\perp^{\max})^2} - \frac{2}{a}\ln\mathcal{R}_1}. \tag{3.47}$$

This trial hard emission is then accepted or rejected using a probability given by the ratio of the true integrand to the overestimated value. If the emission is rejected the procedure is repeated with $x_\perp^{\max}$ set to the rejected $x_\perp$ value until the generated value is below the cut-off. This procedure, called the *veto algorithm*, correctly generates the hardest emission according to Eqn. 3.42 [26].

3.3.2 The hardest QCD emission

The hardest QCD emission is generated in terms of the variables $\Phi_R(p_T, y, \phi)$ defined in Sect.3.2.1. Eqn.3.6a then becomes

$$\Delta_{\text{QCD}}^I(p_T) = \exp\left(-\int_{p_T}^{p_T^{\max}} \mathrm{d}x_\perp' \mathrm{d}\phi \mathrm{d}y \frac{\mathcal{C}_I \alpha_s}{2\pi} \mathcal{W}_I \frac{\mathcal{A}_{\text{QCD}}^I}{B}\right), \tag{3.48}$$

where

$$\frac{\mathcal{C}_I \alpha_s}{2\pi} \mathcal{A}_{\text{QCD}}^I = \frac{|D_{\text{QCD}}^I|}{\sum_j |D_{\text{QED}}^j| + \sum_j |D_{\text{QCD}}^j|} R(\Phi_B, \Phi_R^I) \tag{3.49}$$

the Jacobian

$$\mathcal{W}_I = \frac{x}{1 - v_O}, \tag{3.50}$$

where we mean to use $v_\oplus$ for $I = \{qg; gq; g\bar{q}\}$ and $v_\ominus$ for $I = \{\bar{q}g\}$.

As before we use the veto algorithm to generate the hardest QCD emission according to Eqn. 3.48. In this case we introduce the overestimate function

$$g_I(p_T) = \frac{a_I}{p_T}, \tag{3.51}$$

so that

$$\Delta_{\text{QCD}}^{\text{over}}(p_T) = \exp\left(-\int_{p_T}^{p_T^{\max}} \frac{\mathrm{d}p_T'}{p_T'} \mathrm{d}\phi \mathrm{d}y a_I\right), \tag{3.52}$$

is easily integrable in $\{p_T, p_T^{\max}\}$ and $\mathcal{R}_1 = \Delta_{\text{QCD}}^{\text{over}}(p_T)$ can be solved giving

$$p_T(\mathcal{R}_1) = \mathcal{R}_1^{\frac{1}{a}}. \tag{3.53}$$

As before this trial hard emission is then accepted or rejected using a probability
given by the ratio of the true integrand to the overestimated value. If the emission
is rejected the procedure is repeated with $p_T^{\max}$ set to the rejected p_T value until the
generated value is below the cut-off.

3.4   Results

Unlike the implementations of many other processes in the POWHEG formalism it
is impossible to directly compare our results for any quantities directly with next-
to-leading-order simulations in order to test the implementation due to the very
different treatment of the photon fragmentation contribution. Instead we compare
a simple observable, the rapidity of the photons, with the next-to-leading-order pro-
gram DIPHOX [138] as a sanity check of our results not expecting exact agreement,
although the PDFs and electroweak parameters were chosen to give exact agreement
for the leading order $q\bar{q} \to \gamma\gamma$ process.

For proton-proton collisions at a centre-of-mass energy of 14 TeV, we used the
following set of cuts on p_T and rapidity of photons

$$p_T^\gamma > 25 \text{ GeV}, \qquad\qquad |y^\gamma| < 2.5, \tag{3.54}$$

together with a cut on the invariant mass of the $\gamma\gamma$-pair

$$80 \text{ GeV} < M^{\gamma\gamma} < 1500 \text{ GeV}. \tag{3.55}$$

Moreover, we follow typical experimental selection cuts to isolate direct photons
from the background: we require that the amount of total transverse energy, E_T^{had},
released in the cone, centred around the photon direction in the rapidity and az-
imuthal angle plane, is smaller than 15 GeV, *i.e.*

$$(y - y^\gamma)^2 + (\phi - \phi^\gamma)^2 \leq R^2 \tag{3.56}$$
$$E_T^{\text{had}} \leq 15 \text{ GeV}, \tag{3.57}$$

where $R = 0.4$ is the radius of the cone. The PDFs are chosen to be the CTEQ6
set [104]. The result is shown in Fig. 3.5. The distributions from DIPHOX at
NLO(red dashed line) and LO (red dash-dotted line), together with LO Herwig++
(dotted black line) and Herwig++ with POWHEG corrections (solid black line) do
not include the gluon-gluon channel. At LO the Herwig++ and DIPHOX distri-
butions are indistinguishable. At NLO they show a difference that is very small
compared to the correction from LO to NLO, which means that the NLO curves are
in reasonable agreement given the sizable contribution of the fragmentation contri-
bution that is treated differently in the two approaches.

In Fig. 3.6a we compare the results from Herwig++ with the data of Ref. [124],
a fixed next-to-leading-order calculation from DIPHOX (dotted magenta line) and
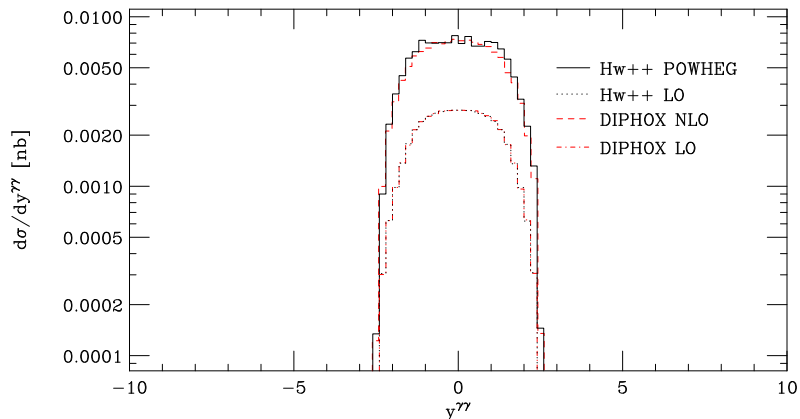
Figure 3.5: Rapidity of the $\gamma\gamma$-pair at NLO. The distribution from the Herwig++ parton shower with POWHEG correction (solid black line) is compared with NLO cross section from DIPHOX (dashed red line). At LO the Herwig++ distribution is given by the dotted black line while the cross section from DIPHOX by the dash-dotted red line.

RESBOS (dashed-dotted green line) [140–144], which performs an analytic resummation of the logarithmically enhanced contributions. Here and in the following the LO Herwig++ parton shower (red dashed line) includes the $q\bar{q} \to \gamma\gamma$, $qg \to \gamma$jet and $gg \to \gamma\gamma$ contribution. The implementation of POWHEG correction improves the description and this results in a distribution (solid blue line) that is in good agreement with the data. Here, as in the following, the NLO curve includes the $gg \to \gamma\gamma$ subprocess. In the lower frame, we plot the ratio MC/data and the yellow band gives the one sigma variation of data. All the plots comparing the results of Herwig++ with experimental results were made using the Rivet [145] package.

It is of interest to study the transverse momentum of the $\gamma\gamma$-pair, because it is not infrared safe for $p_\perp^{\gamma\gamma} \to 0$. The $q\bar{q} \to \gamma\gamma$ and $gg \to \gamma\gamma$ processes present a loss of balance between the corresponding real emission and virtual contribution, which results in large logarithms at every order in perturbation theory. In addition, the fragmentation components introduce an extra convolution that smears out this singularity. Since DIPHOX is based on a fixed, finite order calculation it is not suitable for the study of infrared sensitive observables and it fails in the description of these observables at low $p_\perp^{\gamma\gamma}$, as it is shown in Fig. 3.6b (dotted magenta line). Resummation for diphoton production in hadron-hadron collision has been provided at all orders in α_s in Ref. [146] and implemented in RESBOS, as the corresponding distribution (dashed-dotted green line) shows in the same figure. The Herwig++ parton shower resums the effect of enhanced collinear emission to all orders in α_s in the leading-logarithmic (LL) approximation and results in a finite behaviour for $p_\perp^{\gamma\gamma} \to 0$ (red dashed line). However, the LO distribution does not correctly describe the data. In presence of POWHEG correction the distribution (solid blue line) stays finite at low $p_\perp^{\gamma\gamma}$ and is in good agreement with the CDF data [124].

In addition, Herwig++ distributions, with and without POWHEG corrections, are compared to the data of Ref. [125]. In Fig. 3.7, we show the transverse momentum of the diphoton pair for two ranges of invariant mass of the $\gamma\gamma$-pair, $M_{\gamma\gamma}$; in

61
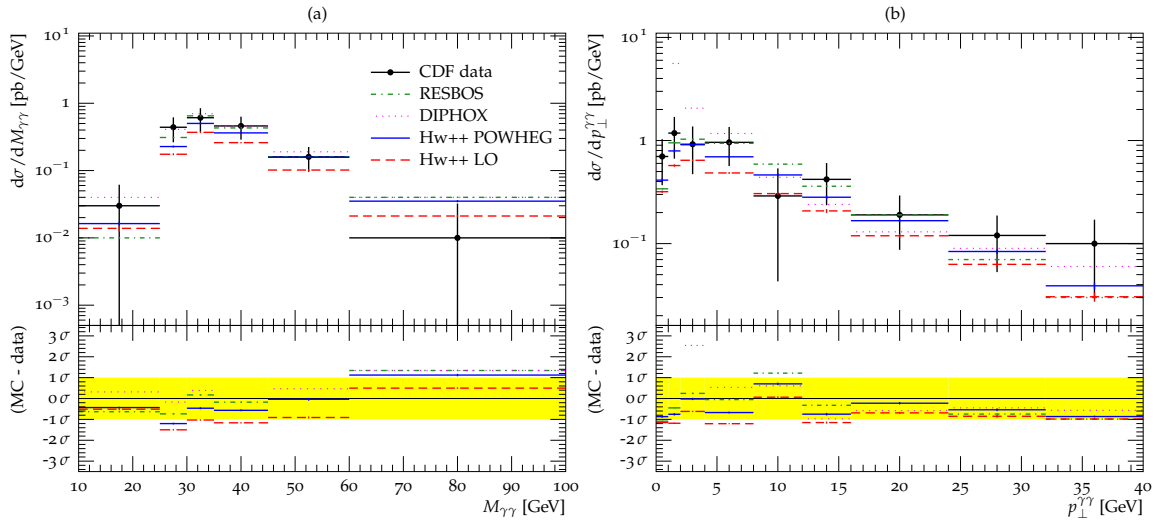
Figure 3.6: The (a) invariant mass and (b) transverse momentum of the $\gamma\gamma$-pair. The solid blue line shows the POWHEG approach, while the dashed red curve shows the result of the Herwig++ shower at LO. We show the NLO cross section provided by DIPHOX (magenta dotted line) and RESBOS (green dashed-dotted line). The data are from Ref. [124] and the curves are plotted with Rivet [145]. In the lower panel, the yellow band describes the one sigma variation of data.
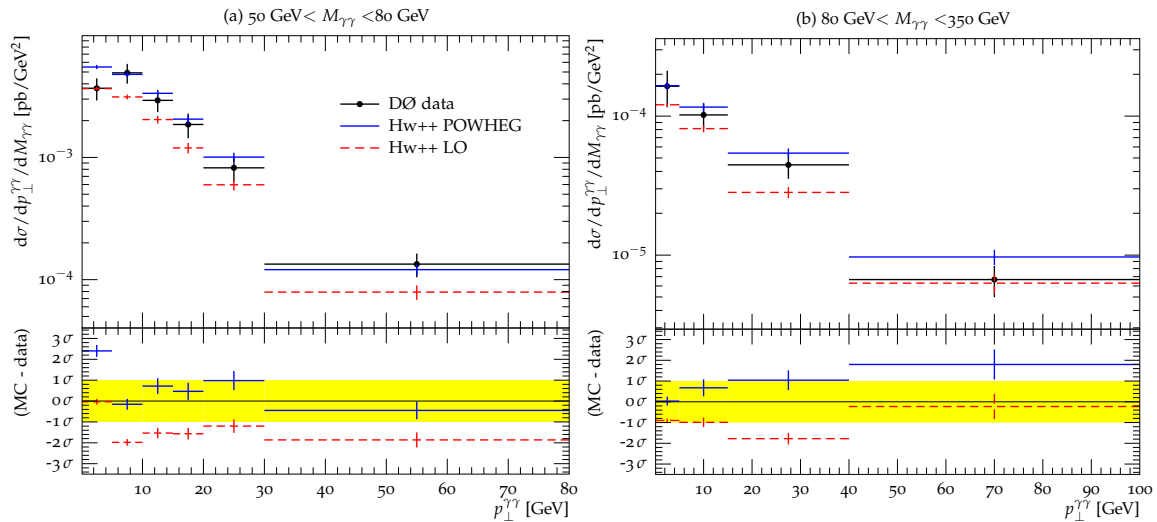
Figure 3.7: Transverse momentum of the diphoton system for (a) 50 GeV $< M_{\gamma\gamma} <$ 80 GeV and (b) 80 GeV $< M_{\gamma\gamma} <$ 350 GeV. The distribution for the POWHEG formalism (solid blue line) is plotted together with the distribution for the Herwig++ parton shower (dashed red line). The data are from Ref. [124] and the lower frame is as described in Fig. 3.6
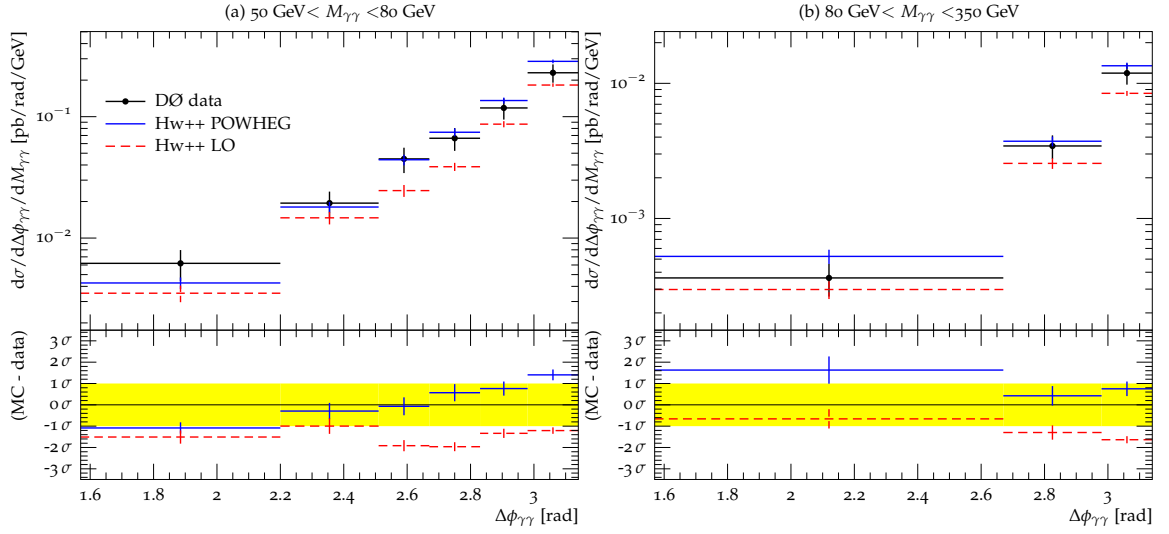
Figure 3.8: Azimuthal angle between the photons for (a) 50 GeV $< M_{\gamma\gamma} <$ 80 GeV and (b) 80 GeV $< M_{\gamma\gamma} <$ 350 GeV. The solid blue line shows the result for the Herwig++ shower with POWHEG corrections, while the red dashed line gives the result from the Herwig++ parton shower. The data are from Ref. [124] and the lower frame is as described in Fig. 3.6
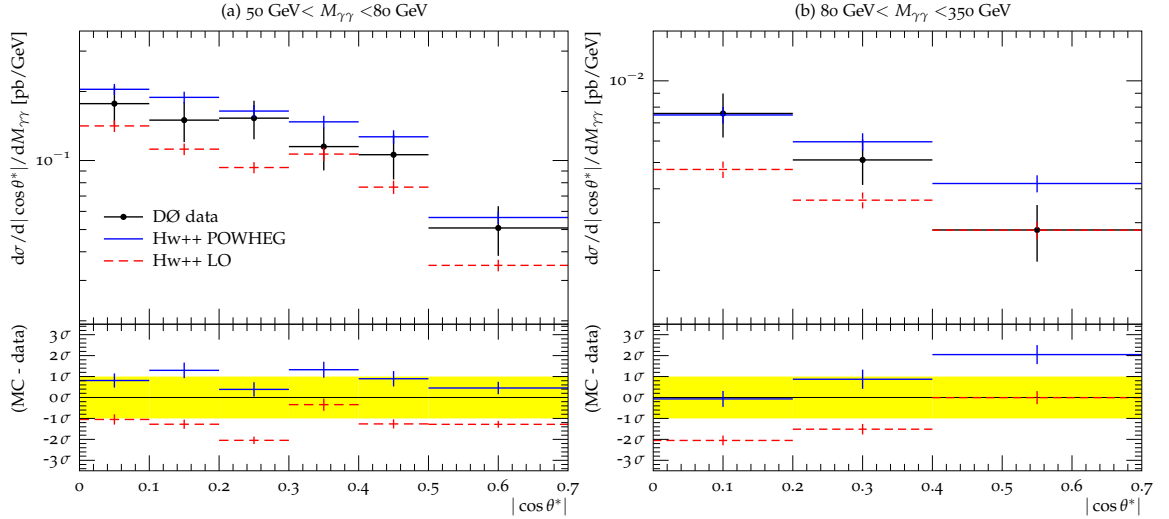
Figure 3.9: Polar scattering angle between the photons for two ranges of $M_{\gamma\gamma}$: 50 GeV $< M_{\gamma\gamma} <$ 80 GeV (a) and 80 GeV $< M_{\gamma\gamma} <$ 350 GeV (b). The solid blue line describes the Herwig++ result with POWHEG corrections, the dashed red line does not include matrix element corrections. The data are from Ref. [124] and the lower frame is as described in Fig. 3.6.

Fig. 3.7a 50 GeV $< M_{\gamma\gamma} <$ 80 GeV and in Fig. 3.7b 80 GeV $< M_{\gamma\gamma} <$ 350 GeV. For the same ranges of $M_{\gamma\gamma}$ we plot the azimuthal angle distribution between the photons in Fig. 3.8a and Fig. 3.8b respectively and the polar angle between the photons in Fig. 3.9a and Fig. 3.9b. For all distributions we see that the LO Herwig++ ditributions (red dashed line) do not correctly describe the data. The POWHEG approach improves the simulation and provides a good description of D0 data [125].

3.5 Conclusion

In the present Chapter the POWHEG NLO matching scheme has been extended and applied to $\gamma\gamma$-production in hadron collisions. The QED singularities are not treated by including fragmentation functions but rather by simulating the LO cross section for the corresponding process and then showering it. The simulation contains a full treatment of the truncated shower which is needed to correctly generate radiation with transverse momentum that is smaller than the one of the hardest emission.

The implementation of the process was tested by comparing the results with the fixed-order DIPHOX program which is in good agreement with the results of our approach for observables which are not sensitive to multiple QCD radiation.

We find that without a correction to describe the hard QCD radiation there is a deficit of radiation in the simulation. The POWHEG approach overcomes this problem and provides a good description of the data of Refs. [124, 125]. A remarkably good description is obtained for infrared sensitive observables, like the transverse momentum of the $\gamma\gamma$-pair at low $p_\perp^{\gamma\gamma}$, which demonstrates the resummation of logarithmic enhancement provided by the Herwig++ parton shower.

This is the first NLO simulation of a process involving photons and provides an important new tool for the study of promt photon production. The simulation will be made available in a forthcoming version of the Herwig++ simulation package.

Chapter 4

Implementing the POWHEG method for DIS in the **Herwig++** parton shower

There are three categories of scattering in particle physics: *elastic*, when only the momentum of the target and incident particle is changed, *inelastic*, which provides an excitation of the target particle in the final state, and *deep inelastic*, where the target is destroyed and new particles may be created.

During the 1960s inelastic scattering of leptons (electrons, muons and neutrinos) became a fundamental tool for the study of the nature of the internal structure of strongly interacting particles (hadrons). The basic philosophy behind these experiments was that the leptons, well-known nearly point-like particles, could be used to probe the structure of protons and neutrons, which were poorly understood at that time. The efficacy of the probe depends on the wavelength of the exchanged boson, $\lambda = \hbar/q$, where $\hbar$ is Plank's constant and q is the square root of the scale: the shorter the boson wavelength, the more detail the probe can resolve.

The first experiments with inelastic scattering were performed with beams of electrons of energy up to 16 GeV and a fixed target of protons; the work was led by a MIT-SLAC group at the Stanford Linear Accelerator Center [147–150]. We present some of their results in Fig. 4.1.

The cross sections, instead of being tiny and falling off rapidly as for the elastic electron-proton cross section, were found to be large with a dependence on the transferred momentum q^2, which is largely described by the Mott cross section, *i.e.* by scattering of pointlike spin $\frac{1}{2}$ particles. Fig. 4.1a shows the differential cross section, divided by the (Mott) cross section for point-like scattering, against q^2 for constant values of the invariant mass of the hadronic final state, $W = [(q + P)^2]^{1/2}$, where P is the momentum of the incoming hadron, and scattering angle of 10º.

Fig. 4.1b shows the energy spectrum of electrons of incident energy $E = 4.879$ GeV scattered at 10º from protons and final energy E'. We see the large elastic peak, which is shifted from 4.879 GeV by the recoil effect, and other peaks that correspond to the excitation of the recoil system. However, only the first peak beyond the elastic one, at $E' \approx 4.2$ GeV, corresponds to a well-known proton resonant state called Δ. In the other regions several excited states contribute to a "single" peak and the
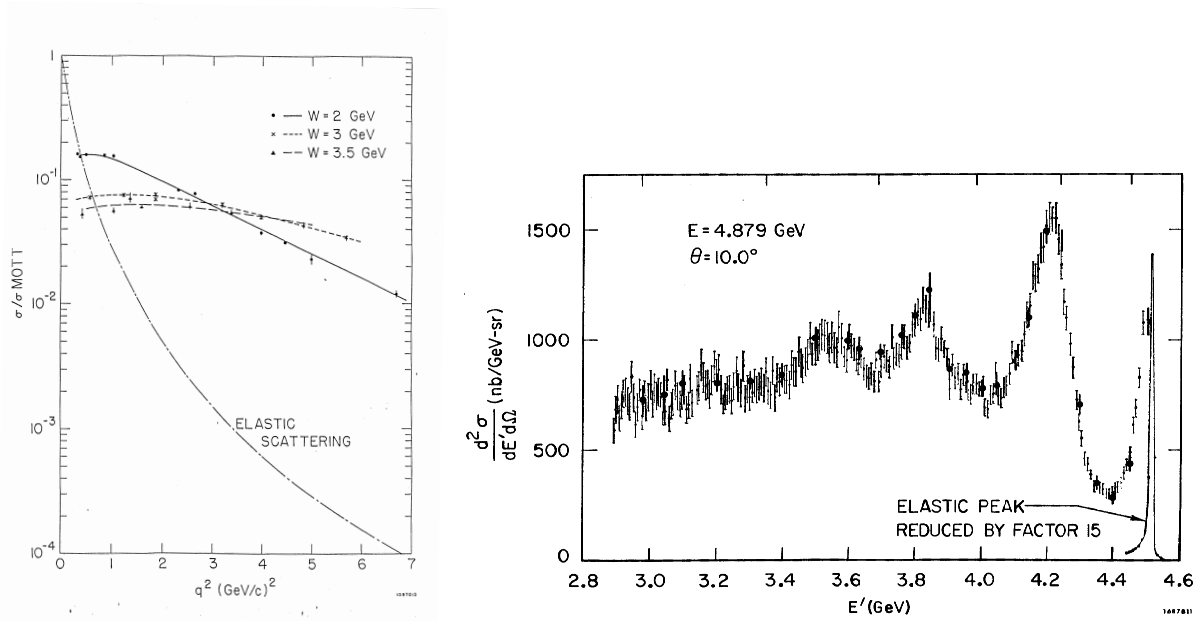
(a)   (b)

Figure 4.1: The pioneering experiments at SLAC showed that the DIS electron-proton cross section had a weak dependence on the transferred momentum, (a), Ref. [150]. In the right panel, (b), Ref. [149], we see resonance peaks due to excited states of the proton.

apparently featureless regions hide resonant states as well.

The complicated features of inelastic scattering were understood within the models proposed by Bjorken (cf. Ref. [151]) and Feynman (cf. Ref. [152]) who had respectively hypothesized the *scale invariance*[1] and *parton model* of hadrons. The former asserts that as $q^2 \to \infty$, $W^2 \to \infty$, the ratio W^2/q^2 is fixed, while the latter states that protons and neutrons are a collection of point-like constituents, partons, *i.e.* inelastic processes can be interpreted as the elastic scattering of the lepton with one of these constituents.

Over the last decades, with the availability of higher energy accelerators, more experiments have contributed to a better understanding of the structure of hadrons and the quark parton model has become the universally recognised picture describing the strong interaction.

The deep inelastic scattering process (DIS) has contributed a great deal in this direction and is now a well known process in the literature. There are two categories: one involves the exchange of a virtual photon or Z^0 boson and is referred to as *neutral current*, the other involves the exchange of a $W^\pm$ boson and is referred to as *charged current*. In *ep*-scattering at HERW, the former provides a final-state lepton, the latter a final-state neutrino.

Here we will focus on the neutral current, in particular electron-hadron and positron-hadron DIS. At leading order it is described by the Feynman diagrams shown in Fig. 4.2a, together with appropriate crossings of the quark line. As we mentioned in Chapter 2, the implementation of the POWHEG method for DIS in the

---

[1]In a private communication, Bjorken told the MIT-SLAC group about the scaling in 1968 [153].
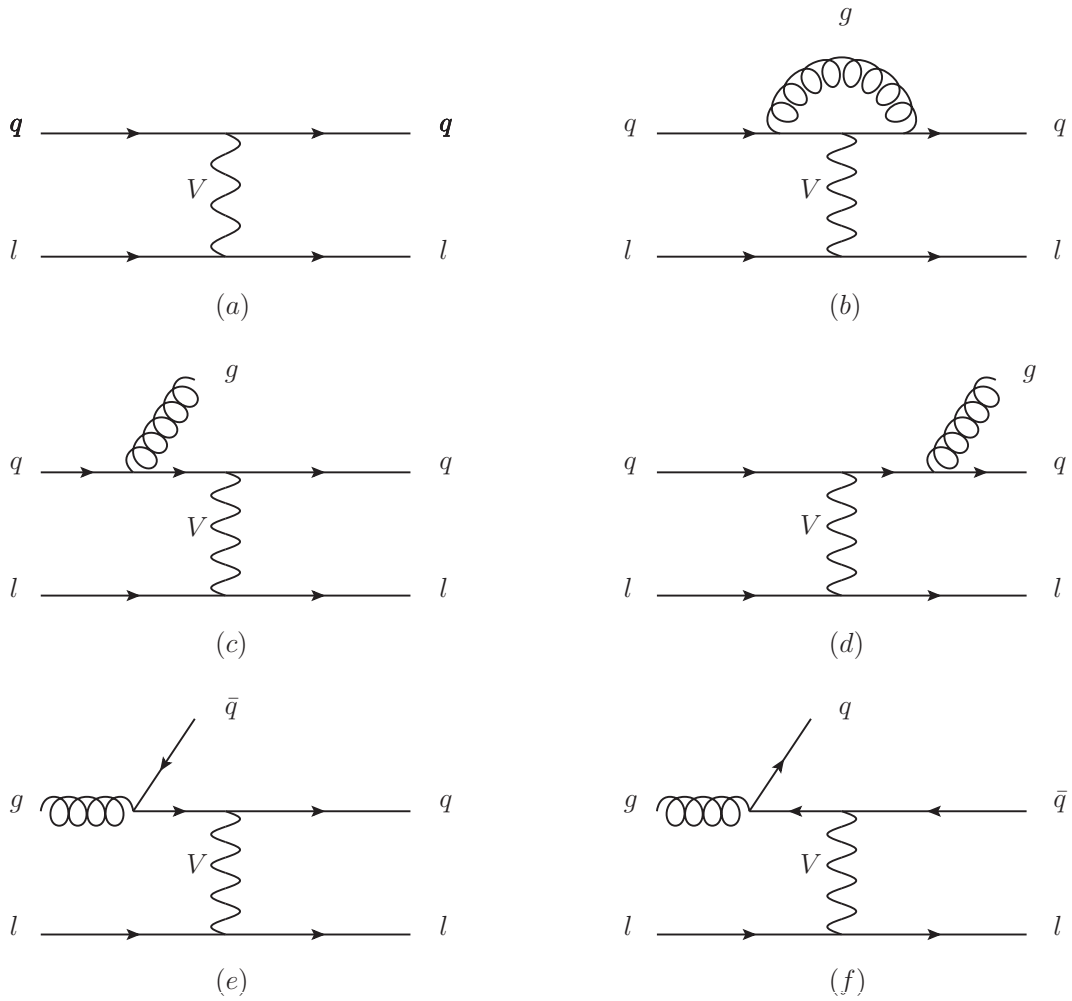
Figure 4.2: Feynman diagrams contributing to deep inelastic scattering at $\mathcal{O}(\alpha_s(\mu_R))$: leading order (a), virtual (b) and real emission (c-f) corrections. For simplicity, we show radiative corrections only to the upper line in the gluon emission (c-d) and gluon initiated processes (e-f).

Herwig++ parton shower strictly follows the one for VBF. However, the numerical integration is simplified by the simpler expression of the matrix element.

In this Chapter we will show the way I calculated and implemented the $\bar{B}(\Phi_B)$ for DIS [97]. The rest of the implementation is very similar to the VBF one, so we refer the reader to Chapter 2. Finally we present results in Sect. 4.2 and conclusions in Sect. 4.3.

4.1 Calculation of $\bar{B}(\Phi_B)$

The expression for the $\bar{B}(\Phi_B)$ function is given by

$$\bar{B}(\Phi_B) = B(\Phi_B) \left[1 + \frac{C_F \alpha_s(\mu_R)}{2\pi} \mathcal{V}(\Phi_B) \right.$$

$$\left. + \sum_{I \in \{\text{QCDC,BGF}\}} \frac{\mathcal{C}_I \alpha_s(\mu_R)}{2\pi} \int \left[\mathcal{A}_I(\Phi_B, \Phi_R) - \mathcal{D}_I(\Phi_B, \Phi_R) \right] \mathrm{d}\Phi_R \right], \quad (4.1)$$

where $B(\Phi_B)$ is the born, $\mathcal{V}(\Phi_B)$ is the virtual contribution of Eqn. 2.33 and $\mathcal{D}_I(\Phi_B, \Phi_R)$ are the dipoles in Eqns. 2.22a-2.22b. The only difference to the VBF case is due to the real corrections. The real emission contribution to $\bar{B}$ is given by Eqn. 2.23. However, in the DIS case the leading-order matrix elements are simple enough that $R_{2,3}$ (see Eqns. 2.19c-2.19d) can be calculated analytically and integrated over the azimuthal angle, ϕ and z_p to simplify the numerical integration of $\bar{B}$.

For DIS [44, 47],

$$R_2 = \frac{\cos^2 \theta_2 + \mathcal{A} \cos \theta_2 \left(\ell - \sqrt{\ell^2 - 1} \sin \theta_2 \cos \phi \right) + \left(\ell - \sqrt{\ell^2 - 1} \sin \theta_2 \cos \phi \right)^2}{1 + \mathcal{A}\ell + \ell^2},$$
$$(4.2)$$

where $\cos \theta_2 = \frac{x_2}{\sqrt{x_2^2 + x_\perp^2}}$, $\sin \theta_3 = \frac{x_\perp}{\sqrt{x_2^2 + x_\perp^2}}$, $\ell = \frac{2}{y_B} - 1$, $y_B = \frac{q \cdot q_1}{p_\ell \cdot q_1}$ and p_ℓ is the four-momentum of the incoming lepton. $\mathcal{A}$ is related to the couplings of the fermions to the exchanged vector bosons. For the charged current process $\mathcal{A} = 2$, whereas for the neutral current process

$$\mathcal{A} = \frac{4r C_{A,\ell} C_{A,q} \left(Q_\ell Q_q + 2r C_{V,\ell} C_{V,q} \right)}{\left(Q_\ell^2 Q_q^2 + 2Q_\ell Q_q r C_{V,\ell} C_{V,q} + r^2 \left(C_{V,\ell}^2 + C_{A,\ell}^2 \right) \left(C_{V,q}^2 + C_{A,q}^2 \right) \right)}, \quad (4.3)$$

with $r = \frac{Q^2}{(Q^2 + m_Z^2)}$ and

$$C_{V,i} = \frac{1}{\sin \theta_W \cos \theta_W} \left(\frac{I_{3,i}}{2} - Q_i \sin^2 \theta_W \right), \quad (4.4\text{a})$$

$$C_{A,i} = \frac{1}{\sin \theta_W \cos \theta_W} \frac{I_{3,i}}{2}, \quad (4.4\text{b})$$

where m_Z is the Z^0 boson mass, θ_W the Weinberg angle, Q_i the fermion charge and $T_{3,i}$ its weak isospin.

The expression for R_3 can be obtained from that for R_2 with the substitution $A \to -\mathcal{A}$, $\theta_2 \to \theta_3$ and $\phi \to \pi - \phi$.

In this case the contribution to $\bar{B}$ is

$$B(\Phi_B) \mathrm{d}\Phi_B \mathrm{d}x_p \sum_{I \in \{\text{QCDC,BGF}\}} \frac{\alpha_S}{2\pi} S_I, \quad (4.5)$$

where

$$S_{\text{QCDC}} = \frac{\frac{x_B}{x_p} f_q\left(\frac{x_B}{x_p}, Q^2\right)}{x_B f_q(x_B, Q^2)} \frac{2 + 2\ell^2 - x_p + 3x_p\ell^2 + \mathcal{A}\ell\left(1 + 2x_p\right)}{1 + \mathcal{A}\ell + \ell^2}, \tag{4.6a}$$

$$S_{\text{BGF}} = -\frac{\frac{x_B}{x_p} f_q\left(\frac{x_B}{x_p}, Q^2\right)}{x_B f_q(x_B, Q^2)} \frac{1 + \ell^2 + 2\left(1 - 3\ell^2\right) x_p(1 - x_p) + 2\mathcal{A}\ell\left(1 - 2x_p(1 - x_p)\right)}{1 + \mathcal{A}\ell + \ell^2}. \tag{4.6b}$$

4.2 Results

At this stage the POWHEG matching for DIS proceeds identically to the VBF case; the NLO phase-space is built up as described in Sect. 2.1.2, $\bar{B}$ is sampled as described in Sect. 2.1.4 and the shower algorithm, hardest emission, truncated and vetoed showers follow as in sects. 3.3-2.3. For this reason we proceed directly to the results.

In order to test our implementation of the POWHEG approach for deep inelastic scattering we first compared the results from Herwig++ and DISENT [156] for the reduced cross section

$$\tilde{\sigma} = \frac{xQ^4}{2\pi\alpha^2 Y_+} \frac{\mathrm{d}^2\sigma}{\mathrm{d}x\mathrm{d}Q^2}, \tag{4.7}$$

where $y = \frac{Q^2}{xs}$, $Y_\pm \equiv 1 \pm (1 - y)^2$ and α is the fine-structure constant. The difference between the Herwig++ and DISENT results divided by the sum of the results is shown as a dashed line in the lower panels in Figs. 4.3 and 4.4. However, the dashed line is not visible because this difference is always less than one per mille. In addition Fig. 4.3 shows the comparison of the Herwig++ result with the results from Ref. [154] and Fig. 4.4 shows the comparison of the Herwig++ result with the results from Refs. [154] and [155]. The excellent agreement with DISENT and the experimental data demonstrates that the generation of the Born variables and calculation of $\bar{B}$ is correct. In both cases the PDFs from Ref. [157] were used.

In order to study the real emission we compare the results of Herwig++ with the measurements of the transverse energy flow in DIS from Ref. [158], which are sensitive to the treatment of hard radiation in angular ordered parton showers [44]. The cross section for the transverse energy flow, $\frac{1}{N} \frac{\mathrm{d}E_T^*}{\mathrm{d}\eta^*}$, is given as a function of pseudorapidity, η^*. Here the superscript * is used for the quantities in the hadronic centre of mass system and N is the total number of DIS events. Comparisons of Herwig++ with the low and high Q^2 samples from Ref. [158] are shown in Figs. 4.5 and 4.6, respectively. In addition to the Herwig++ result, with and without the POWHEG correction, we have included the result of the FORTRAN HERWIG [27,42] and Herwig++ with a matrix element correction based on the approach of Ref. [44]. These results clearly show that without a correction to describe hard QCD radiation there is a deficit of emissions between $1 < \eta^* < 3$, which is remedied by using either the POWHEG approach or a traditional matrix element correction. In general the POWHEG approach gives slightly less radiation than the matrix element due to the Sudakov suppression of radiation, which is neglected in the matrix element correction approach and is in the best agreement with the experimental results. In these plots
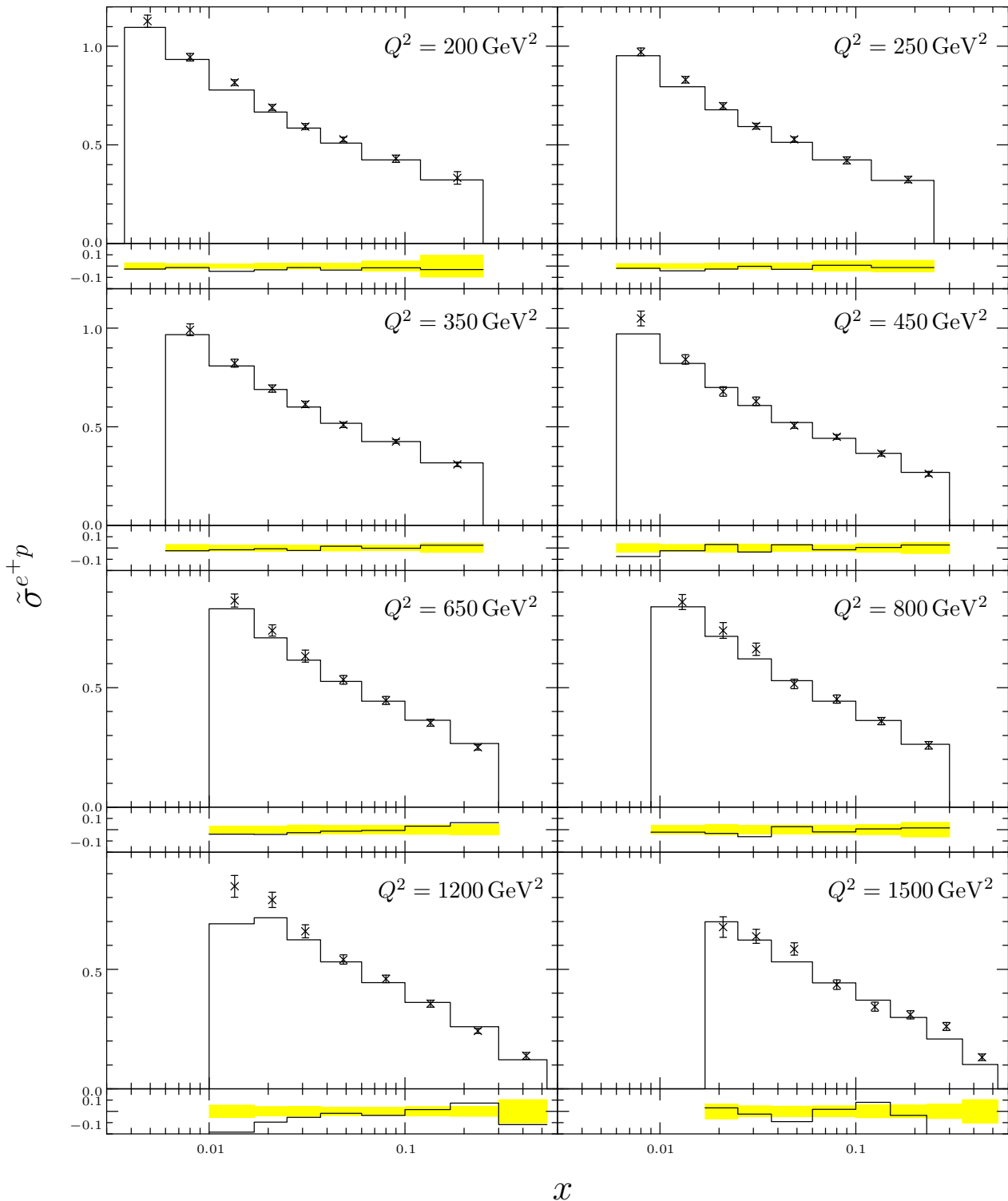
Figure 4.3: The e^+p reduced cross section $\tilde{\sigma}^{e^+p}$, as a function of x at fixed Q^2 between $200\,\mathrm{GeV}^2$ and $1500\,\mathrm{GeV}^2$. The experimental results of Ref. [154] are shown as crosses. The lower frame shows $(\mathrm{Data} - \mathrm{Theory})/\mathrm{Data}$ and the yellow band gives the one sigma error. The solid (black) line shows the Herwig++ result.
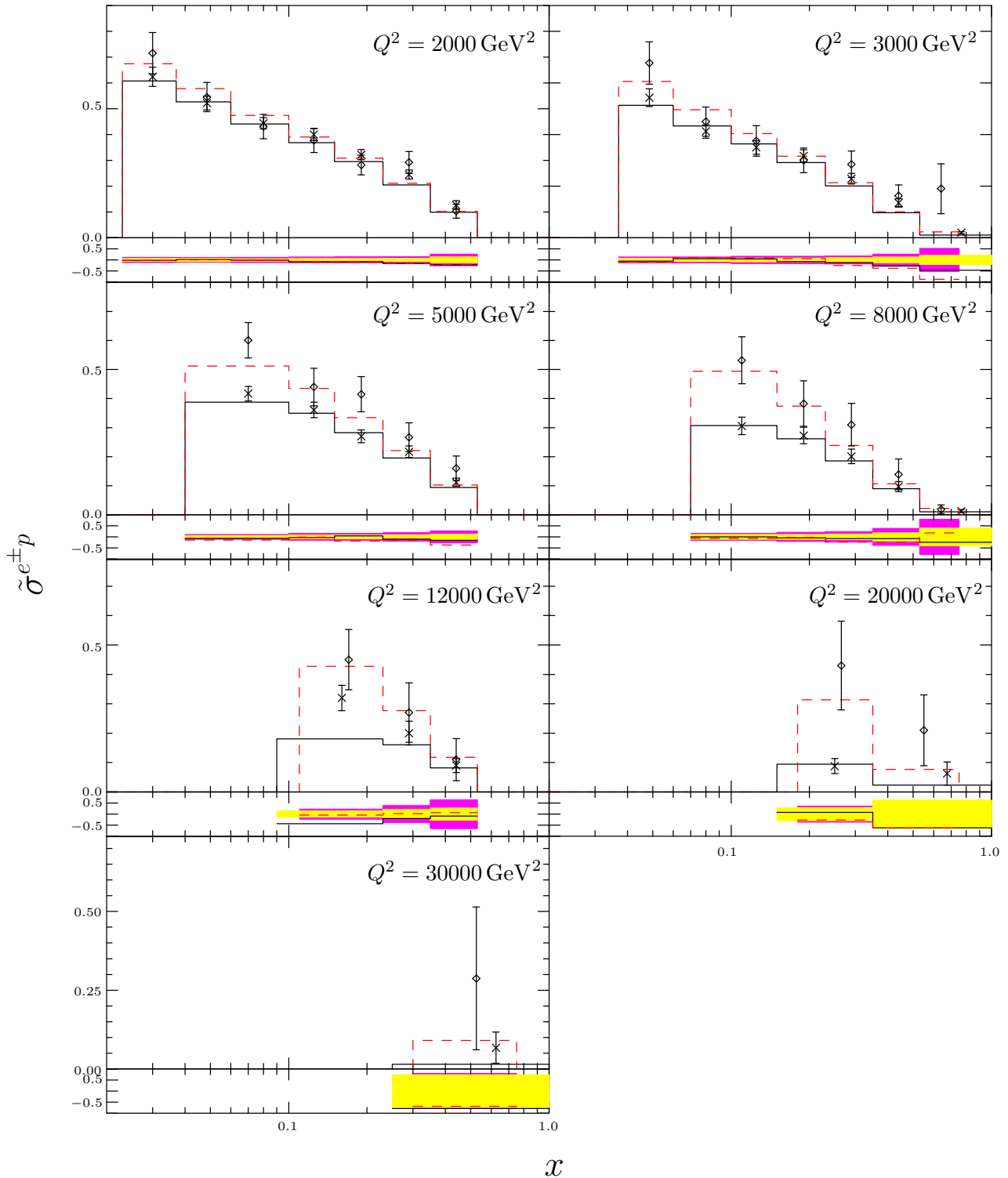
Figure 4.4: The $e^{\pm}p$ reduced cross section $\tilde{\sigma}^{e^{\pm}p}$, as a function of x at fixed Q^2 between $200\,\mathrm{GeV}^2$ and $1500\,\mathrm{GeV}^2$. The experimental results of Ref. [154] for $\tilde{\sigma}^{e^+p}$ are shown as crosses and the results of Ref. [155] for $\tilde{\sigma}^{e^-p}$ as diamonds. The lower frame shows $(\mathrm{Data}-\mathrm{Theory})/\mathrm{Data}$ and the inner (yellow) band gives the one sigma error for $\tilde{\sigma}^{e^+p}$ and the outer (magenta) band the one sigma error for $\tilde{\sigma}^{e^-p}$. The solid (black) line shows the Herwig++ result for $\tilde{\sigma}^{e^+p}$ and the dashed (red) line shows the Herwig++ result for $\tilde{\sigma}^{e^-p}$.
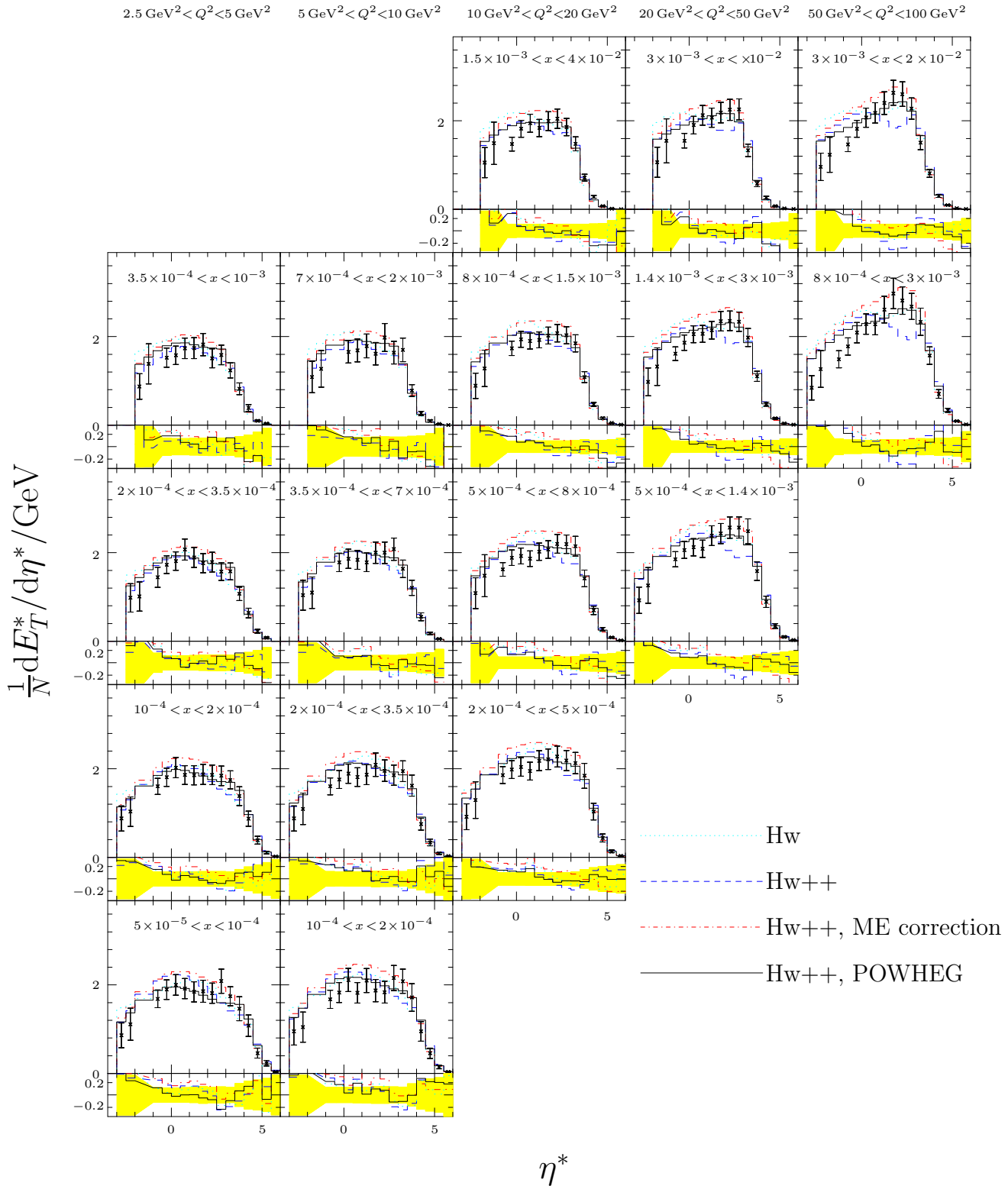
Figure 4.5: The inclusive transverse energy flow $\frac{1}{N}\mathrm{d}E_T^*/\mathrm{d}\eta^*$ at different values of x and Q^2 for the low Q^2 sample from [158]. The lower frame shows $(\mathrm{Data} - \mathrm{Theory})/\mathrm{Data}$ and the yellow band gives the one sigma error.
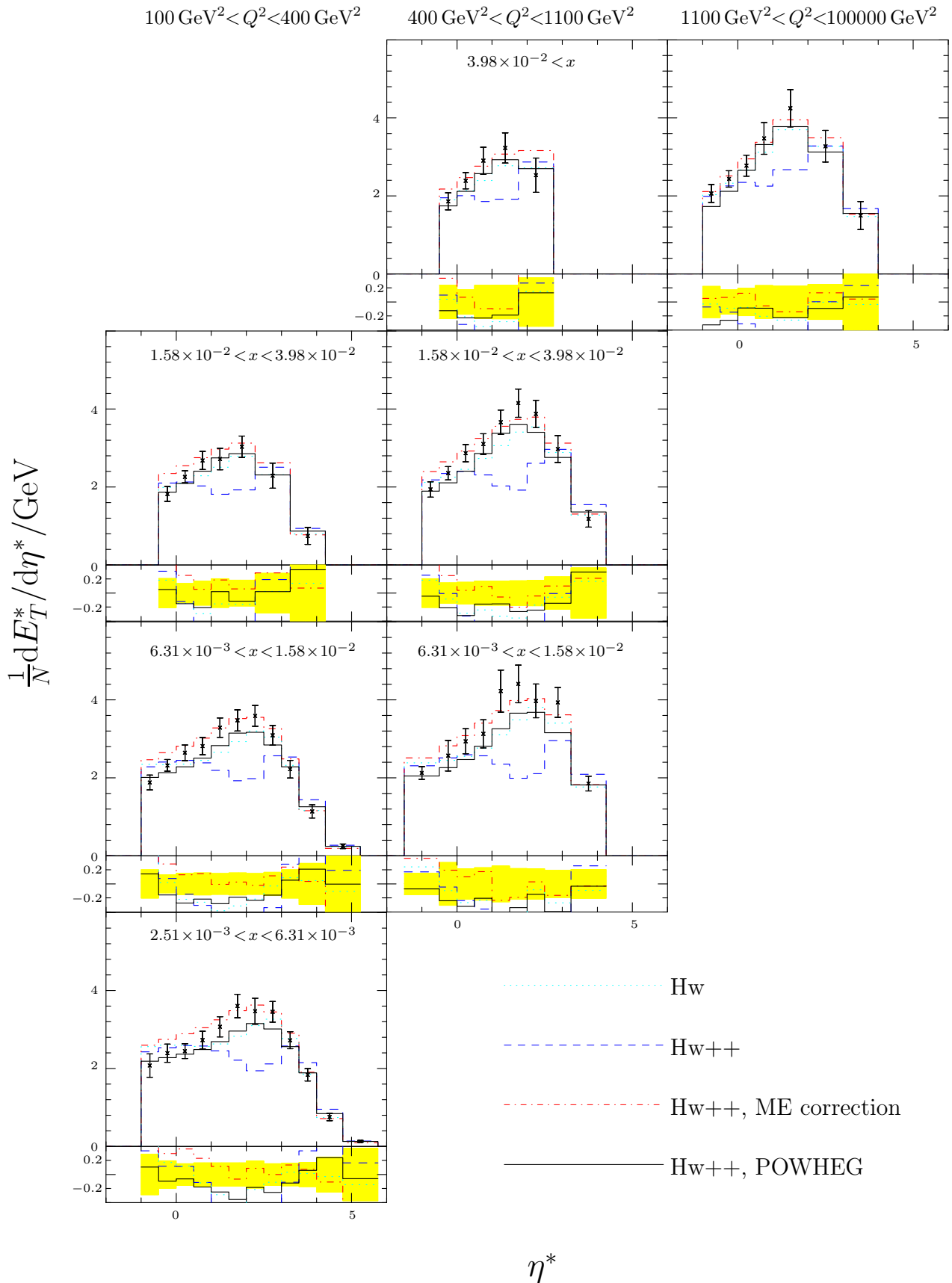
Figure 4.6: The inclusive transverse energy flow $\frac{1}{N}\mathrm{d}E_T^*/\mathrm{d}\eta^*$ at different values of x and Q^2 for the high Q^2 sample from [158]. The lower frame shows (Data $-$ Theory)/Data and the yellow band gives the one sigma error.

we have tuned the mass parameter for the splitting of the soft beam remnant cluster in Herwig++ to 0.5 GeV from the HERWIG value of 1 GeV. The transverse energy flow in DIS is most sensitive to this parameter and the original HERWIG value was tuned to older transverse energy flow data.

4.3 Conclusions

In the present Chapter the POWHEG formalism has been applied to the Herwig++ parton shower for the DIS process. As discussed in Sect. 2.1, some of the Feynman diagrams contributing to the VBF process are negligible in the phase-space regions where VBF can be observed experimentally. This results in similar NLO corrections for both DIS and VBF, provided that in the latter process we take into account the corrections to upper and lower quark lines. This allows for the application of the same approach for both processes.

The calculation and implementation of $\bar{B}$ have been checked by comparing the reduced cross section from Herwig++ and DISENT, and we find excellent agreement between the two distributions. In addition, we find the cross sections to be in good agreement with the experimental results of Refs. [154, 155, 158]. Our results show that the POWHEG approach correctly populates the so-called *dead zone*, as it appears in the transverse energy flow distributions at high Q^2.

Chapter 5

Implementing the POWHEG method for DIS in **Matchbox**

The DIS is a simple and very well known process in the literature, but it provides an important test bed for the initial-final and final-initial radiation of the dipole shower. In Chapter 4 we discussed the importance of DIS for the study of hadron structure before showing the way I implemented the POWHEG method for this process in the **Herwig++** parton shower; particular emphasis was put on the calculation of $\bar{B}(\Phi_B)$, the generation of the hardest emission and the reorganization of the shower into truncated and vetoed shower.

Now we focus on the POWHEG implementation for DIS into the shower of Ref. [4]. As we highlighted in Sect. 1.6.5, the dipole shower is p_T ordered and does not need to be rearranged: the hardest p_T emission is simply the first one and there is no need to interrupt the branching simulation. Moreover, **Matchbox** is based on a general design that provides $\bar{B}(\Phi_B)$ in an automatic way and implements it for $e^+e^- \to$ hadrons, Drell-Yan and DIS processes, by the crossing of the $\mathcal{M}_{(\mathcal{O} \to q(p_1) + \bar{q}(p_2) + l(p_3) + \bar{l}(p_4))}$ matrix element, where q $(\bar{q})$ identifies a quark (antiquark) and l $(\bar{l})$ a lepton (antilepton) of a given flavour. The POWHEG approach for DIS in the dipole shower has been completed by my implementation of the NLO phase-space. In particular, the latter is required to be independent from the LO implementation and to present the transferred momentum, Q^2, as one of the degrees of freedom. For these reasons the phase-space algorithm of Sect. 2.1.2 cannot be used even though the Breit frame is still the simplest choice.

In this Chapter we will show how I implemented the NLO phase-space into the dipole shower for DIS in Sect. 5.1, and the results will be given in Sect. 5.2. We will present our conclusions in Sect. 5.3.

5.1   NLO phase-space

The next-to-leading order cross section for the DIS process is[1] (cf. Eqn. 1.6)

$$d\sigma_{NLO} = \frac{d\Phi_3}{2\hat{s}} dx f(x, Q^2) \overline{\sum} |\mathcal{M}(k_1 p_1 \to k_2 p_2 p_3)|^2, \qquad (5.1)$$

---

[1]The convention for the momenta follows the one chosen in Fig. 5.1.

where $\bar{\sum}$ denotes the sum over the final-state quantum numbers for each contributing channel and the average over the initial-state quantum numbers. The function $f(x, Q^2)$ is the PDF, which depends on the momentum fraction of the incoming parton, x, and the scale, Q^2. As mentioned before, Matchbox provides an automated way to calculate $\sum |\mathcal{M}(k_1 p_1 \to k_2 p_2 p_3)|^2$ and the PDF. The remaining contribution is

$$\mathrm{d}\Phi_{NLO} = \frac{\mathrm{d}\Phi_3}{2\hat{s}} \equiv \mathcal{W}_{NLO} \mathrm{d}\tilde{\Phi}_{NLO}, \qquad (5.2)$$

which consists of the phase-space weight, $\mathcal{W}_{NLO}$, and the phase-space variables defined on the unit cube, $\mathrm{d}\tilde{\Phi}_{NLO}$. Moreover, the phase-space is expected to provide the outgoing momenta in the centre of mass frame of the incoming particles.

In this section we describe in detail how these quantities are calculated and show the way the DIS NLO phase-space works within Matchbox. The implementation proceeds schematically in the following way:

- calculate the NLO phase-space measure;

- parametrise the variables in terms of the unit cube;

- map the phase-space to flatten the integrand in the singular domain;

- generate the outgoing momenta in the centre of mass frame of the incoming particles.

In the following we will give more details about each of these items.

5.1.1   The measure

We want to calculate the phase-space measure for massless quarks and leptons with mass m_l. The phase-space for the $e(k_1) + q(p_1) \to e(k_2) + q(p_2) + g(p_3)$ scattering[2], shown in Fig. 5.1, is given by (cf. Eqns. 1.6-1.7)

$$\mathrm{d}\Phi_{NLO} = \frac{(2\pi)^4}{2\hat{s}} \frac{\mathrm{d}^3 k_2}{(2\pi)^3 2 E_{k_2}} \frac{\mathrm{d}^3 p_2}{(2\pi)^3 2 E_{p_2}} \frac{\mathrm{d}^3 p_3}{(2\pi)^3 2 E_{p_3}} \delta^4(k_1 + p_1 - k_2 - p_2 - p_3). \quad (5.3)$$

Choosing $p_x = p_2 + p_3$, *i.e.* using

$$\int \mathrm{d}^4 p_x \delta^4(p_x - p_2 - p_3), \qquad (5.4)$$

we change our problem into a simpler $2 \to 2$ scattering and can thus split the phase-space measure into hadronic and leptonic contributions.

The leptonic part is studied by considering the scattering $p_1 + k_1 \to p_x + k_2$ and rewritten as

$$\begin{aligned} \mathrm{d}\Phi^l_{NLO} &= \frac{(2\pi)^4}{2\hat{s}} \frac{\mathrm{d}^3 k_2}{(2\pi)^3 2 E_{k_2}} \frac{\mathrm{d}^3 p_x}{(2\pi)^3 2 E_{p_x}} \delta^4(k_1 + p_1 - k_2 - p_x) \\ &= \frac{1}{32\pi} \frac{1}{|\vec{k}_1| \hat{s}^{3/2}} \frac{\mathrm{d}\phi_l}{2\pi} \mathrm{d}Q^2. \end{aligned} \qquad (5.5)$$

---

[2]This is just one of the channels contributing to DIS at NLO. The discussion of the phase-space would proceed in a similar way if we considered the $eg \to eq\bar{q}$ or any other process obtained by crossing.
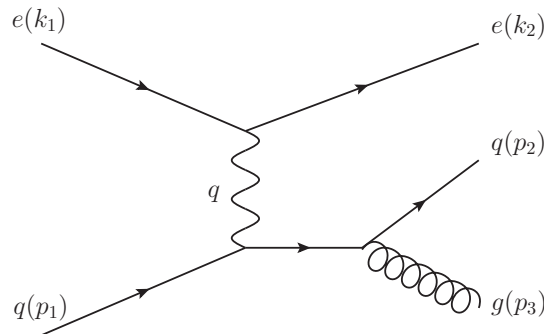
Figure 5.1: Electron-quark scattering at NLO.

Here the last line follows from energy conservation and the definition

$$Q^2 = -(k_1 - k_2)^2, \qquad (5.6)$$

and ϕ_l is the azimuthal angle of the outgoing lepton around the incoming direction.

The hadronic contribution is studied in the Breit frame by considering the process $p_1 + q \rightarrow p_2 + p_3$ and rewritten as

$$\mathrm{d}\Phi^h_{NLO} = (2\pi)^3 \mathrm{d}m_x^2 \prod_{i=2}^{3} \frac{\mathrm{d}^3 p_i}{(2\pi)^3 2E_{p_i}} \delta^4(p_x - p_3 - p_2)$$
$$= \frac{1}{16\pi^2} \frac{\mathrm{d}\phi_h}{2\pi} \frac{\mathrm{d}x_1}{x_1} \mathrm{d}x_2 Q^2, \qquad (5.7)$$

where the result follows from energy-momentum conservation of the momenta defined in Eqns. 2.2a-2.2c and the definition of x_i in Eqn. 2.3. The hadronic azimuthal angle around the incoming direction is ϕ_h.

From Eqns. 5.5 and 5.7 we obtain

$$\mathrm{d}\Phi_{NLO} \equiv \mathrm{d}\Phi^h_{NLO} \mathrm{d}\Phi^l_{NLO} = -\frac{1}{64(2\pi)^3} \frac{Q^2}{|\vec{k}_1|\hat{s}^{3/2}} \mathrm{d}Q^2 \frac{\mathrm{d}\phi_l}{2\pi} \frac{\mathrm{d}\phi_h}{2\pi} \frac{\mathrm{d}x_1}{x_1} \mathrm{d}x_2, \qquad (5.8)$$

which gives the phase-space measure of Ref. [48] in the massless case. Eqn. 5.8 gives the phase-space weight in the variables $\{Q^2, \phi_l, \phi_h, x_1, x_2\}$.

5.1.2 The unit cube

As we discussed in Sect. 2.1.4, for convenience the phase-space variables are transformed into a new set defined on the unit cube.

The element $\mathrm{d}Q^2$ integrates the photon propagator ($\propto 1/Q^2$), which diverges in the limit $Q^2 \rightarrow 0$. The mapping of the phase-space needs to be denser in the region where the integrand function has a high gradient and this would require more time for the numerical integration. In order to provide an efficient integration we consider a Jacobian transformation that both flatten the integrand function and change Q^2

into $\tilde{Q}^2$, where $\tilde{Q}^2$ is defined in $[0, 1]$. This is performed in the following way

$$\int_{Q^2_{\min}}^{Q^2_{\max}} \frac{1}{Q^2} \mathrm{d}Q^2$$

$$= \left[\ln Q^2_{\max} - \ln Q^2_{\min}\right] \int_0^1 \mathrm{d}\tilde{Q}^2, \tag{5.9}$$

where

$$\left| J\left(\frac{\partial Q^2}{\partial \tilde{Q}^2}\right) \right| \mathrm{d}\tilde{Q}^2 = Q^2(\tilde{Q}^2) \left[\ln Q^2_{\max} - \ln Q^2_{\min}\right] \mathrm{d}\tilde{Q}^2 \tag{5.10}$$

$$Q^2(\tilde{Q}^2) = e^{\left[\left(\ln Q^2_{\max} - \ln Q^2_{\min}\right)\tilde{Q}^2 + \ln Q^2_{\min}\right]}. \tag{5.11}$$

We typically set $Q^2_{\min} = 2 \text{ GeV}^2$ and $Q^2_{\max} = \hat{s}$.

The azimuthal angles can be easily parametrised on the unit cube as:

$$\mathrm{d}\tilde{\phi}_l = \frac{\mathrm{d}\phi_l}{2\pi}, \qquad\qquad \mathrm{d}\tilde{\phi}_h = \frac{\mathrm{d}\phi_h}{2\pi}. \tag{5.12}$$

Finally the variable (x_1, x_2) can be changed into the (x_p, z_p) defined in Eqns. 2.8a-2.8b as

$$\left| J\left(\frac{\partial^2(x_1, x_2)}{\partial x_p \partial z_p}\right) \right| \mathrm{d}x_p \mathrm{d}z_p = \frac{1}{x_p^3} \mathrm{d}x_p \mathrm{d}z_p. \tag{5.13}$$

5.1.3   Mapping

Here again the integrand function shows a high gradient towards the singularities in (x_p, z_p) and for efficiency reasons we flatten the integrand in the singular domain. The divergences are given by $\sim \frac{1}{(1-x_p)(1-z_p)}$ for the quark initiated process (cf. Eqn. 2.10) and $\sim \frac{1}{z_p(1-z_p)}$ for the gluon initiated one (cf. Eqn. 2.16). Therefore we need a new set of variables $(\bar{x}_p, \bar{z}_p)$ such that

$$\frac{\mathrm{d}z_p}{\mathrm{d}\bar{z}_p}\mathrm{d}\bar{z}_p = [z_p(\bar{z}_p) + \epsilon][1 - z_p(\bar{z}_p) + \epsilon]\mathrm{d}\bar{z}_p, \tag{5.14a}$$

$$\frac{\mathrm{d}x_p}{\mathrm{d}\bar{x}_p}\mathrm{d}\bar{x}_p = [1 - x_p(\bar{x}_p) + \epsilon]\mathrm{d}\bar{x}_p, \tag{5.14b}$$

which gives

$$\bar{z}_p = \frac{1}{1 + 2\epsilon}\ln\left[\frac{z_p + \epsilon}{1 - z_p + \epsilon}\right], \tag{5.15a}$$

$$\bar{x}_p = -\ln[1 - x_p + \epsilon] \tag{5.15b}$$

and the Jacobian

$$\left| J\left(\frac{\partial^2(x_p, z_p)}{\partial \bar{x}_p \partial \bar{z}_p}\right) \right| \mathrm{d}\bar{x}_p \mathrm{d}\bar{z}_p = [z_p(\bar{z}_p) + \epsilon][1 - z_p(\bar{z}_p) + \epsilon][1 - x_p(\bar{x}_p) + \epsilon]\mathrm{d}\bar{x}_p \mathrm{d}\bar{z}_p. \tag{5.16}$$

Here we choose $\epsilon = 0.01$ to guarantee that the variables $(\bar{x}_p, \bar{z}_p)$ are finite everywhere in their domain, i.e. $\bar{x}_p^{\min} \leq \bar{x}_p \leq \bar{x}_p^{\max}$ and $\bar{z}_p^{\min} \leq \bar{z}_p \leq \bar{z}_p^{\max}$ with

$$\bar{x}_p^{\min} = -\ln[1 - x_B + \epsilon], \qquad\qquad \bar{x}_p^{\max} = -\ln[\epsilon], \qquad\qquad (5.17a)$$

$$\bar{z}_p^{\min} = \frac{1}{1 + 2\epsilon}\ln\left[\frac{\epsilon}{1 + \epsilon}\right], \qquad\qquad \bar{z}_p^{\max} = \frac{1}{1 + 2\epsilon}\ln\left[\frac{1 + \epsilon}{\epsilon}\right]. \qquad (5.17b)$$

The variables $(\bar{x}_p, \bar{z}_p)$ are not defined on the unit cube and we need a further Jacobian transformation for that. We choose

$$\tilde{x}_p = \frac{\bar{x}_p - \bar{x}_p^{\min}}{\bar{x}_p^{\max} - \bar{x}_p^{\min}}, \qquad\qquad (5.18a)$$

$$\tilde{z}_p = \frac{\bar{z}_p - \bar{z}_p^{\min}}{\bar{z}_p^{\max} - \bar{z}_p^{\min}}, \qquad\qquad (5.18b)$$

with Jacobian

$$\left| J\left(\frac{\partial^2(\bar{x}_p, \bar{z}_p)}{\partial\tilde{x}_p\partial\tilde{z}_p}\right) \right| \mathrm{d}\tilde{x}_p\mathrm{d}\tilde{z}_p = [\bar{x}_p^{\max} - \bar{x}_p^{\min}][\bar{z}_p^{\max} - \bar{z}_p^{\min}]\mathrm{d}\tilde{x}_p\mathrm{d}\tilde{z}_p. \qquad (5.19)$$

5.1.4 Outgoing momenta

At this stage we have all the ingredients needed to calculate the NLO outgoing momenta. The lepton momentum is calculated in the centre of mass frame and has the following form:

$$k_2 = (\sqrt{|\vec{k}_2|^2 + m_l^2}; |\vec{k}_2|\cos\theta_l\sin\phi_l, |\vec{k}_2|\sin\theta_l\sin\phi_l, |\vec{k}_2|\sin\theta_l), \qquad (5.20)$$

where the polar angle is known from Eqn. 5.6, $|\vec{k}_2|$ is the modulus of the lepton trimomentum and in the centre of mass frame it is

$$|\vec{k}_2| = \left[\frac{(\hat{s} + m_l^2 - p_x^2)^2}{4\hat{s}} - m_l^2\right]^{1/2}. \qquad (5.21)$$

The parton momenta p_2 and p_3 are calculated in the Breit frame according to Eqns. 2.2b-2.2c. Now we need to boost these momenta into the centre of mass frame. The same result is obtained if we boost $p_2 + p_3$ so that $p_x \rightarrow (E_x'; -\vec{k}_2)$. To this end, we first translate p_x along the z-axis; i.e.

$$\begin{pmatrix} \sqrt{\hat{s}} - E_{k_2} \\ -k_2^x \\ -k_2^y \\ -k_2^z \end{pmatrix} = \begin{pmatrix} \gamma_z & 0 & 0 & -\beta_z\gamma_z \\ 0 & 1 & 0 & 0 \\ 0 & 0 & 1 & 0 \\ -\beta_z\gamma_z & 0 & 0 & \gamma_z \end{pmatrix} \begin{pmatrix} E_x \\ 0 \\ 0 \\ p_x^z \end{pmatrix}, \qquad (5.22)$$

which gives

$$\beta_z = \frac{p_x^z E_x + |\vec{k}_2|(\sqrt{\hat{s}} - E_{k_2})}{(\sqrt{\hat{s}} - E_{k_2})^2}. \qquad (5.23)$$

We then need to rotate p_x around the x-axis by θ_l and ϕ_l around the z-axis. This gives the requested expression for p_x. Therefore we apply the same roto-translation to p_2 and p_3 separately.

5.1.5 The NLO phase-space algorithm

Once the phase-space weight has been calculated we need a recipe in order to implement it into a code. The phase-space algorithm works in the following way:

- generate flat distributed random numbers between 0 and 1, $\tilde{\Phi}_{NLO} = \left\{ \tilde{Q}^2, \tilde{\phi}_l, \tilde{\phi}_h, \tilde{x}_p, \tilde{z}_p \right\}$;

- compute the momentum of the outgoing lepton in the centre of mass frame;

- calculate the parton momenta in the Breit frame, Eqns. 2.2b-2.2c;

- boost the parton momenta to the centre of mass frame;

- compute the weight:

$$\mathcal{W}_{NLO} = \left| J \left(\frac{\partial^2 (x_1, x_2)}{\partial x_p \partial z_p} \right) \right| \left| J \left(\frac{\partial^2 (x_p, z_p)}{\partial \tilde{x}_p \partial \tilde{z}_p} \right) \right| \left| J \left(\frac{\partial Q^2}{\partial \tilde{Q}^2} \right) \right|$$
$$\times \frac{1}{x_1(\tilde{x}_p)} \frac{1}{64(2\pi)^3} \frac{Q^2(\tilde{Q}^2)}{|\vec{k}_1| \hat{s}^{3/2}}. \tag{5.24}$$

5.2 Results

In order to test the implementation of the phase-space, we first compare results of the NLO cross section for Matchbox and Herwig++. For the following set of cuts

$$Q^2 > 20 \text{ GeV}^2, \tag{5.25}$$
$$W^2 > 100 \text{ GeV}^2, \tag{5.26}$$

we compare the p_T and rapidity distribution of the outgoing lepton, as shown in Fig. 5.2. The distributions are normalised to one. The p_T curve has a peak around 5 GeV and is 0.28 $\frac{1}{\text{GeV}}$ high. The rapidity distribution has a peak around 2 and 1.4 high. The distribution is not symmetric respect to zero as expected in lepton-proton scattering (cf. rapidity distribution for hadron-hadron scattering in Fig. 2.4). For both observables there is a tiny mismatch of the cross section between Herwig++ and Matchbox.

To check whether the mismatch is coming from the implementation of the NLO phase-space, we use two equivalent sets of dipoles and check the integration over the phase-space. For the quark initiated process, we introduce suitable dipoles, that we call "new dipoles" (ND), and write in terms of the Catani-Seymour dipoles, that we label with the subscript "standard dipoles" (SD), in the following way:

$$D_{\text{ND}}^{\text{FI}} = D_{\text{SD}}^{\text{FI}} + (1 - x)(1 + 3xz), \tag{5.27}$$
$$D_{\text{ND}}^{\text{IF}} = D_{\text{SD}}^{\text{FI}} + u(1 + 3\tilde{x}(1 - u)), \tag{5.28}$$
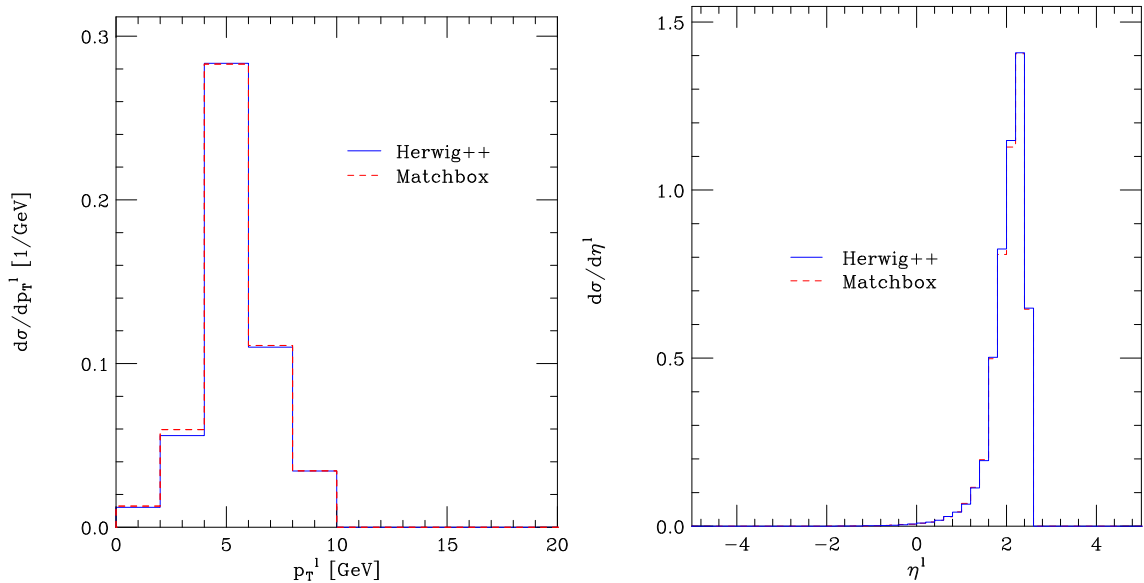
Figure 5.2: NLO cross section comparison between Herwig++ (solid blue line) and Matchbox (dashed red line). We plot the p_T (left panel) and rapidity (right panel) distribution of the outgoing electron. In both cases we observe a tiny mismatch.

where

$$x = \frac{p_{\text{emitt}}p_{\text{spect}} + p_{\text{emiss}}p_{\text{spect}} - p_{\text{emitt}}p_{\text{emiss}}}{(p_{\text{emitt}} + p_{\text{emiss}})p_{\text{spect}}}, \tag{5.29}$$

$$z = \frac{p_{\text{emitt}}p_{\text{spect}}}{(p_{\text{emitt}} + p_{\text{emiss}})p_{\text{spect}}}, \tag{5.30}$$

$$\tilde{x} = \frac{p_{\text{spect}}p_{\text{emitt}} + p_{\text{emiss}}p_{\text{emitt}} - p_{\text{emiss}}p_{\text{spect}}}{(p_{\text{emitt}} + p_{\text{emiss}})p_{\text{spect}}}, \tag{5.31}$$

$$u = \frac{p_{\text{emitt}}p_{\text{emiss}}}{(p_{\text{emitt}} + p_{\text{emiss}})p_{\text{spect}}}, \tag{5.32}$$

and $D_{\text{SD}}^{\text{IF}} + D_{\text{SD}}^{\text{FI}}$ is the counterterm for the QCD Compton scattering defined in Eqn. 2.22a. The ND-dipoles can be easily integrated over the 1-parton phase-space of the emitted particle and the result of the integration is a finite term that has to be included in the virtual piece of the cross section. The results are shown in Fig. 5.3. The p_T (left panel) and rapidity distribution (right panel) of the outgoing lepton match very well within the statistical fluctuations. This demonstrates that the phase-space integration works correclty and that the mismatch pointed out in Fig. 5.2 is not caused by the NLO phase-space implementation.

We would now like to provide a test that is focussed on observables that are more sensitive to the extra-jet. In order to study the real emission, we consider the transverse energy flows and the thrust distribution, which are specifically sensitive to the hard radiation [44]. We compare the results of the dipole shower, with and without POWHEG corrections (solid blue line and red dashed line respectively), with the transverse energy flow in DIS from Ref. [158]. As in the previous Chapter, the cross section for the transverse energy flow, $\frac{1}{N}\frac{dE_\perp^*}{d\eta^*}$, is shown as a function of pseudorapidity, η^*. The superscript * is used to label the quantities in the hadronic
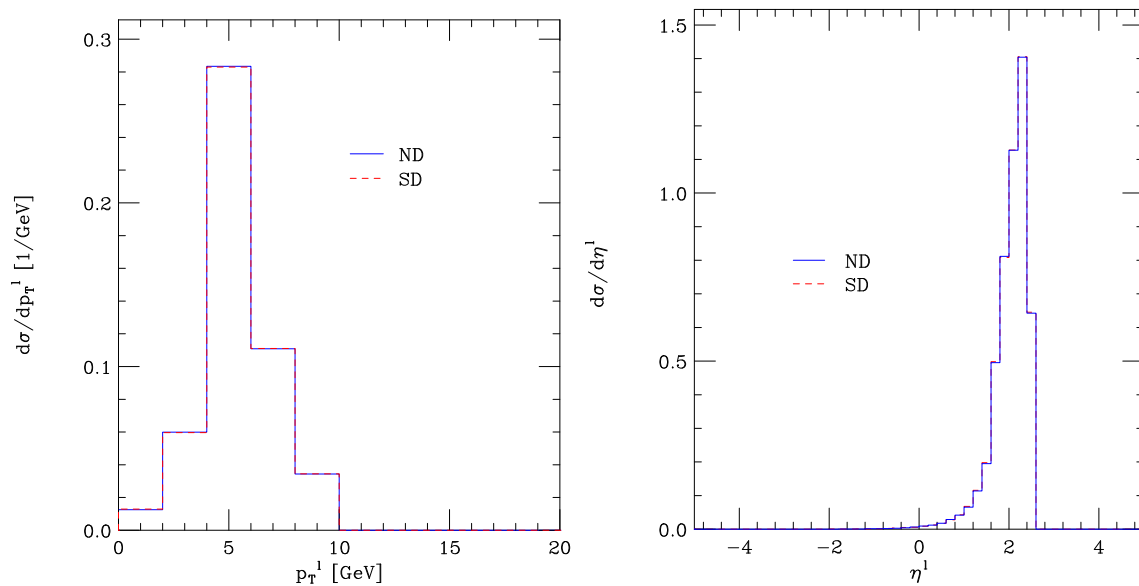
Figure 5.3: NLO cross section comparison between ND-dipoles (solid blue line) and SD-dipoles (dashed red line). We plot the p_T (left panel) and rapidity (right panel) distribution of the outgoing electron. In both cases the distributions match very well.

centre of mass system and N is the total number of DIS events. We choose the high Q^2 sample of Ref. [158] and provide two sets of results. In Fig. 5.4 we show the transverse energy flow for different values of the Bjorken scale, x, and Q^2. The lower frame shows the ratio theory/data and the yellow band gives the one sigma error of the data. Here and in the following the distributions are plotted with the Rivet package [145]. In Fig. 5.4a the LO dipole shower provides a bad description of data and this problem is overcome with the POWHEG corrections: the NLO distribution describes the data very well and the ratio theory/data stays within the one sigma error of the measurement (see lower frame). However, the ratio theory/data of the NLO distributions is bigger for higher values of Q^2, and for low values of η^* the LO simulation seems to give a better description of the data of Ref. [158]: see Figs. 5.4c-f. This behaviour is not expected. A careful analysis of Figs. 5.4b-e shows that the LO and NLO simulations are equally not optimal for $\eta^* \approx 2$ and the same happens for $\eta^* \approx 1.5$ in Fig. 5.4f. Moreover, a systematic deviation from the data seems to characterise the LO and NLO distributions of Fig. 5.4g at low η^*.

In Fig. 5.5 we show the transverse energy flow for different ranges of Q^2 and after integrating over x. Here again it emerges that the NLO simulation describes the HERA data very well at low values of Q^2, while the LO distribution stays below the measurement, see Fig. 5.5a-b. However, we observe a systematic deviation that appears for both the LO and NLO curves at $\eta^* \approx 2.7$ in Fig. 5.5b. For $Q^2 > 400\,\mathrm{GeV}^2$ the LO simulation gives a better description and both distributions deviate from the data with a ratio theory/data ≈ 1.6 for $\eta^* \approx 2.3$.

The behaviour of the shower is not fully understood yet, as the shower is still under testing/debugging. As mentioned in the introduction of the present Chapter, the implementation of the DIS was made with the purpose of testing the dipole
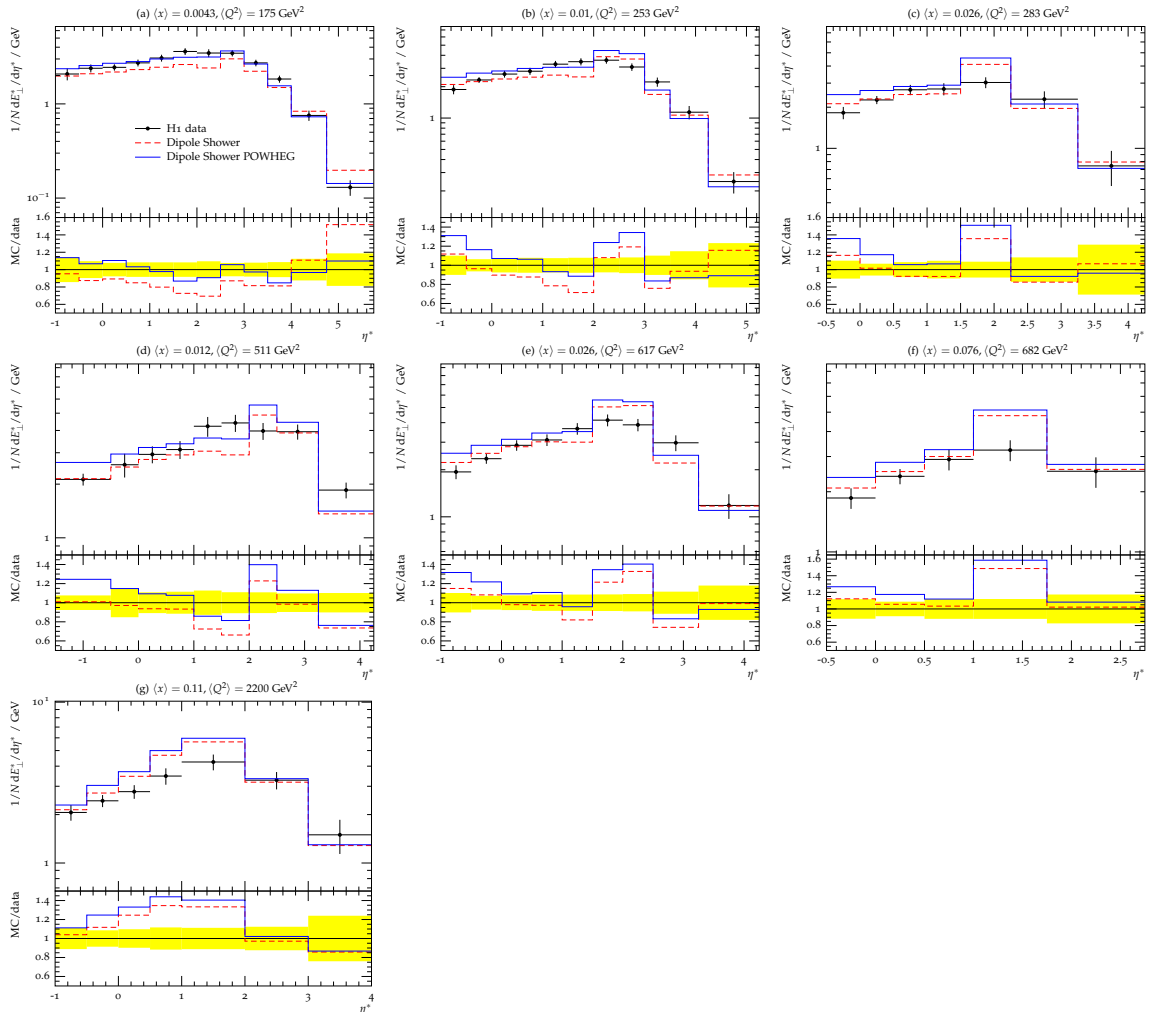
Figure 5.4: The inclusive transverse energy flow $\frac{1}{N}\mathrm{d}E_\perp^*/\mathrm{d}\eta^*$ at different values of x and Q^2 for the high Q^2 sample from [158]. The lower frame shows theory/data and the yellow band gives the one sigma error of the data.
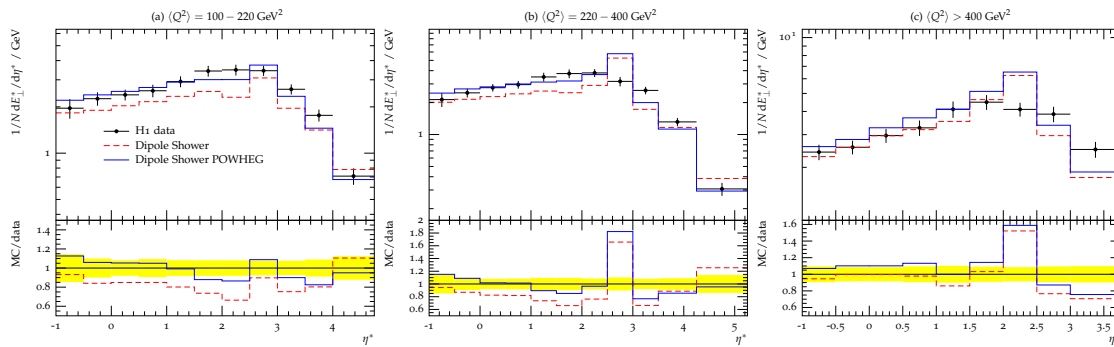
Figure 5.5: The inclusive transverse energy flow $\frac{1}{N}\mathrm{d}E_\perp^*/\mathrm{d}\eta^*$ at different values of Q^2 for the high Q^2 sample from [158]. The lower frame is as described in Fig. 5.4.

shower for the initial-final and final initial radiation. The present work has given strong hints to direct debugging and further tests, and the results have improved significantly with the passing of time. At the present stage we consider the results to be in a reasonable agreement with the data, but further improvement are expected to come.

We will first need to understand the behaviour of the shower better. Then we will need to study with care the effects of the hadronization model and understand how simulation could be improved in this direction. As mentioned in the previous Chapter, the transverse energy flow in DIS turned out to be very sensitive to the value of the mass parameter for the splitting of the soft beam remnant cluster and a tuning of this parameter was needed to optimize the results from Herwig++. A similar tuning was tried for Matchbox but did not provide the expected results. Furthermore, we expect higher order corrections to NLO to be necessary for a satisfactory simulation, as shown in Ref. [159]. In the latter work simulations with SHERPA were compared with the transverse energy flow in DIS from Ref. [160]. It was shown that Monte Carlo predictions gradually improve with a growing number of final-state partons in the hard matrix element. They observed that if only two final-state partons are considered in the matrix element, the Monte Carlo prediction is far off the data. The 3-parton sample gives an improved description, but the data is described in a satisfactory way only by a 4-parton sample.

We now look at observables that are sensitive to the geometric distribution, or *shape*, of the jets. In 1977 Sterman and Weinberg pioneered a method used to predict the production of jets in e^+e^- events using QCD [161]. The model included two variables that are of great importance to qualify and quantify the shape of an event: *thrust* and *broadening*.

The thrust measures the longitudinal collimation of the jets in the event and the broadening measures the spatial distribution. They are respectively defined as:

$$T = \frac{\sum_i |\vec{p}_i \cdot \vec{n}|}{\sum_i |\vec{p}_i|} = \frac{\sum_i |p_i^{||}|}{\sum_i |\vec{p}_i|}, \tag{5.33a}$$

$$B = \frac{\sum_i |\vec{p}_i \times \vec{n}|}{\sum_i |\vec{p}_i|} = \frac{\sum_i |p_i^\perp|}{\sum_i |\vec{p}_i|}. \tag{5.33b}$$

The sum is over all momenta of the particles in the *current hemisphere* of the

Breit frame[3], while $\vec{n}$ defines the unit vector in the chosen direction. The common direction used in analysis is either the *photon axis*, which is the direction of the virtual photon, or the *thrust axis*, which is the direction in which the thrust is maximised.

Here we choose the thrust axis and compare the simulation from the dipole shower with the result from Ref. [162]; the dipole shower analysis was performed with the program Rivet which, thus far, only provides correct results for the thrust for the data of Ref. [162].

Fig. 5.6 shows the thrust for the LO and NLO dipole shower (solid blue and dashed red respectively) at different values of the Bjorken scaling variable x and Q^2, for the high Q^2 sample of Ref. [162]. The lower frame is as described in Fig. 5.4. It is necessary to exclude events in which the energy in the current hemisphere is less than a certain limit; *i.e.* a cut, ϵ_{lim}, is needed to ensure infrared safety. The distributions are normalised such that n refers to the number of events in the (x, Q^2) bin after the ϵ_{lim} cut is applied and N to the total number of events in the (x, Q^2) bin before the ϵ_{lim} cut (cf. Ref. [162–164]).

In Figs. 5.6a-b the LO and NLO simulations describe the data well for $0.7 < T < 0.95$ and $0.8 < T < 0.95$ and they both deviate from the data for lower values of the thrust. In Figs. 5.6c-f the LO dipole shower provides a better simulation: the lower frame shows that the red dashed line fluctuates within the yellow band or it stays closer to it than the solid blue line. The POWHEG corrections provide a good description of data for high Q^2, as is shown in Fig. 5.6g. In the latter case, the LO shower also simulate the data well, with the exception of the range $0.75 < T < 0.8$, where the ratio MC/data $\approx$ 2.

As mentioned before, we expect to optimize the results with a better understanding of the dipole shower, which is currently in a stage of test/debugging. The effect of the hadronization model has to be considered with care and we need to understand how the results can be improved in this direction. Another candidate for the improvement of the results is the higher order correction to NLO that we expect to be relevant for the simulation of the thrust as well.

5.3 Conclusions

DIS is a very well known process in the literature and provides an important test bed for the initial-final and final-initial radiation of the dipole shower. In this Chapter we have discussed the POWHEG implementation of this process into the dipole shower of Ref. [4]

Matchbox provides an automated way to compute and implement $\bar{B}$, while the NLO phase-space was implemented as discussed in the present Chapter. We have calculated the phase-space measure, the outgoing momenta and the variables have been parametrized in terms of the unit cube.

A preliminary check of the implementation has been performed by comparing the NLO cross section of Matchbox and Herwig++. The tiny differences that we found

---

[3]In the Breit frame the current hemisphere or current region is the hemisphere of space containing the final state partons.
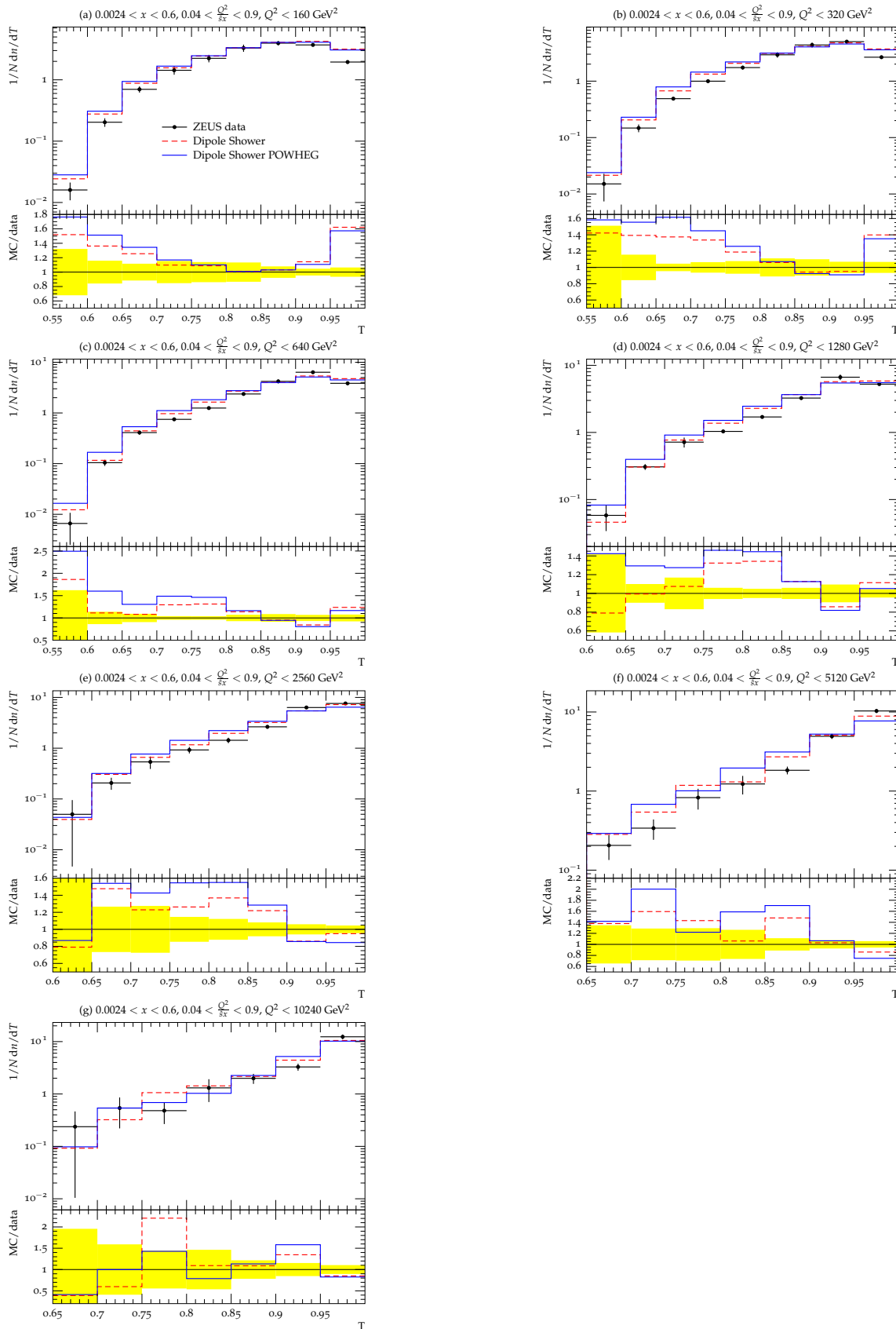
Figure 5.6: The thrust at different values of x and Q^2 for the high Q^2 sample from Ref. [162]. The lower frame provides the same information as Fig. 5.4.

in the p_T and rapidity distributions of the outgoing lepton were studied in detail by providing the integration of the phase-space with two different sets of dipoles. The good agreement of the distributions showed that the mismatch is not caused by the NLO phase-space implementation.

A further test has been performed on observables that are sensitive to the emission of the extra-jet: transverse energy flow and thrust. Here we find that for some ranges of rapidity and thrust, the LO simulation is better than the NLO distribution. This is not expected. However, the dipole shower is still in a stage of test/debugging. The present work has contributed to the test of initial-final and final-initial radiation of the shower but we expect further improvements to be made. A better understanding of the shower, the tuning of parameters describing the hadronization model and the higher order corrections to NLO are the main candidates for such improvement. Given the status of the shower, we consider the results of the present work to be in reasonable agreement with the HERA data of Refs. [158] and [162].

Here we have compared the NLO cross sections of Matchbox and Herwig++. At this stage, it is of principle interest to deepen the comparison of the descriptions provided by the two showers. We will compare the distributions of transverse energy flow, discussed for Herwig++ in Chapter 4, and the thrust that has not yet been considered for Herwig++. We devote the next Chapter to completing the studies of the present work by giving details on such comparison.

Chapter 6

Comparing the DIS implementation for **Herwig++** and **Matchbox**

As already discussed, deep inelastic scattering was of great importance for the study and understanding of the internal structure of hadrons and is now very well known in the literature. In the present work, the NLO QCD corrections to DIS were implemented into the Herwig++ and Matchbox parton showers according to the POWHEG matching scheme, as shown in Chapters 4 and 5 respectively. The two approaches are different, as was extensively discussed in the previous Chapters, and it is useful to recap the main aspects of the two implementations here.

The implementation of DIS into the Herwig++ parton shower was performed along the same lines as the Higgs production via vector boson fusion (see Chapter 2). I worked on the implementation of the $\bar{B}$ and the NLO phase-space. In the latter the transferred momentum, Q^2, is computed in the Breit frame at LO and then used for the generation of the NLO momenta (cf. Eqns. 2.2a-2.2c).

The implementation of DIS in Matchbox provides an important test for the initial-final and final-initial radiation of the dipole shower. I worked on the implementation of the NLO phase-space, while $\bar{B}$ is automatically computed by the program itself. As required, the NLO phase-space is independent from the LO one and Q^2 is one of the phase-space variables.

At this stage it is of interests to compare the result produced by the two different simulations. In this Chapter we will present the results of the comparison in Sect. 6.1 and conclusions in Sect. 6.2.

6.1   Results

This Section is devoted to a comparison of distributions of transverse energy flow and thrust from Herwig++ and Matchbox.

In Fig. 6.1 we collect the results for the transverse energy flow that were shown in Chapters 4 and 5. We compare the distributions from Herwig++ and Matchbox without POWHEG corrections (dotted green and dashed red line respectively) and the corresponding NLO curves (dashed-dotted magenta and solid blue respectively).

We focus on the high Q^2 sample of Ref. [158] and show distributions for different ranges of Q^2 and x. The lower frame gives the ratio theory/data and the yellow band the one sigma error. Here and in the following the distributions were plotted with the Rivet package [145].

In Figs. 6.1a-g both LO simulations show a deficit of radiation between $1 < \eta^* < 3$. This is very evident for the Herwig++ distributions; therefore, we conclude that the dipole shower without NLO correction provides a better description compared to the LO Herwig++. The lack of radiation is remedied by using the POWHEG correction, as the solid blue and dashed-dotted magenta lines show. Both NLO parton showers provide a very good description of the data in Fig. 6.1a. The NLO simulation of the dipole shower shows a bigger theory/data ratio for higher values of Q^2, while Herwig++ presents satisfactory NLO results (Fig. 6.1b-f): the dashed-dotted curve stays within the yellow band and it is rare that the LO Herwig++ simulation is better than the NLO one (cf. $\eta^* < 0$ in Fig. 6.1g). However, it has to be mentioned that the systematic deviations that we have pointed out in the previous Chapter for the dipole shower at LO and NLO (cf. $\eta^* \approx 2$ in Figs. 6.1b-e and $\eta^* \approx 1.5$ in Fig. 6.1f) have been removed from the Herwig++ curves by tuning the mass parameter for the splitting of soft beam remnant clusters to 0.5 GeV, as discussed in Chapter 4. A similar tuning was tried for the dipole shower but it did not provide the expected improvement. The transverse energy flow in DIS is very sensitive to this parameter and perhaps a different tuning is needed for the dipole shower.

In Fig. 6.2 we show the transverse energy flow from the two showers for different ranges of Q^2 and after integrating over x. Also in this case it is evident that the LO description provided by the dipole shower is better than the corresponding LO Herwig++ curve (cf. Fig. 6.2a-c). The NLO dipole shower describes the data of Ref. [158] very well for low ranges of Q^2 (cf. Fig. 6.1a-b), even though the Herwig++ simulation is very satisfactory at NLO. For $Q^2 > 400 \, \mathrm{GeV}^2$ the dipole shower without POWHEG corrections gives the best description of the measurements of Ref. [158] with the exception of the deviation at $\eta^* \approx 2.3$ that we may reasonably solve with an optimal tuning of the parameters of the hadronization model.

Figs. 6.1-6.2 collect the plots that we have shown in Chapter 4 and 5, but the thrust has only been discussed for the dipole shower thus far. We dedicate the last part of the present section for the comparison of distributions of this observable. In Fig. 6.3 we show the distributions for thrust at different values of Q^2 and Bjorken scale x. The simulation at LO and NLO for both Herwig++ and Matchbox are compared with the data of Ref. [162]. The thrust is calculated in the current hemisphere of the Breit frame and along the thrust axis. The legend is as in Fig. 6.2 and the yellow band is described in Fig. 6.2 as well. In this case, the systematic deviations from the yellow band are not removed by tuning the mass parameter for the splitting of soft beam remnant cluster to 0.5 GeV. It is relevant to notice that both showers present a similar deviation for low values of thrust in Figs. 6.3a-c and for $0.7 < T < 0.85$ in Fig. 6.3d-e. In the same regions the showers show a better description at LO. The big deviation present in Fig. 6.3f for the NLO Herwig++ parton shower has been studied for different values of the mass parameter and the results did not show a relevant improvement. However, the two approaches provide
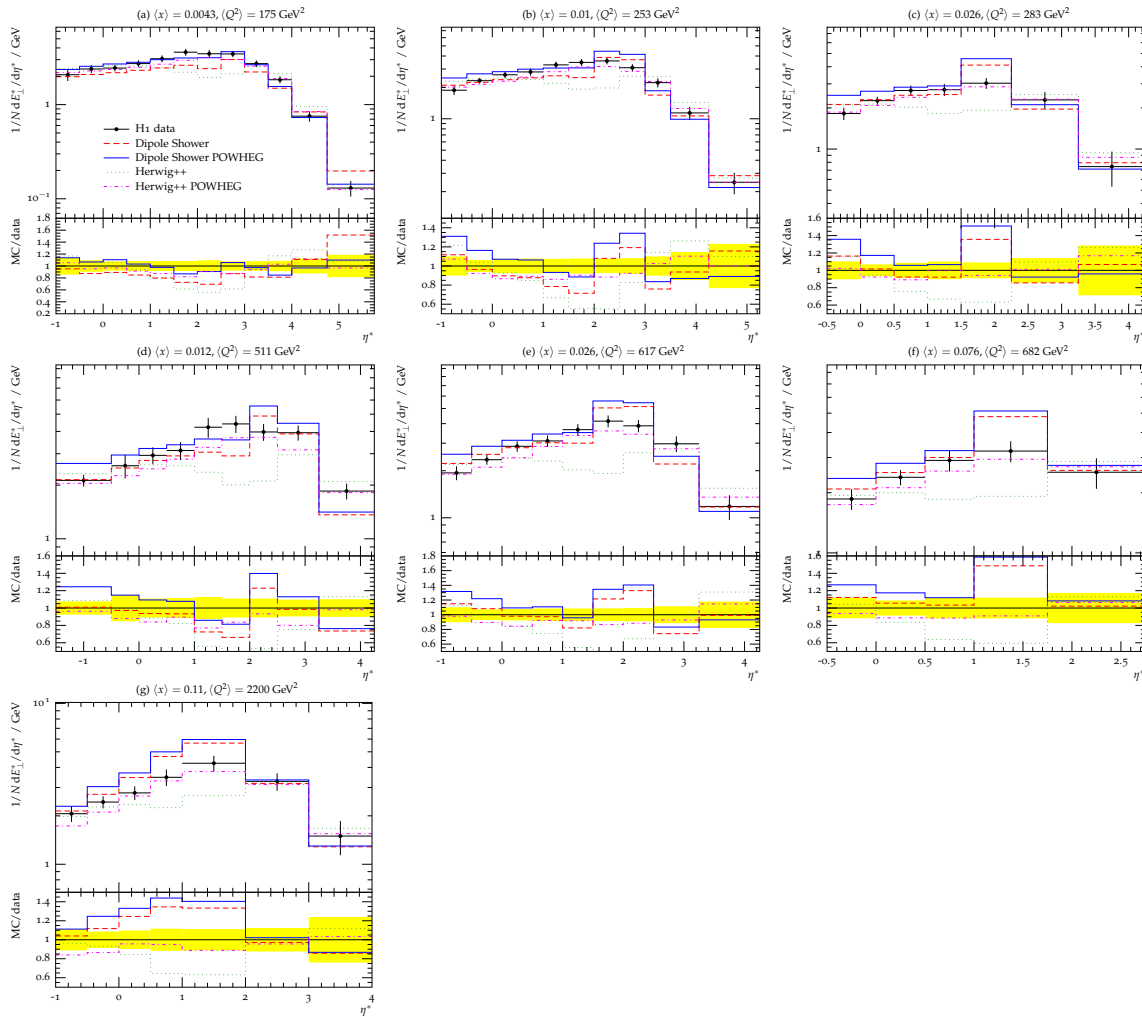
Figure 6.1: The inclusive transverse energy flow $\frac{1}{N}dE_T^*/d\eta^*$ at different values of x and Q^2 for the high Q^2 sample from [158]. The lower frame shows theory/data and the yellow band gives the one sigma error of the data.
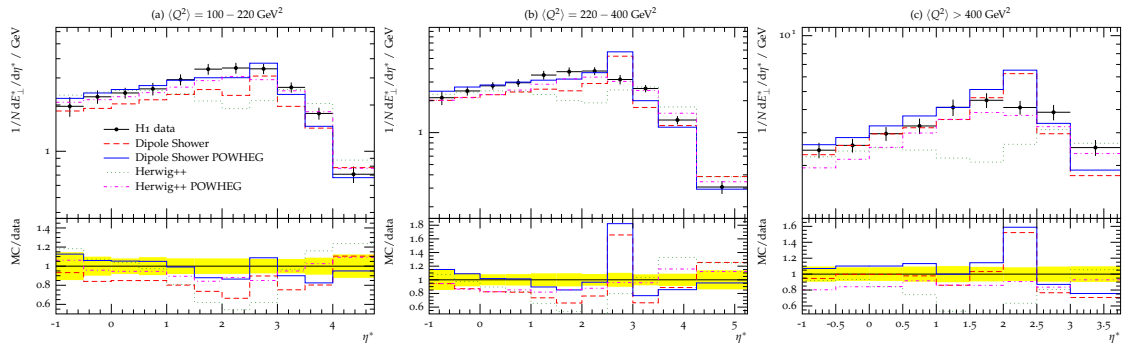
Figure 6.2: The inclusive transverse energy flow $\frac{1}{N}dE_T^*/d\eta^*$ at different values of Q^2. The high Q^2 sample from [158] is considered here. The lower frame shows theory/data and the yellow band gives the one sigma error of the data.

a reasonable description of the data from Ref. [162]. The dipole shower provides a better description at high values of Q^2. We assume that NNLO corrections are needed to improve the description of the two showers for this observable but we do not exclude the possibility to optimize the similation with further study.

6.2 Conclusions

The present Chapter was devoted to a comparison of the Herwig++ and dipole shower implementations of the POWHEG method for the DIS process. First we have summarized the main features of the approaches followed for the two showers. For both of them we have then considered distributions of inclusive transverse energy flow and thrust, and we have compared them with the data of Ref. [158] and Ref. [162] respectively.

The analysis regarding the transverse energy flow shows that the dipole shower provides a better description of the data of Ref. [158] at LO compared to the LO Herwig++ shower. However, the NLO simulation from Matchbox does not produce an equivalent improvement: the fluctuations are not always contained in the one sigma error of the data and the LO simulation is better in some ranges of η^* and for different values of $< Q^2 >$. The LO Herwig++ simulations show a very evident deficit of radiation for $1 < \eta^* < 3$ that is remedied by using the POWHEG correction. The NLO Herwig++ distributions describe the data very well, with fluctuations that are contained in the yellow band of the lower frame. However, we have become aware that the transverse energy flow in DIS is most sensitive to the mass parameter for the splitting of soft beam remnant cluster. Deviations similar to the ones pointed out in the previous Chapter for the dipole shower have been cured in the Herwig++ distributions by tuning this parameter. A similar tuning did not give the expected improvement for the dipole shower but we expect that a different tuning would help for the optimization of the results. The dipole shower is still in a stage of test/debugging: we consider the results to be reasonably good but expect to improve the simulation in the near future.

Tuning the parameter of the hadronization model did not improve the results of both showers for the thrust. We have pointed out systematic deviations that are present in ranges of thrust where the LO simulations show a better description. However, the Herwig++ and dipole showers provide a reasonable description of the data from Ref. [162] and we expect the simulations to be improved with further study.
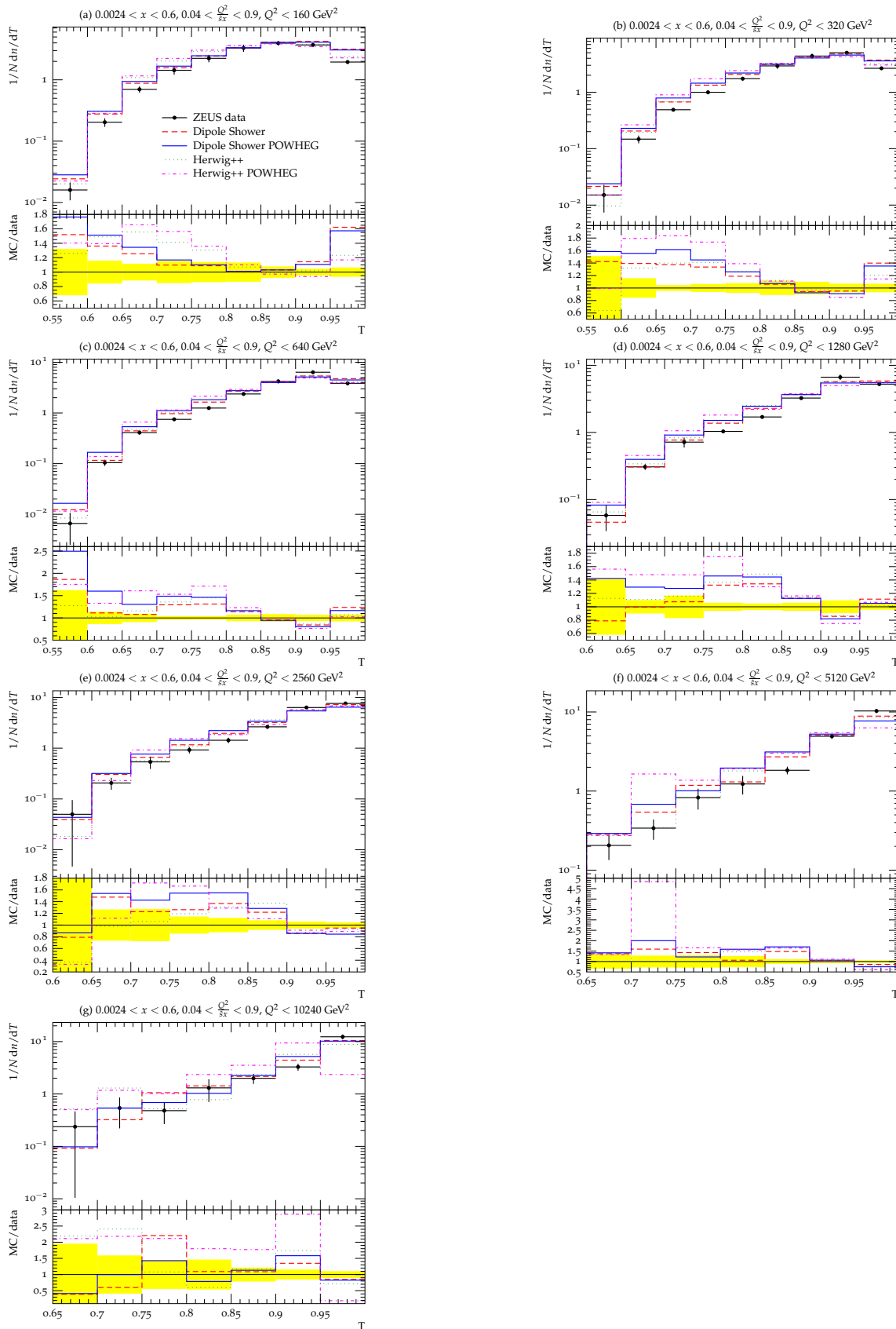
Figure 6.3: The thrust at different values of x and Q^2. The high Q^2 sample from Ref. [162] is considered here. The lower frame provides the same information as in Fig. 6.1.

Chapter 7

Conclusions

The Large Hadron Collider at CERN has recently started operating, launching a new era of research in particle physics. Exciting new physics, including new particles, are expected to be found in the very near future and the potential for making a new discovery depends on the accuracy of event generators in describing both signal and background processes. Many efforts have been put into developing a new generation of event generators intended for use throughout the LHC data analysis era. To this end, great attention has been focussed on the improvement of parton showers using matrix element corrections.

Parton showers provide a resummation of the logarithmic enhancement that are associated with soft and collinear emissions. This formalism has been very successful but it has some limits in its applicability. In the standard approach the parton branching is based on the collinear approximation and the parton shower description becomes unreliable for large transverse momentum emissions: there is a region of phase-space, referred to as the dead zone, into which the shower cannot radiate. On the other hand, fixed-order matrix element calculations give a good description of emissions with large transverse momentum and they are the main candidate for the improvement of the parton shower description. However, the naive interface of parton showers and NLO corrections would imply a double counting of the region of phase-space where they both radiate.

A formalism is therefore needed to merge the two worlds such that the resummation of the shower is retained, the description of large transverse momentum emission is improved with the exact matrix elements and the double counting is removed. A number of different matrix element merging (or matching) schemes have been developed over the last few years. The first successful systematic method is known as MC@NLO. However, the novel POWHEG method has the advantage of producing only positive weights. It corrects the hardest emission with the NLO cross section and therefore requires angular ordered parton showers to be reorganized in terms of truncated showers, vetoed showers and hardest emission.

In the present thesis, the POWHEG matching scheme has been studied within the standard Herwig++ parton shower and the new dipole-type shower of Ref. [4]. The latter formalism generalises the standard parton shower branching by introducing exact energy-momentum conservation within the splitting, with the consequent disappearance of the dead zone. Unlike the Herwig++ parton shower, which is angu-

lar ordered, the evolution of the dipole shower is described in term of the transverse momentum of the emitted particle and no reorganization of the shower is needed for the implementation of the POWHEG method.

The POWHEG method was first applied to Higgs production via vector boson fusion (VBF) in the Herwig++ parton shower. This process is expected to play a fundamental rôle in the measurement of the Higgs coupling to fermions and gauge bosons, because it allows for different decay channels, such as $H \to \tau^+\tau^-$ and $H \to W^+W^-$. We found that the POWHEG implementation improves the cross section for rapidity separation of the two tagging jet and transverse momentum and rapidity for the third hardest jet, while it leaves the rest of the distributions unchanged with respect to the LO Herwig++. The lack of data prevents us from comparing jet distributions with experiment results. However, we expect this implementation to be an important tool for analysing the upcoming results at the LHC.

The POWHEG scheme was then implemented for diphoton production in hadron-hadron collisions in the Herwig++ parton shower. This process is considered one of the main backgrounds for the discovery channel of the Higgs boson decaying into two photons, for Higgs masses below 140 GeV. The POWHEG approach was found to give a good description of the data of Refs. [124,125]. A remarkably good description is obtained for infrared sensitive observables, like the transverse momentum of the $\gamma\gamma$-pair, that demonstrates the resummation of logarithmic enhancement provided by the Herwig++ shower. The implementation is based on a general approach that treats QED singularities by simulating the LO cross section for the corresponding process and then showering it rather than using the fragmentation function. This approach turned out to be successful and very efficient, and it will be implemented in VBFNLO for processes with final state photons in the near future.

Deep inelastic scattering (DIS) has been of great importance for the study of the internal structure of hadrons since the 1960s and is now a well known process in the literature. Its implementation in the Herwig++ parton shower within the POWHEG merging scheme was also shown in the present thesis. The approach followed the one used for VBF. We first compared results with DISENT and found excellent agreement, which demonstrates that the NLO cross section is correctly implemented. We thus found results to be in good agreement with the measurement of Refs. [154,155,158].

The same process was studied in the dipole shower within the POWHEG formalism. The latter algorithm is implemented in the shower in an automated way and I worked on the NLO phase-space that provides the NLO momenta and phase-space integration of the differential cross section. The implementation aimed to test the shower for the final-initial and initial-final radiation. We found a tiny mismatch with the NLO cross section from Herwig++. The mismatch was carefully studied with an explicit test on the integration of the NLO phase-space and the positive results that we obtained demonstrated that the mismatch is not caused by the NLO phase-space implementation. Furthermore, we compared results with the data of Refs. [158,162] and found that the LO simulation is better than NLO in some ranges of rapidity and thrust. The dipole shower is still in the test/debugging stage and we consider the results to be in a reasonable agreement with the data. However, we expect further improvement to come in the near future.

Finally, the implementations of DIS in the two showers were analysed together. The results from Herwig++ and the dipole shower at LO and NLO were compared with the data of Refs. [158, 162]. For the transverse energy flow, we find that the dipole shower provides a better description at LO than the LO Herwig++, but this improvement is not present at NLO. We found standard Herwig++ shower with POWHEG corrections to give very satisfactory results. The thrust is described reasonably well from the two showers but the tuning of parameter of the hadronization model did not show the expected improvement.

In summary, we have presented research in the implementation and development of matching parton showers with matrix element corrections. Successful results have been shown for an implementation that is expected to be a relevant tool for the analysis of data for the Higgs detection at the LHC and for a general approach, which describes QED singularities in processes with final states photons, that will be implemented in VBFNLO in the near future. In addition, very interesting results have been shown for the novel dipole shower and they are expected to be of great help with upcoming improvements of the description of the shower. Results, such as these, are extremely significant. The LHC promises to unlock scientific mysteries about the creation of the Universe and the fundamental nature of matter, and Monte Carlo event generators will play a major rôle.

Acknowledgments

First, I would like to thank my mother. I am and will always be immensely indebted to her for allowing me to realize my own potential. Life wanted her to be both mother and father and she succeeded in this hard task. All the support she has provided me over the years was the greatest gift anyone has ever given me and without her, I may never have gotten to where I am today.

Special thanks go to my supervisors, Stefan Gieseke and Peter Richardson, who have given me the opportunity to do a Ph.D. that has been a very fruitful, personal and professional, experience that I will carry with me lifelong. I have learnt a lot from them and I am indebted to them for the help and encouragement, linguistically and otherwise. Many thanks go to Dieter Zeppenfeld who has given me several valuable hints and comments on my work, especially during the TP research seminars.

I would also like to thank Simon Plaetzer with whom I have collaborated during my Ph.D.: I have benefited a lot from our interesting discussion. I am grateful to David Grellscheid and Mike Seymour who have kindly helped me for many programming problems and otherwise. Many thanks go to the other Herwig++ authors: I have benefited from their advice and comments, and enjoyed the contact with all of them.

I thank my office mate Paco for the several advices that he has given me in the last years; I have always enjoyed our discussion and it was a good time sharing the office with him. I thank Sophy who has kindly volunteered to read my PhD thesis and many thanks go to all other members of the TP institute for making my time in Karlsruhe an enjoyable one.

Bibliography

[1] P. Nason, *A new method for combining NLO QCD with shower Monte Carlo algorithms*, *JHEP* **11** (2004) 040, [`hep-ph/0409146`].

[2] S. Frixione, P. Nason, and C. Oleari, *Matching NLO QCD computations with parton shower simulations: the POWHEG method*, *JHEP* **11** (2007) 070, [`hep-ph/0709.2092`].

[3] M. Bahr *et. al.*, *Herwig++ physics and manual*, *Eur. Phys. J.* **C58** (2008) 639–707, [`arXiv:0803.0883`].

[4] S. Platzer and S. Gieseke, *Coherent parton showers with local recoils*, *JHEP* **01** (2011) 024, [`arXiv:0909.5593`].

[5] R. K. Ellis, W. J. Stirling, and B. R. Webber, *QCD and collider physics*, *Camb. Monogr. Part. Phys. Nucl. Phys. Cosmol.* **8** (1996) 1–435.

[6] G. Dissertori, I. G. Knowles, and M. Schmelling, *Quantum chromodynamics: high energy experiments and theory*, *Oxford University Press* (2003).

[7] H. Fritzsch, M. Gell-Mann, and H. Leutwyler, *Advantages of the color octet gluon picture*, *Phys. Lett.* **B47** (1973) 365–368.

[8] L. D. Faddeev and V. N. Popov, *Feynman diagrams for the Yang-Mills field*, *Phys. Lett.* **B25** (1967) 29–30.

[9] M. E. Peskin and D. V. Schroeder, "An introduction to quantum field theory." Reading, USA: Addison-Wesley (1995) 842.

[10] H. D. Politzer, *Reliable perturbative results for strong interaction*, *Phys. Rev. Lett.* **30** (1973) 1346–1349.

[11] D. J. Gross and F. Wilczek, *Ultraviolet behavior of non-abelian gauge theories*, *Phys. Rev. Lett.* **30** (1973) 1343–1346.

[12] F. Bloch and A. Nordsieck, *Note on the radiation field of the electron*, *Phys. Rev.* **52** (1937) 54–59.

[13] T. Kinoshita, *Mass singularities of Feynman amplitudes*, *J. Math. Phys.* **3** (1962) 650–677.

[14] T. D. Lee and M. Nauenberg, *Degenerate systems and mass singularities*, *Phys. Rev.* **133** (1964) 1549–1562.

Bibliography

[15] G. Altarelli and G. Parisi, *Asymptotic freedom in parton language, Nucl. Phys.* **B126** (1977) 298.

[16] V. N. Gribov and L. N. Lipatov, *Deep inelastic e p scattering in perturbation theory, Sov. J. Nucl. Phys.* **15** (1972) 438–450.

[17] A. Bassetto, M. Ciafaloni, G. Marchesini, and A. H. Mueller, *Jet multiplicity and soft gluon factorization, Nucl. Phys.* **B207** (1982) 189.

[18] A. Bassetto, M. Ciafaloni, and G. Marchesini, *Jet structure and infrared sensitive quantities in perturbative QCD, Phys. Rept.* **100** (1983) 201–272.

[19] S. Catani and M. Ciafaloni, *Many gluon correlations and the quark form-factor in QCD, Nucl. Phys.* **B236** (1984) 61.

[20] M. Ciafaloni, *Exponentiating soft emission in QCD, Phys. Lett.* **B95** (1980) 113.

[21] Y. L. Dokshitzer, V. A. Khoze, and S. I. Troian, *Coherence and physics of QCD jets, Adv. Ser. Direct. High Energy Phys.* **5** (1988) 241–410.

[22] A. H. Mueller, *On the multiplicity of hadrons in QCD jets, Phys. Lett.* **B104** (1981) 161–164.

[23] B. I. Ermolaev and V. S. Fadin, *Log-log asymptotic form of exclusive cross-sections in quantum chromodynamics, JETP Lett.* **33** (1981) 269–272.

[24] Y. L. Dokshitzer, V. S. Fadin, and V. A. Khoze, *Coherent effects in the perturbative QCD parton jets, Phys. Lett.* **B115** (1982) 242–246.

[25] G. Marchesini and B. R. Webber, *Simulation of QCD coherence in heavy quark production and decay, Nucl. Phys.* **B330** (1990) 261.

[26] T. Sjostrand, S. Mrenna, and P. Z. Skands, *PYTHIA 6.4 physics and manual, JHEP* **05** (2006) 026, [`hep-ph/0603175`].

[27] G. Corcella *et. al., HERWIG 6.5: an event generator for hadron emission reactions with interfering gluons (including supersymmetric processes), JHEP* **01** (2001) 010, [`hep-ph/0011363`].

[28] T. Sjostrand, S. Mrenna, and P. Z. Skands, *A brief introduction to PYTHIA 8.1, Comput. Phys. Commun.* **178** (2008) 852–867, [`arXiv:0710.3820`].

[29] T. Gleisberg *et. al., Event generation with SHERPA 1.1, JHEP* **02** (2009) 007, [`arXiv:0811.4622`].

[30] A. Giovannini, *QCD jets as Markov branching processes, Nucl. Phys.* **B161** (1979) 429–448.

[31] P. Cvitanovic, P. Hoyer, and K. Zalewski, *parton evolution as a branching process, Nucl. Phys.* **B176** (1980) 429.

[32] P. Cvitanovic, P. Hoyer, and K. Konishi, *Partons and bramching*, *Phys. Lett.* **B85** (1979) 413.

[33] G. C. Fox and S. Wolfram, *A model for parton showers in QCD*, *Nucl. Phys.* **B168** (1980) 285.

[34] G. Marchesini and B. R. Webber, *Simulation of QCD jets including soft gluon interference*, *Nucl. Phys.* **B238** (1984) 1.

[35] S. Gieseke, P. Stephens, and B. Webber, *New formalism for QCD parton showers*, *JHEP* **12** (2003) 045, [hep-ph/0310083].

[36] S. Catani and M. H. Seymour, *A general algorithm for calculating jet cross sections in NLO QCD*, *Nucl. Phys.* **B485** (1997) 291–419, [hep-ph/9605323].

[37] S. Plätzer, "Parton shower and radiative corrections in QCD." PhD thesis.

[38] T. Sjostrand and M. Bengtsson, *The Lund Monte Carlo for jet fragmentation and e+ e- physics. Jetset version 6.3: an update*, *Comput. Phys. Commun.* **43** (1987) 367.

[39] M. Bengtsson and T. Sjostrand, *Parton showers in leptoproduction events*, *Z. Phys.* **C37** (1988) 465.

[40] E. Norrbin and T. Sjostrand, *QCD radiation off heavy particles*, *Nucl. Phys.* **B603** (2001) 297–342, [hep-ph/0010012].

[41] G. Miu and T. Sjostrand, *W production in an improved parton shower approach*, *Phys. Lett.* **B449** (1999) 313–320, [hep-ph/9812455].

[42] G. Corcella *et. al.*, *HERWIG 6.5 release note*, [hep-ph/0210213].

[43] M. H. Seymour, *Photon radiation in final state parton showering*, *Z. Phys.* **C56** (1992) 161–170.

[44] M. H. Seymour, *Matrix element corrections to parton shower simulation of deep inelastic scattering*, . Contributed to 27th International Conference on High Energy Physics (ICHEP), Glasgow, Scotland, 20-27 Jul 1994.

[45] G. Corcella and M. H. Seymour, *Matrix element corrections to parton shower simulations of heavy quark decay*, *Phys. Lett.* **B442** (1998) 417–426, [hep-ph/9809451].

[46] G. Corcella and M. H. Seymour, *Initial state radiation in simulations of vector boson production at hadron colliders*, *Nucl. Phys.* **B565** (2000) 227–244, [hep-ph/9908388].

[47] M. H. Seymour, *Matrix element corrections to parton shower algorithms*, *Comp. Phys. Commun.* **90** (1995) 95–101, [hep-ph/9410414].

Bibliography

[48] M. H. Seymour, *A simple prescription for first order corrections to quark scattering and annihilation processes*, Nucl. Phys. **B436** (1995) 443–460, [`hep-ph/9410244`].

[49] S. Gieseke, A. Ribon, M. H. Seymour, P. Stephens, and B. Webber, *Herwig++ 1.0: an event generator for* e^+e^- *annihilation*, JHEP **02** (2004) 005, [`hep-ph/0311208`].

[50] S. Gieseke, *The new Monte Carlo event generator Herwig++*, `hep-ph/0408034`.

[51] K. Hamilton and P. Richardson, *A simulation of QCD radiation in top quark decays*, JHEP **02** (2007) 069, [`hep-ph/0612236`].

[52] S. Gieseke *et. al.*, *Herwig++ 2.0 release note*, [`hep-ph/0609306`].

[53] M. Bahr *et. al.*, *Herwig++ 2.2 release note*, [`hep-ph/0804.3053`].

[54] S. Gieseke, D. Grellscheid, K. Hamilton, A. Papaefstathiou, S. Platzer, *et. al.*, *Herwig++ 2.5 release note*, `arXiv:1102.1672`.

[55] S. Catani, F. Krauss, R. Kuhn, and B. R. Webber, *QCD matrix elements + parton showers*, JHEP **11** (2001) 063, [`hep-ph/0109231`].

[56] F. Krauss, *Matrix elements and parton showers in hadronic interactions*, JHEP **08** (2002) 015, [`hep-ph/0205283`].

[57] L. Lonnblad, *Correcting the colour-dipole cascade model with fixed order matrix elements*, JHEP **05** (2002) 046, [`hep-ph/0112284`].

[58] A. Schalicke and F. Krauss, *Implementing the ME+PS merging algorithm*, JHEP **07** (2005) 018, [`hep-ph/0503281`].

[59] F. Krauss, A. Schalicke, and G. Soff, *APACIC++ 2.0: a parton cascade in C++*, Comput. Phys. Commun. **174** (2006) 876–902, [`hep-ph/0503087`].

[60] N. Lavesson and L. Lonnblad, *W + jets matrix elements and the dipole cascade*, JHEP **07** (2005) 054, [`hep-ph/0503293`].

[61] S. Mrenna and P. Richardson, *Matching matrix elements and parton showers with HERWIG and PYTHIA*, JHEP **05** (2004) 040, [`hep-ph/0312274`].

[62] M. L. Mangano, M. Moretti, F. Piccinini, R. Pittau, and A. D. Polosa, *ALPGEN, a generator for hard multiparton processes in hadronic collisions*, JHEP **07** (2003) 001, [`hep-ph/0206293`].

[63] J. Alwall *et. al.*, *Comparative study of various algorithms for the merging of parton showers and matrix elements in hadronic collisions*, Eur. Phys. J. **C53** (2008) 473–500, [`arXiv:0706.2569`].

[64] S. Frixione and B. R. Webber, *Matching NLO QCD computations and parton shower simulations*, JHEP **06** (2002) 029, [`hep-ph/0204244`].

[65] S. Frixione and B. R. Webber, *The MC@NLO 3.3 event generator*, [hep-ph/0612272].

[66] S. Frixione, E. Laenen, P. Motylinski, and B. R. Webber, *Single-top production in MC@NLO*, *JHEP* **03** (2006) 092, [hep-ph/0512250].

[67] S. Frixione, E. Laenen, P. Motylinski, and B. R. Webber, *Angular correlations of lepton pairs from vector boson and top quark decays in Monte Carlo simulations*, *JHEP* **04** (2007) 081, [hep-ph/0702198].

[68] S. Frixione, E. Laenen, P. Motylinski, B. Webber, and C. D. White, *Single-top hadroproduction in association with a W boson*, [hep-ph/0805.3067].

[69] O. Latunde-Dada, *Herwig++ Monte Carlo at next-to-leading order for e^+e^- annihilation and lepton pair production*, [arXiv:0708.4390].

[70] O. Latunde-Dada, *MC@NLO for the hadronic decay of Higgs bosons in associated production with vector bosons*, *JHEP* **05** (2009) 112, [arXiv:0903.4135].

[71] A. Papaefstathiou and O. Latunde-Dada, *NLO production of W ' bosons at hadron colliders using the MC@NLO and POWHEG methods*, *JHEP* **07** (2009) 044, [arXiv:0901.3685].

[72] F. Englert and R. Brout, *Broken symmetry and the mass of gauge vector mesons*, *Phys. Rev. Lett.* **13** (1964) 321–322.

[73] P. W. Higgs, *Broke symmetries and the masses of gauge bosons*, *Phys. Rev. Lett.* **13** (1964) 508–509.

[74] G. S. Guralnik, C. R. Hagen, and T. W. B. Kibble, *Global conservation laws and massless particles*, *Phys. Rev. Lett.* **13** (1964) 585–587.

[75] T. W. B. Kibble, *Symmetry breaking in non-Abelian gauge theories*, *Phys. Rev.* **155** (1967) 1554–1561.

[76] D. Zeppenfeld, R. Kinnunen, A. Nikitenko, and E. Richter-Was, *Measuring Higgs boson couplings at the LHC*, *Phys. Rev.* **D62** (2000) 013009, [hep-ph/0002036].

[77] A. Belyaev and L. Reina, $pp \to t\bar{t}H$, $H \to \tau^+\tau^-$: *toward a model independent determination of the Higgs boson couplings at the LHC*, *JHEP* **08** (2002) 041, [hep-ph/0205270].

[78] H. M. Georgi, S. L. Glashow, M. E. Machacek, and D. V. Nanopoulos, *Higgs bosons from two gluon annihilation in proton proton collisions*, *Phys. Rev. Lett.* **40** (1978) 692.

[79] D. L. Rainwater, D. Zeppenfeld, and K. Hagiwara, *Searching for $H \to \tau^+\tau^-$ in weak boson fusion at the LHC*, *Phys. Rev.* **D59** (1999) 014037, [hep-ph/9808468].

[80] T. Plehn, D. L. Rainwater, and D. Zeppenfeld, *A method for identifying* $H \to \tau^+\tau^- \to e^\pm \mu^\mp +$ *missing* p_T *at the CERN LHC, Phys. Rev.* **D61** (2000) 093005, [`hep-ph/9911385`].

[81] D. L. Rainwater and D. Zeppenfeld, *Observing* $H \to W^{(*)}W^{(*)} \to e^\pm \mu^\mp \not{p}_T$ *in weak boson fusion with dual forward jet tagging at the CERN LHC, Phys. Rev.* **D60** (1999) 113004, [`hep-ph/9906218`].

[82] N. Kauer, T. Plehn, D. L. Rainwater, and D. Zeppenfeld, $H \to WW$ *as the discovery mode for a light Higgs boson, Phys. Lett.* **B503** (2001) 113–120, [`hep-ph/0012351`].

[83] D. L. Rainwater and D. Zeppenfeld, *Searching for* $H \to \gamma\gamma$ *in weak boson fusion at the LHC, JHEP* **12** (1997) 005, [`hep-ph/9712271`].

[84] O. J. P. Eboli and D. Zeppenfeld, *Observing an invisible Higgs boson, Phys. Lett.* **B495** (2000) 147–154, [`hep-ph/0009158`].

[85] D. Cavalli *et. al.*, *The Higgs working group: summary report,* [`hep-ph/0203056`].

[86] T. Plehn, D. L. Rainwater, and D. Zeppenfeld, *Determining the structure of Higgs couplings at the LHC, Phys. Rev. Lett.* **88** (2002) 051801, [`hep-ph/0105325`].

[87] T. Han and S. Willenbrock, *QCD correction to the* $p\,p \to W\,H$ *and* $Z\,H$ *total cross- sections, Phys. Lett.* **B273** (1991) 167–172.

[88] A. Djouadi, M. Spira, and P. M. Zerwas, *Production of Higgs bosons in proton colliders: QCD corrections, Phys. Lett.* **B264** (1991) 440–446.

[89] M. Spira, A. Djouadi, D. Graudenz, and P. M. Zerwas, *Higgs boson production at the LHC, Nucl. Phys.* **B453** (1995) 17–82, [`hep-ph/9504378`].

[90] S. Dawson, *Radiative corrections to Higgs boson production, Nucl. Phys.* **B359** (1991) 283–300.

[91] W. Giele *et. al.*, *The QCD/SM working group: summary report,* [`hep-ph/0204316`].

[92] S. Catani, D. de Florian, and M. Grazzini, *Higgs production in hadron collisions: soft and virtual QCD corrections at NNLO, JHEP* **05** (2001) 025, [`hep-ph/0102227`].

[93] R. V. Harlander and W. B. Kilgore, *Soft and virtual corrections to* $pp \to H + X$ *at NNLO, Phys. Rev.* **D64** (2001) 013015, [`hep-ph/0102241`].

[94] R. V. Harlander and W. B. Kilgore, *Next-to-next-to-leading order Higgs production at hadron colliders, Phys. Rev. Lett.* **88** (2002) 201801, [`hep-ph/0201206`].

[95] C. Anastasiou and K. Melnikov, *Higgs boson production at hadron colliders in NNLO QCD*, Nucl. Phys. **B646** (2002) 220–256, [`hep-ph/0207004`].

[96] V. Ravindran, J. Smith, and W. L. van Neerven, *NNLO corrections to the total cross section for Higgs boson production in hadron hadron collisions*, Nucl. Phys. **B665** (2003) 325–366, [`hep-ph/0302135`].

[97] L. D'Errico and P. Richardson, *A positive-weight next-to-leading-order Monte Carlo simulation of deep inelastic scattering and Higgs boson production via vector boson fusion in Herwig++*, [`arXiv:1106.2983`].

[98] T. Figy, C. Oleari, and D. Zeppenfeld, *Next-to-leading order jet distributions for Higgs boson production via weak-boson fusion*, Phys. Rev. **D68** (2003) 073005, [`hep-ph/0306109`].

[99] R. Kleiss, *From two to three jets in heavy boson decays: an algorithmic approach*, Phys. Lett. **B180** (1986) 400.

[100] P. De Causmaecker, R. Gastmans, W. Troost, and T. T. Wu, *Multiple Bremsstrahlung in gauge theories at high- energies. 1. General formalism for quantum electrodynamics*, Nucl. Phys. **B206** (1982) 53.

[101] L. Lönnblad, *ThePEG, PYTHIA7, Herwig++ and ARIADNE*, Nucl. Instrum. Meth. **A559** (2006) 246–248.

[102] M. Cacciari and G. P. Salam, *Dispelling the N^3 myth for the k_t jet-finder*, Phys. Lett. **B641** (2006) 57–61, [`hep-ph/0512210`].

[103] P. Nason and C. Oleari, *NLO Higgs boson production via vector-boson fusion matched with shower in POWHEG*, [`arXiv:0911.5299`].

[104] W.-K. Tung, *New generation of parton distributions with uncertainties from global QCD analysis*, Acta Phys. Polon. **B33** (2002) 2933–2938, [`hep-ph/0206114`].

[105] S. Alioli, P. Nason, C. Oleari, and E. Re, *A general framework for implementing NLO calculations in shower Monte Carlo programs: the POWHEG BOX*, JHEP **1006** (2010) 043, [`arXiv:1002.2581`].

[106] K. Hamilton, P. Richardson, and J. Tully, *A positive-weight next-to-leading order Monte Carlo simulation for Higgs boson production*, JHEP **04** (2009) 116, [`arXiv:0903.4345`].

[107] J. R. Ellis, M. K. Gaillard, and D. V. Nanopoulos, *A phenomenological profile of the Higgs boson*, Nucl. Phys. **B106** (1976) 292.

[108] M. A. Shifman, A. I. Vainshtein, M. B. Voloshin, and V. I. Zakharov, *Low-energy theorems for Higgs boson couplings to photons*, Sov. J. Nucl. Phys. **30** (1979) 711–716.

[109] J. F. Gunion and H. E. Haber, *Higgs boson production in the photon-photon collider mode of a high-energy e+ e- linear collider*, Phys. Rev. **D48** (1993) 5109–5120.

[110] G. L. Kane, G. D. Kribs, S. P. Martin, and J. D. Wells, *Two photon decays of the lightest Higgs boson of supersymmetry at the LHC*, Phys. Rev. **D53** (1996) 213–220, [`hep-ph/9508265`].

[111] B. Kileng, P. Osland, and P. N. Pandita, *Production and two photon decay of the MSSM scalar Higgs boson at the LHC*, Z. Phys. **C71** (1996) 87–94, [`hep-ph/9506455`].

[112] **The ATLAS** Collaboration, G. Aad *et. al.*, *Expected performance of the ATLAS experiment - detector, trigger and physics*, [`arXiv:0901.0512`].

[113] **CMS** Collaboration, G. L. Bayatian *et. al.*, *CMS technical design report, volume II: physics performance*, J. Phys. **G34** (2007) 995–1579.

[114] **D0** Collaboration, V. M. Abazov *et. al.*, *Search for resonant diphoton production with the D0 detector*, Phys. Rev. Lett. **102** (2009) 231801, [`arXiv:0901.1887`].

[115] S. Mrenna and J. D. Wells, *Detecting a light Higgs boson at the Fermilab Tevatron through enhanced decays to photon pairs*, Phys. Rev. **D63** (2001) 015006, [`hep-ph/0001226`].

[116] M. C. Kumar, P. Mathews, V. Ravindran, and A. Tripathi, *Diphoton signals in theories with large extra dimensions to NLO QCD at hadron colliders*, Phys. Lett. **B672** (2009) 45–50, [`arXiv:0811.1670`].

[117] G. F. Giudice and R. Rattazzi, *Theories with gauge-mediated supersymmetry breaking*, Phys. Rept. **322** (1999) 419–499, [`hep-ph/9801271`].

[118] **WA70** Collaboration, E. Bonvin *et. al.*, *Intrinsic transverse momentum in the pi- p → gamma gamma X reaction at 280-GeV/c*, Phys. Lett. **B236** (1990) 523.

[119] **WA70 Collaboration** Collaboration, E. Bonvin *et. al.*, *Double prompt photon production at high transverse momentum by pi- on protons at 280-GeV/c*, Z.Phys. **C41** (1989) 591.

[120] **E706 Collaboration** Collaboration, M. Begel, *Photons and diphotons from E706*, Nucl.Phys.Proc.Suppl. **79** (1999) 244–246.

[121] **UA1** Collaboration, C. Albajar *et. al.*, *Direct photon production at the CERN proton - anti-proton collider*, Phys. Lett. **B209** (1988) 385–396.

[122] **UA2** Collaboration, J. Alitti *et. al.*, *A Measurement of single and double prompt photon production at the CERN $\bar{p}p$ collider*, Phys. Lett. **B288** (1992) 386–394.

[123] **CDF** Collaboration, F. Abe *et. al.*, *Measurement of the cross-section for production of two isolated prompt photons in $\bar{p}p$ collisions at $\sqrt{s} = 1.8$ TeV*, *Phys. Rev. Lett.* **70** (1993) 2232–2236.

[124] **CDF** Collaboration, D. E. Acosta *et. al.*, *Measurement of the cross section for prompt diphoton production in $p\bar{p}$ collisions at $\sqrt{s} = 1.96$ TeV*, *Phys. Rev. Lett.* **95** (2005) 022003, [`hep-ex/0412050`].

[125] **The D0** Collaboration, V. M. Abazov *et. al.*, *Measurement of direct photon pair production cross sections in ppbar collisions at sqrt(s)=1.96 TeV*, *Phys. Lett.* **B690** (2010) 108–117, [`arXiv:1002.4917`].

[126] E. L. Berger, E. Braaten, and R. D. Field, *Large p(T) production of single and double photons in proton proton and pion-proton collisions*, *Nucl. Phys.* **B239** (1984) 52.

[127] C. H. Llewellyn Smith, *QCD predictions for processes involving real photons*, *Phys. Lett.* **B79** (1978) 83.

[128] H. Baer, J. Ohnemus, and J. F. Owens, *A next-to-leading logarithm calculation of direct photon production*, *Phys. Rev.* **D42** (1990) 61–71.

[129] P. Aurenche, R. Baier, M. Fontannaz, and D. Schiff, *Prompt photon production at large p(T) scheme invariant QCD predictions and comparison with experiment*, *Nucl. Phys.* **B297** (1988) 661.

[130] L. E. Gordon and W. Vogelsang, *Polarized and unpolarized isolated prompt photon production beyond the leading order*, *Phys. Rev.* **D50** (1994) 1901–1916.

[131] P. Aurenche, A. Douiri, R. Baier, M. Fontannaz, and D. Schiff, *Large p(T) double photon production in hadronic collisions: beyond leading logarithm QCD calculation*, *Z. Phys.* **C29** (1985) 459–475.

[132] B. Bailey, J. F. Owens, and J. Ohnemus, *An order alpha-s Monte Carlo calculation of hadronic double photon production*, *Phys. Rev.* **D46** (1992) 2018–2027.

[133] V. Del Duca, F. Maltoni, Z. Nagy, and Z. Trocsanyi, *QCD radiative corrections to prompt diphoton production in association with a jet at hadron colliders*, *JHEP* **04** (2003) 059, [`hep-ph/0303012`].

[134] P. Aurenche, R. Baier, and M. Fontannaz, *Prompt photon production at colliders*, *Phys. Rev.* **D42** (1990) 1440–1449.

[135] E. W. N. Glover and A. G. Morgan, *Measuring the photon fragmentation function at LEP*, *Z. Phys.* **C62** (1994) 311–322.

[136] S. Frixione, *Isolated photons in perturbative QCD*, *Phys. Lett.* **B429** (1998) 369–374, [`hep-ph/9801442`].

[137] S. Catani, M. Fontannaz, J. P. Guillet, and E. Pilon, *Cross-section of isolated prompt photons in hadron hadron collisions*, *JHEP* **05** (2002) 028, [hep-ph/0204023].

[138] T. Binoth, J. P. Guillet, E. Pilon, and M. Werlen, *A full next-to-leading order study of direct photon pair production in hadronic collisions*, *Eur. Phys. J.* **C16** (2000) 311–330, [hep-ph/9911340].

[139] L. D'Errico and P. Richardson, *Next-to-leading-order Monte Carlo simulation of diphoton production in hadronic collisions*, [arXiv:1106.3939].

[140] C. Balazs, E. L. Berger, S. Mrenna, and C. P. Yuan, *Photon pair production with soft gluon resummation in hadronic interactions*, *Phys. Rev.* **D57** (1998) 6934–6947, [hep-ph/9712471].

[141] C. Balazs, E. L. Berger, P. M. Nadolsky, and C. P. Yuan, *Calculation of prompt diphoton production cross sections at Tevatron and LHC energies*, *Phys. Rev.* **D76** (2007) 013009, [arXiv:0704.0001].

[142] P. M. Nadolsky, C. Balazs, E. L. Berger, and C. P. Yuan, *Gluon-gluon contributions to the production of continuum diphoton pairs at hadron colliders*, *Phys. Rev.* **D76** (2007) 013008, [hep-ph/0702003].

[143] P. M. Nadolsky and C. R. Schmidt, *Diphoton production in gluon fusion at small transverse momentum*, *Phys. Lett.* **B558** (2003) 63–68, [hep-ph/0211398].

[144] C. Balazs, P. M. Nadolsky, C. Schmidt, and C. Yuan, *Diphoton background to Higgs boson production at the LHC with soft gluon effects*, *Phys.Lett.* **B489** (2000) 157–162, [hep-ph/9905551].

[145] A. Buckley *et. al.*, *Rivet user manual*, [hep-ph/1003.0694].

[146] C. Balazs, E. L. Berger, P. M. Nadolsky, and C. P. Yuan, *All-orders resummation for diphoton production at hadron colliders*, *Phys. Lett.* **B637** (2006) 235–240, [hep-ph/0603037].

[147] D. H. Coward *et. al.*, *Electron-proton elastic scattering at high momentum transfers*, *Phys. Rev. Lett.* **20** (1968) 292–295.

[148] E. D. Bloom *et. al.*, *High-energy inelastic e p scattering at 6-degrees and 10-degrees*, *Phys. Rev. Lett.* **23** (1969) 930–934.

[149] E. D. Bloom *et. al.*, *Recent results in inelastic electron scattering*, . Presented at the XV International Conference on High Energy Physics, Kiev, USSR, Aug 26-Sep4, 1970.

[150] M. Breidenbach *et. al.*, *Observed behavior of highly inelastic electron-proton scattering*, *Phys. Rev. Lett.* **23** (1969) 935–939.

[151] J. D. Bjorken, *Theoretical ideas on high-energy inelastic electron proton scattering*, . Invited paper at the Amer. Phys. Soc. New York Meeting, Feb 3, 1969.

[152] R. P. Feynman, *Very high-energy collisions of hadrons*, Phys. Rev. Lett. **23** (1969) 1415–1417.

[153] J. I. Friedman, *Deep inelastic scattering: comparisons with the quark model*, Rev. Mod. Phys. **63** (Jul, 1991) 615–627.

[154] **ZEUS** Collaboration, S. Chekanov *et. al.*, *High-Q^2 neutral current cross sections in e^+p deep inelastic scattering at $\sqrt{s} = 318\,GeV$*, Phys. Rev. **D70** (2004) 052001, [`hep-ex/0401003`].

[155] **ZEUS** Collaboration, S. Chekanov *et. al.*, *Measurement of high-Q^2 e^-p neutral current cross sections at HERA and the extraction of xF_3*, Eur. Phys. J. **C28** (2003) 175, [`hep-ex/0208040`].

[156] S. Catani and M. H. Seymour, *NLO QCD calculations in DIS at HERA based on the dipole formalism*, [`hep-ph/9609521`].

[157] **ZEUS** Collaboration, S. Chekanov *et. al.*, *A ZEUS next-to-leading-order QCD analysis of data on deep inelastic scattering*, Phys. Rev. **D67** (2003) 012007, [`hep-ex/0208023`].

[158] **H1** Collaboration, C. Adloff *et. al.*, *Measurements of transverse energy flow in deep inelastic-scattering at HERA*, Eur. Phys. J. **C12** (2000) 595–607, [`hep-ex/9907027`].

[159] T. Carli, T. Gehrmann, and S. Hoeche, *Hadronic final states in deep-inelastic scattering with Sherpa*, Eur. Phys. J. **C67** (2010) 73–97, [`arXiv:0912.3715`].

[160] **H1** Collaboration, C. Adloff *et. al.*, *Measurement of inclusive jet cross-sections in deep- inelastic e p scattering at HERA*, Phys. Lett. **B542** (2002) 193–206, [`hep-ex/0206029`].

[161] G. F. Sterman and S. Weinberg, *Jets from quantum chromodynamics*, Phys. Rev. Lett. **39** (1977) 1436.

[162] **ZEUS** Collaboration, A. A. Savin, "Event shapes in deep inelastic scattering at HERA." Prepared for 14th International Workshop on Deep Inelastic Scattering (DIS 2006), Tsukuba, Japan, 20-24 Apr 2006.

[163] A. A. Everett, "Measurements of event shapes in deep inelastic scattering at HERA with ZEUS." UMI-32-22794.

[164] A. Robichaud-Veronneau, "Event shapes in DIS at HERA." Summer Report.